Volume 20 No. 2 • Fall 2013

MagLab Reports

The 2012 Highlights Issue

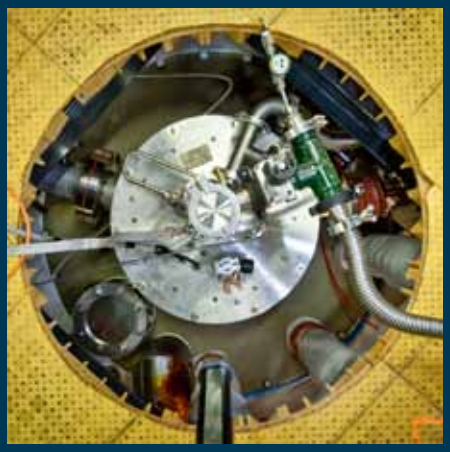
The lab's most important user research from last year **PAGE 6**

Theory Winter School

Info on our upcoming conference on topological phases **PAGE 10**











NATIONAL HIGH MAGNETIC FIELD LABORATORY
FSU • UF • LANL

TABLE OF CONTENTS

FEATURES

4 **DIRECTOR'S DESK**
The Year in Review
by Gregory Boebinger

10 **THEORY WINTER SCHOOL**
Details about our conference on Topological Phases

32 **USER CENTER**
2012 World-wide User Map

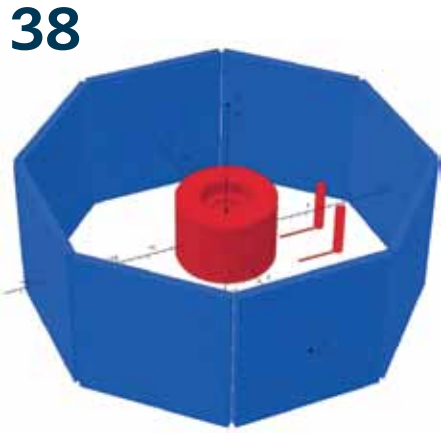
60 **USER SUMMER SCHOOL**
A crash course in measurement

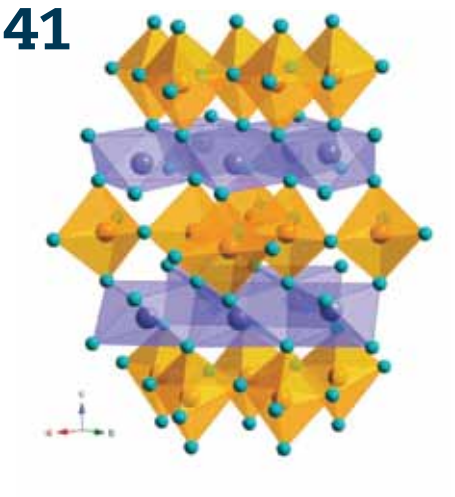
62 **MAGLAB NEWS**
Honors, awards, news briefs

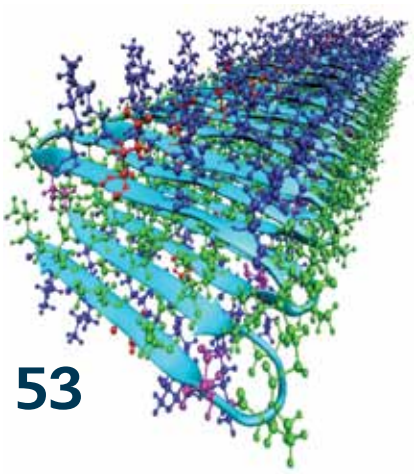
RESEARCH STORIES

6 **CONDENSED MATTER SCIENCE**
Condensed matter technique development, graphene, Kondo/heavy fermion systems, magnetism & magnetic materials, molecular conductors, quantum fluids & solids, qubits & quantum entanglement, semiconductors, basic superconductivity, topological matter and other condensed matter

06 Development of a Force Magnetometer for the NHMFL DC Field Facility
07 Quantum Hall Effect in Hydrogenated Graphene
08 Spin Phase Transition in Bilayer Graphene at Charge Neutrality
09 Filling-factor-dependent Magnetophonon Resonance in Graphene Revealed by Magneto-Raman Spectroscopy
11 Infrared Spectroscopy of Tunable Magneto-Plasmons in Graphene
12 Electronic Multicriticality in Bilayer Graphene
14 Quantum Oscillation Measurements in Cerium 235s
16 Magnetostriction and Magnetic Texture to 100.75 Tesla in Frustrated $SrCu_2(BO_3)_2$
17 Successive Magnetic Phase Transitions and Multiferroicity in Spin-1 Triangular Lattice Antiferromagnet $Ba_3NiNb_2O_9$
18 Giant Magnetic Hysteresis in Sr_3NiIrO_6
19 Spin-nematic Phase in the S = 1/2 Antiferromagnet $LiCuVO_4$ Probed by NMR at 45 T
21 Evolution of Magnetism in a Jahn-Teller Driven Magnetic Dimensionality Switch
22 Observation of a Bose Glass State in Doped Quantum Magnet
23 Reentrant Integer Quantum Hall Effect in the Lowest Landau Level
24 Magneto-Photoluminescence Measurements of Dilute $GaAs_{1-x}N_x$
25 Resonant Ultrasound Spectroscopy (RUS) Measurements on Ultra-high Quality YBCO Single Crystal Cuprates
27 Unprecedented Fermi Surface Spectral Resolution in the Underdoped High T_c Superconductor $YBa_2Cu_3O_{6+x}$ Obtained Using 100 Tesla Magnetic Fields
28 Transition from Slow Abrikosov to Fast Moving Josephson Vortices in Iron-Pnictide Superconductors
29 Quantum Oscillations from a 2D Electron Gas at a Mott/band Insulator Interface
30 Tuning the Quantum Oscillations of Dirac Surface Electrons in a Topological Insulator by Ionic Liquid Gating
34 Dirac electrons in topological insulator candidates







35 MAGNETS & MAGNET MATERIALS
Engineering materials, magnet technology and applied superconductivity

35 High Field Magnets with $Bi_2Sr_2CaCu_2O_{8+x}$ /Ag alloy Round Wire

36 Thermal Conductivity Test of YBCO Coated-Conductor Tape Stacks Interleaved with Insulated Stainless Steel Tapes

38 Comprehensive Analysis of Binary Current Leads for the NHMFL Series Connected Hybrid Magnet in the Course of Their Development

39 Overpressure Processing as the Route to Dense, High Critical Current Density, Coil-Length Bi-2212 Round Wires

40 Magneto-Optical and Electromagnetic Study of Intergrain Critical Current in Fine-Grain $(Ba_{0.6}K_{0.4})Fe_2As_2$ Wire and Bulks

41 CHEMISTRY
Chemistry, geochemistry and magnetic resonance technique development

41 HFEPR of Magnetic Materials with Unusual Optical Properties: $YIn_{1-x}Fe_xO_3$

42 EPR Studies of a Mn(III)–Cu(II) Dimer Containing a Jahn–Teller Compressed Mn Ion

43 Giant Ising-type Magnetic Anisotropy in Trigonal Bipyramidal Ni(II) Complexes

44 Atmospheric Pressure Laser-Induced Acoustic Desorption Chemical Ionization Mass Spectrometry for Analysis of Saturated Hydrocarbons

45 Closed Network Growth of Fullerenes

46 Encapsulated Gadolinium and Dysprosium Ions Within Ultra-Short Carbon Nanotubes for MR Microscopy at 11.75 and 21.1 T

48 High-Resolution Imaging Probe for STRAFI Studies of Solid-Materials

50 LIFE SCIENCES
Biochemistry and biology

50 Solid-State NMR Structural and Dynamics Studies of HIV-1 Protein Assemblies

52 Solid-State NMR Evidence for Eumelanin from the Jurassic Period

53 Solid State NMR Structural Characterization of MAX8 Peptide Nanofibers

55 Emerging Tumor Resistance and Sodium-Diffusion MRI

57 Ultrafast *in vivo* Diffusion Imaging of Stroke at 21.1 T by Spatiotemporal Encoding

59 Identification of Male and Female Mating Pheromones in *Panagrellus redivivus*

The MagLab in 2012: Keeping A Finger on the Pulse of Cutting-edge Science

2012 was an exciting year at the MagLab. We achieved a series of successful experiments in the 100.75 tesla (T) nondestructive magnet at our Los Alamos Pulsed Field Facility in March and, four months later, the National Science Foundation awarded the MagLab its five-year renewal grant, which will allow us to keep the lights (and, more importantly, the magnets!) running through 2017.

And true to its core mission, the MagLab continues to host some of the world's best scientists doing superb science. This year was record-breaking with 1,352 researchers from around the world - the largest number to date - using the lab's seven facilities. Of the 365 principal investigators, 72 were first-time investigators, and more than 23 percent of the year's total users were women or minorities.

Highlight-worthy

Of the 415 research reports submitted in 2012:

- 101 reports (24 percent) were published in 2012, or have been accepted for publication, many in prominent journals like *Nature*, *Physical Review Letters* and *Proceedings of the National Academy of Science*.
- An additional 41 reports (10 percent) were submitted for publication.
- Nearly 38 percent have manuscripts in preparation for publication.

Selecting highlights is a bit like picking your favorite child. To build this year's highlights issue, the MagLab's Science Council culled through all 415 research reports across 18 categories, including magnet science and technology, materials science, condensed matter physics, chemistry and the life sciences. As the director, it is my pleasure (and difficult task) to finalize the list and decide which reports to feature in this highlights issue.

The following 39 highlights emphasize what is truly great about the Magnet Lab – they equally showcase the diverse impact of high magnetic field science, the outstanding quality of research that happens here, and our continuous pursuit to push science further with the creation of new tools, techniques and methods. The highlights come from across the lab's three sites and seven user facilities and give a marvelous sampling of what multidisciplinary science can achieve.

Applied Superconductivity: Hot New Technologies

Exciting scientific and technological discoveries were made at the lab this year related to the high temperature superconductor Bi-2212.

- Scientists at the lab provided a proof of principle that round-wire Bi-2212 is suitable for high-field magnet applications (*Overpressure Processing as the Route to Dense, High Critical Current Density, Coil-Length Bi-2212 Round Wires*, page 39).
- Improvements in processing and insulation now demonstrate that compact Bi-2212 coils are possible and make good alternatives to coated conductor technology for specific applications (*High-Field Magnets with $Bi_2Sr_2CaCu_2O_{8+x}$/Ag Alloy Round Wire*, page 35).

100 T Pulsed Magnet Breaks Megagauss Barrier and Delivers Mega-Science

More interesting research on superconductivity was enabled by our groundbreaking 100 tesla pulsed magnet in Los Alamos.

- With the unique capabilities of this high-field magnet, scientists were able to see more of the quantum oscillations for

Science Council

Composed of distinguished research scientists representing all three sites of the Magnet Lab, the Science Council is responsible for, among other things, recommending each year's research highlights. Members are:

Albert Migliori, LANL Fellow and Pulsed Magnet User Program
Art Edison, Professor of Biochemistry and AMRIS User Program
James Brooks, Professor, Physics Chair
Gail Fanucci, Assistant Professor, AMRIS User Program
Lucio Frydman, Chief Scientist for Chemistry and Biology
Zhehong Gan, Scholar-Scientist, NMR User Program
Lev Gor'kov, Program Director, Professor, Condensed Matter Science/Theory
Stephen Hill, Director, EMR Program User Program
Jurek Krzystek, Scholar-Scientist, EMR User Program
David Larbalestier, Director, Applied Superconductivity Center
Dragana Popovic, Scholar-Scientist, Condensed Matter Science/Experimental
Ryan Rodgers, Associate Scholar-Scientist, ICR User Program
Theo Siegrist, Professor, Condensed Matter Science/Experimental
Glenn Walter, Associate Professor, AMRIS User Program
Huub Weijers, Engineer, Magnet Science & Technology

YBCO and deduce additional information about the Fermi surface of this high-temperature superconductor (*Unprecedented Fermi Surface Spectral Resolution in the Underdoped High Tc Superconductor $YBa_2Cu_3O_{6+x}$ Obtained Using 100 Tesla Magnetic Field*, page 27).

- The 100 tesla pulsed magnet also facilitated the discovery of magnetization plateaus in $SrCu_2(BO_3)_2$ centered at 75 T and 95 T. These and other magnetization plateaus result from novel magnetic dipole configurations. They had been predicted, but the capabilities of the 100 tesla pulsed magnet are required to make them observable (*Magnetostriction and Magnetic Texture to 100.75 Tesla in Frustrated $SrCu_2(BO_3)_2$*, page 16) .

Cool Science with Carbon

Carbon continues to be an interesting material for research in high magnetic fields, whether in the form of fullerenes or graphene.

- For the first time, scientists discovered that fullerenes self-assemble and "grow" by absorbing vaporized carbon atoms into their structure (*Closed Network Growth of Fullerenes*, page 45).
- Other researchers performed far-infrared transmission measurements on graphene in 17.5 T fields, finding potential applications in magneto-optical devices, such as optical modulators or Faraday rotators (*Infrared Spectroscopy of Tunable Magneto-Plasmons in Graphene*, page 11).

Relevant, Resonance Science

In the areas of MRI, NMR, ICR and EMR, the MagLab remains at the forefront of groundbreaking research.

- Using our 900 MHz ultra wide-bore magnet, researchers were able to image sodium in vivo to gain information about the level of drug resistance of tumors to chemotherapy. This basic research carries strong implications for future cancer treatment, perhaps enabling patients and doctors to know whether chemotherapy has worked within days as opposed to weeks or months (*Emerging Tumor Resistance and Sodium-Diffusion MRI*, page 55).
- NMR spectroscopy showed researchers that a form of melanin existed in fossils from the Jurassic period, demonstrating that this material stays in a fossil for at least 160 million years, the oldest determination to date (*Solid-State NMR Evidence for Eumelanin from the Jurassic Period*, page 52).

Diverse Investment in Science

All of this exciting science would not have been possible without funding and support. The majority of 2012's research projects were funded by the U.S. National Science Foundation, the U.S. Department of Energy, and the U.S. National Institutes of Health. Other funding organizations included: National Aeronautics and Space Administration (NASA), U.S. Department of Defense, U.S. Air Force Office of Scientific Research, U.S. Army, U.S. Navy and numerous universities.

Research in 2012 also received international support from science foundations, ministries and universities around the world, including Brazil, Canada, China, Denmark, France, Germany, Israel, Japan, Poland, Russia, Slovakia, South Korea and the United Kingdom.

The Magnet Lab itself invested in bold, risky scientific efforts through our Annual User Collaboration Grants Program. This program encourages collaborations among internal and external investigators by providing seed money for new science and enhancements of experimental techniques. In 2012, the program supported 48 of the 415 research activities, a 64 percent increase over the previous year.

A large thank you is due, as always, to our user community for developing this excellent body of work. I look forward to sharing more great science in the months and years to come.

And now, the 2012 highlights!

Rock and roll,



Gregory S. Boebinger
MagLab Director

Mag Lab Reports

Volume 20 No. 2 • Fall 2013

PUBLISHED BY
The National High Magnetic Field Laboratory
1800 East Paul Dirac Drive
Tallahassee, FL 32310-3706

PHONE NUMBER
(850) 644-0311

MAGNET LAB DIRECTOR
Greg Boebinger

USER PROGRAMS CHIEF OF STAFF
Anke Toth

EDITOR
Kristin Roberts

GRAPHIC DESIGNER
Liz Vernon

This document is available in alternate formats upon request. Contact Public Affairs for assistance. If you'd like to be added to our mailing list, please write us at the address shown above, call (850) 644-1933,or e-mail *public-affairs@magnet.fsu.edu*.

The MagLab is supported by the National Science Foundation and the state of Florida.

www.magnet.fsu.edu

Facebook.com/NationalMagLab
@NationalMagLab
Youtube.com/nhmfl

Condensed Matter Technique Development

The first step in the characterization of strongly correlated systems, perhaps the most often studied materials at NHMFL, invariably requires measurements of magnetization in high magnetic fields at low temperatures. However, many techniques for these measurements suffer from a number of technical handicaps. With its unique design involving two pairs of crossed suspension wires and a capacitive transducer, the force magnetometer is especially suitable for high-field low-temperature measurements, and will soon be available in the NHMFL user program, thanks to the work by Aoyama *et al.*

Development of a Force Magnetometer for the NHMFL DC Field Facility

C.P. Aoyama and Y. Takano (UF, Physics)**; T. Sakakibara** (Univ. Tokyo, ISSP)

Introduction

Magnetization is one of the key bulk static properties in magnetism and superconductivity. Accurate characterization of strongly correlated systems invariably requires measurements of magnetization in high magnetic fields at low temperatures. However, many techniques for these measurements suffer from heating (SQUID magnetometers, vibrating sample magnetometers), incompatibility with very high fields (SQUID magnetometers, vibrating sample magnetometers), the magnetocaloric effect (the induction method in pulsed magnetic fields), or magnetic torque (cantilever magnetometers)—except force magnetometers. With its unique design involving two pairs of crossed suspension wires and a capacitive transducer, the force magnetometer developed by Sakakibara *et al.*[1] is especially suitable for high-field low-temperature measurements, with high immunity to magnetic torque arising from sample anisotropy or shape-dependent non-uniform demagnetizing field. However, this type of magnetometer has been in use only in a small number of laboratories, none of which are high magnetic field facilities and none of which are in this country, at least to our knowledge. To rectify this situation, we have developed a force magnetometer to be used at the NHMFL DC Field Facility. Although this magnetometer has been designed for the resistive magnet with a gradient coil at the facility, the initial test was performed using SCM1, an 18 T/20 T superconducting magnet which lacks a gradient coil.

Experimental, Results & Discussion

Figure 1 shows the magnetometer. A 30.62 mg nickel disk, 0.1 mm thick, was used as a sample to test and calibrate the magnetometer. The estimated saturation magnetization of the sample was 1.793 emu.[2] To obtain a field gradient required for magnetic force, the sample was placed in various positions away from the field center. As a result, the field gradient was proportional to the field for a given sample position. Results shown in **Figure 2** suggest that the magnetometer will perform well in the resistive magnet.



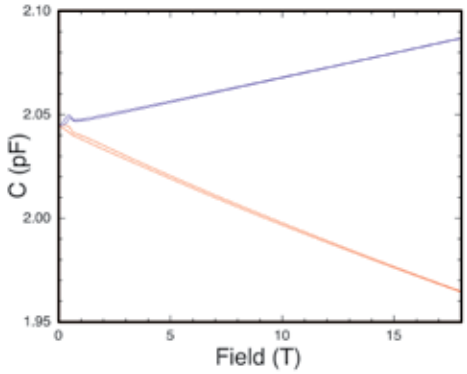


FIGURE 1. (LEFT) Force magnetometer. The overall diameter is 20 mm. The sample platform is at the bottom, facing down and hidden from the viewer. The two SIP connectors and the coiled leads, to which they are attached, are for a resistance thermometer and heater. Microcoaxes for the capacitor electrodes are not shown.

FIGURE 2. (RIGHT) Magntometer capacitance as a function of field at 20 mK for a nickel standard placed 22.4 mm above (red) and 11.4 mm below (blue) the field center. At 18 T, field gradients at these positions are –25.4 T/m and 11.2 T/m, estimated from the magnet manufacturer's calculated field profile.

Acknowledgments

We thank T.P. Murphy and J.-H. Park for useful discussions and technical assistance. This work was supported by NHMFL UCGP, University of Florida FEO program, and a JSPS fellowship.

REFERENCES

1. Sakakibara, T., Mitamura, H., Tayama, T., and Amitsuka, H., *Jpn. J. Appl. Phys.* **33**, 5067 (1994).

2. Danan, H., Herr, A., and Meyer, A. J. P., *J. Appl. Phys.* **39**, 669 (1968).

Graphene

This report describes how high magnetic fields have revealed the emergence of a quantum Hall state in hydrogenated graphene, a system where the amount of disorder is significantly higher than in previous studies of the quantum Hall effect (QHE). This work also opens up questions, such as the nature of the zero-field insulating state in hydrogenated graphene and the robustness of the QHE to disorder.

• Published in *Phys. Rev. Lett.*, **110**, 176801 (2013).

Quantum Hall Effect in Hydrogenated Graphene

J. Guillemette and G. Gervais (McGill U., Physics); **M. Siaj** (UQAM Chemistry); **R. Martel** (U. de Montréal, Chemistry); **T. Szkopek** (McGill U., Electrical and Computer Engineering)

Introduction

Two-dimensional atomic crystals have attracted much attention as surfaces with unique low-dimensional electron transport behaviour, most notably the zero-gap semiconductor graphene. The relativistic Dirac dispersion of electrons in graphene leads to an anomalous four-fold degenerate quantum Hall (QH) sequence. Common to these studies is low disorder, with a mean free path large compared to electron Fermi wavelength with the cleanest graphene samples exhibiting the fractional quantum Hall (FQH) effect. We report here our discovery of a quantum Hall effect in graphene at the opposite extreme, whereby hydrogenation was used to induce a short mean-free path beyond the Ioffe-Regel limit for the onset of strongly insulating behaviour. Our work illustrates the importance of the interplay between electron localization by point defect scattering and magnetic confinement in two-dimensional atomic crystals.

Experimental

Our starting material is large-area monolayer graphene grown by chemical vapour deposition (CVD) on Cu.[1] The graphene material quality was verified by Raman spectroscopy. We used a custom-built, high-flux, atomic hydrogen gun to thermally crack a flow of ultra-purified molecular hydrogen directed at a graphene device target while *in situ* electron transport measurement was performed during hydrogenation. The temperature dependence and perpendicular magnetic field dependence of the resistance of hydrogenated graphene was measured in SCM2 so as to identify the optimal sample for the 45 T hybrid magnet.

Results & Discussion

Figure 1A shows the dependence of the resistance on the perpendicular magnetic field and the carrier density (gate voltage). **Figure 1B** shows the quantum Hall effect in hydrogenated graphene where the two-point resistance saturates within 0.5% of $h/2e^2$ at 45 T, corresponding to ν=-2 Landau filling for hole conduction. Finally, **Figure 1C** shows the resistance plotted against the magnetic length. The disorder length obtained from Raman spectroscopy is identified as the shaded region.

Conclusions

The emergence of a quantum Hall state from a zero field effect mobility insulating state raises the question of how much disorder can be introduced into a 2D electron gas (2DEG) and still form a quantum Hall state. Our observations with hydrogenated graphene pushes the limit of disorder where the QHE can still be attained in a strong magnetic field, suggesting that the QHE might be robust to arbitrarily large disorder.

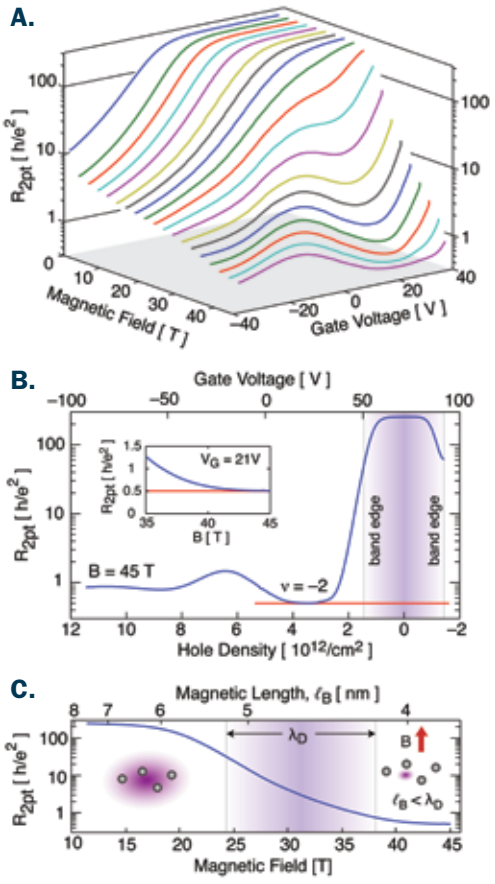


FIGURE 1. A. Plot of the resistance versus carrier density and magnetic field. **B.** A carrier density sweep at 45 T shows the resistance reaching a quantum hall plateau. **C.** Resistance versus magnetic length.

Acknowledgements

We thank NSERC (Canada), FQRNT (Quebec), and CIFAR for financial support.

REFERENCES

1. A. Guermoune, *et al. Carbon* **49**, 4204 (2011).

Graphene

A quantum-spin-Hall analogue has been predicted in bilayer graphene with a Landau level filling factor ν=0 if the ground state is a spin ferromagnet. This report describes a study of bilayer graphene in which the ν=0 state is tuned using an in-plane magnetic field and perpendicular electric field to reveal a transition to a ferromagnet, consistent with predictions.
• Published in *Nature Physics*, **9**, 154 (2013).

Spin Phase Transition in Bilayer Graphene at Charge Neutrality

P. Maher, A.F. Young and P. Kim (Columbia University, Physics); **C.R. Dean** (Columbia University, Electrical Engineering and Mechanical Engineering); **J. Hone** (Columbia University, Mechanical Engineering); **K.L. Shepard** (Columbia University, Electrical Engineering) **K. Watanabe and T. Taniguchi** (National Institute for Materials Science, Japan)

Introduction

The most celebrated property of the quantum spin Hall effect is the presence of spin-polarized counter-propagating edge states. This novel edge state configuration has also been predicted to occur in graphene when spin-split electron and hole-like Landau levels are forced to cross at the edge of the sample. In particular, a quantum spin hall analogue has been predicted at charge neutrality in bilayer graphene if the ground state is a spin ferromagnet. Because in-plane magnetic field couples directly to the spin degree of freedom and the interlayer asymmetry created by oppositely biased top and back gates couples to the valley degree of freedom, the ground state of bilayer graphene can be experimentally tuned.

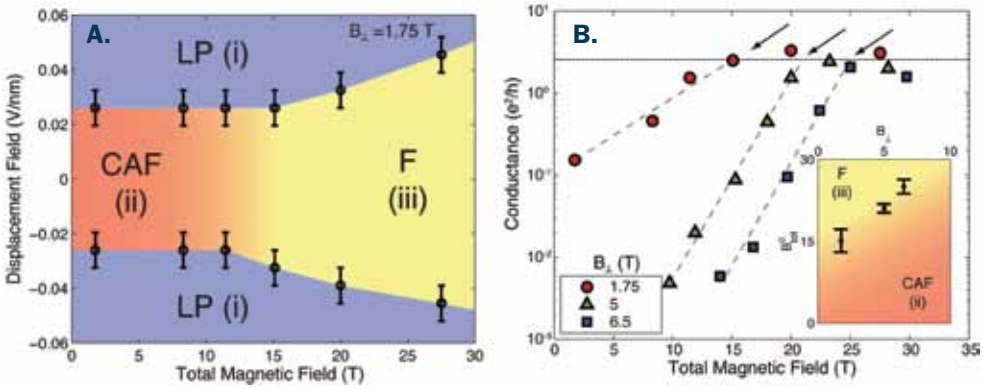


FIGURE 1. A & B

Experimental

Hexagonal-boron-nitride-encapsulated bilayer graphene devices were fabricated using a mechanical transfer process. Samples were patterned into a Hall bar using conventional electron beam lithography techniques, and contacted with electrical leads consisting of a Cr/Pd/Au metal stack. Four-terminal transport measurements were performed using standard low-frequency lock-in techniques. Displacement field was controlled by simultaneously changing top and back gates, and in-plane magnetic field was controlled by rotating the sample. All measurements were performed in a 31 tesla resistive magnet with the sample mounted in a ^{3}He cryostat (sample in vapor) at an approximate 300 mK base temperature.

Results & Discussion

By altering both the electric displacement field across the sample and the in-plane magnetic field at a fixed perpendicular magnetic field, we can tune the spin and pseudospin anisotropies and control the ordering of the $\nu = 0$ state. **Figure 1A** shows the phase diagram we observe. At high displacement field, the ground state is an insulating layer polarized phase. At low displacement field and low in-plane field, the ground state is an insulating canted antiferromagnet. As in-plane field is increased, the ground state transitions to a ferromagnet. **Figure 1B** shows that as this transition happens, the conductance increases exponentially with total field. At some finite total field, the conductance reaches a final value of ~$4e^2/h$. This is in agreement with predictions that the ferromagnet ground state should have gapless counter-propagating spin polarized edge states. This edge configuration is analogous to the quantum spin Hall effect.

REFERENCES

1. Maher, P. *et al., Nature Physics* **9**, 154 (2013).

Graphene

Graphene offers a rich playground to study electron-phonon interactions in 2D systems due to its unusual electronic structure and peculiar optical phonon dispersion. This study reveals a unique filling-factor and circular-polarization-dependent structure of magneto-phonon coupled modes, thus providing a comprehensive picture of magneto-phonon resonances in graphene.

• Published in *Phys. Rev. Lett.*, **110**, 227402 (2013).

Filling-Factor-Dependent Magnetophonon Resonance in Graphene Revealed by Magneto-Raman Spectroscopy

Y. Kim, J.M. Poumirol and D. Smirnov (NHMFL); **N.G. Kalugin** (New Mexico Tech); **J. Kono** (Rice University); **T. Georgiou, Y.J. Kim and K.S. Novoselov** (University of Manchester); **A. Lombardo and A.C. Ferrari** (Cambridge University); **O. Kashuba** (Institute for Theoretical Physics, RWTH Aachen); **V. I. Fal'ko** (Lancaster University)

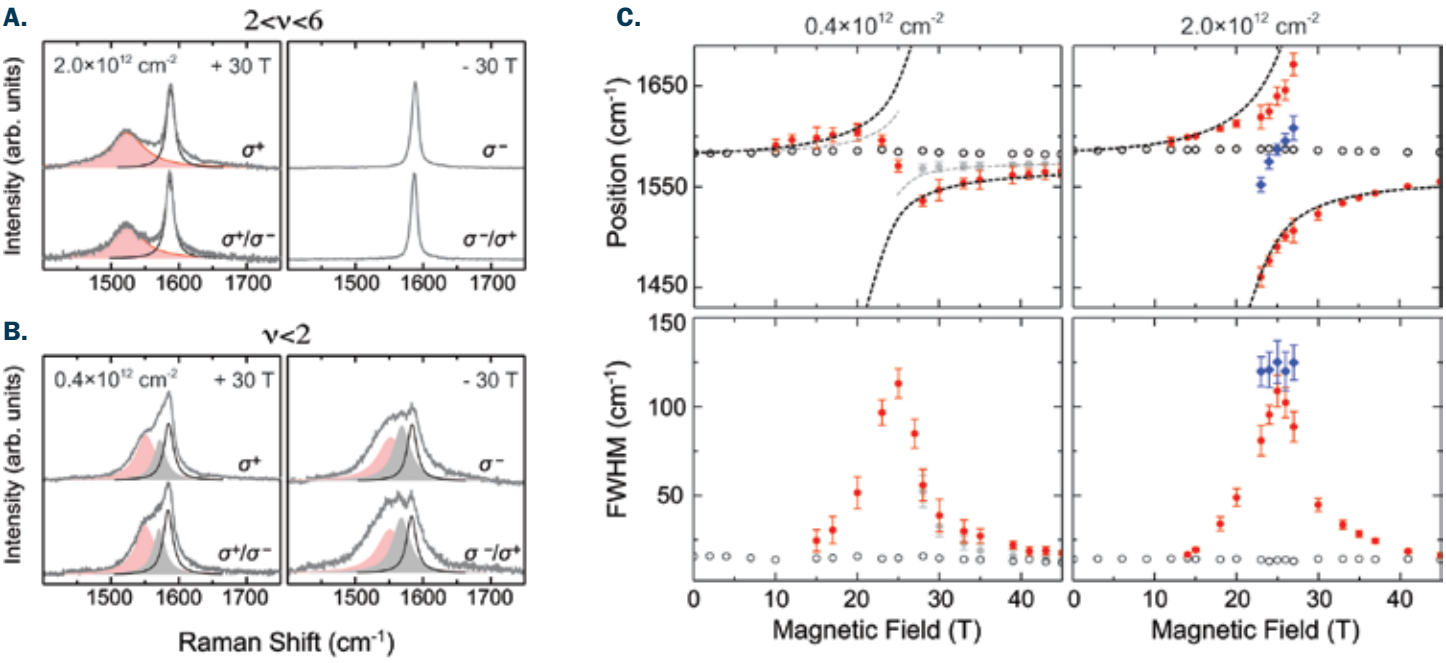


FIGURE 1. A. & B. Circular-polarized magneto-Raman spectra of graphene measured at 30 T. **C.** Peak position and FWHM the G peak Lorenzian components as a function of magnetic field.

Introduction

Central to the problem of understanding properties of condensed matter is the interplay between low energy excitations, such as electron-phonon coupling (EPC). In graphene, the Raman G peak is predicted to exhibit anticrossings when the energy of the zone-centre E_{2g} phonon matches the separation of the Landau levels (LLs). This magneto-phonon resonance (MPR) effect can be described as a resonant mixing of electronic and lattice excitations into a combined mode, leading to a splitting proportional to the EPC. A unique feature of MPR in graphene, is the filling-factor dependence of the anticrossing structure of coupled modes, as well as a possibility to resolve the MPR of circularly polarized phonons.[1]

Results & Discussion

Here, we report a polarization-resolved Raman spectroscopy study of MPR in graphene.[2] Measurements were performed at 300K for B up to 45 T using a high-field magneto-Raman insert, as for Reference 3. By varying the filling factor (ν) through chemical doping, we identified different types of G peak B-field dependencies, providing a comprehensive evidence of MPR on

circularly polarized phonons. At high carrier density ($\nu>6$), the G peak does not reveal MPR splitting. For $2<\nu<6$, the G peak exhibits a strong anticrossing reaching ~150cm^{-1} (~20meV) for B=25 T. The electron-phonon coupled modes appear only in the σ+ and σ+/ σ- geometry, while the G peak does not split nor shift in σ- and σ-/ σ+ polarizations. For $\nu<2$, the coupled modes appear in both σ+ and σ-polarizations. Moreover, the spectra for the $2<\nu<6$ case show an additional component, indicated in blue in **Figure 1C.** This unexpected increase of Raman intensity in the middle of the anticrossing gap is assigned to mixing and splitting of electron-phonon coupled modes caused by fluctuations of strain-induced pseudo-magnetic fields.

Acknowledgements

We acknowledge funding by NHMFL UCGP-5068, DOE/BES DE-FG02-07ER46451, DOE/BES DE-FG02-06ER46308, the Robert A. Welch Foundation C-1509, EPSRC grants GR/S97613/01, EP/E500935/1, ERC grant NANOPOTS, EU grants GENIUS and RODIN, two Royal Society Wolfson Research Merit Awards, NSF ECCS 0925988, ERC AdG 'Graphene and Beyond'.

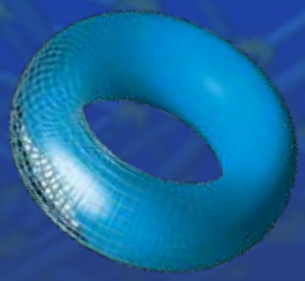
REFERENCES

1. M.O. Goerbig *et al. Phys. Rev. Lett.* **99**, 087402 (2007).
2. Y. Kim *et al., Phys. Rev. Lett.* **110**, 227402 (2013).
3. Y. Kim *et al., Phys. Rev. B* **85**, 121403(R) (2012).

JANUARY 6-10, 2014

THEORY WINTER SCHOOL

at the MagLab in Tallahassee, FL



LECTURE FOCUS

TOPOLOGICAL PHASES OF CONDENSED MATTER
– a subject of great interest in Condensed Matter and Materials Research Theory.

POSTER SESSIONS

Junior participants will have the opportunity for direct exchange of ideas with lecturers and each other.

WHAT IS WINTER SCHOOL?

Theory Winter School is a five-day program bringing together leading experts in specific areas of research. Those experts present tutorial lectures to help expand interest in those fields.

Winter School primarily targets advanced theory graduate students and post-docs who can apply from any institution worldwide.

INVITED LECTURERS

JASON ALICEA – *Caltech*
TAYLOR HUGHES – *UIUC*
XIAO-LIANG QI – *Stanford*
NICK BONESTEEL – *FSU, MagLab*
JOEL MOORE – *Berkeley*
YING RAN – *Boston College*
LIANG FU – *MIT*
PHUAN ONG – *Princeton*
KUN YANG – *FSU, MagLab*

APPLICATION DEADLINE

September 30, 2013

To learn more and register, go to magnet.fsu.edu and search "winter school," or visit:

www.magnet.fsu.edu/winterschool

Graphene

In graphene, there are waves in the density of electrons, known as plasmons, which interact strongly with light and may allow much faster transmission of information than is possible in the current generation of electronics. From infrared (IR) transmission measurements of graphene microstructures performed at the NHMFL, it was found that the plasmon resonance peak at zero magnetic field splits into two modes when exposed to high magnetic fields and the plasmons at the edges of the microstructures show a longer lifetime when a magnetic field is applied. These findings may not only lead to new applications in magneto-optical devices such as optical modulators and Faraday rotators, but also open a new avenue to explore the physics of graphene at the edge of the device.

• Published in *Nano Lett.*, **12**, 3766 (2012).

Infrared Spectroscopy of Tunable Magneto-Plasmons in Graphene

Z. Li (NHMFL); **H. Yan, X. Li, W. Zhu, P. Avouris and F. Xia** (IBM)

Introduction

Due to its linear electronic band structure, the charge carriers in graphene behave as massless Dirac fermions. Graphene plasmons are collective oscillations of these fermions, which possess many fundamentally different properties from that of conventional two-dimensional plasmons involving carriers with non-zero mass. One of the differences is the carrier density dependence of the plasmon resonance frequency. As a result, the study of graphene plasmons emerges as a very dynamic and fast developing research field.

Experimental

We successfully performed far-IR transmission measurement of graphene disk arrays,[1] anti-dot arrays and ring arrays[2] under a magnetic field up to 17.5 T using SCM3. In our previous experiments, graphene samples were grown by chemical vapor deposition (CVD) and then transferred to proper substrates. We used electron beam lithography and oxygen plasma etching to define graphene disks. IR transmission spectra were measured using a Fourier transform spectrometer at SCM3 of NHMFL.

Results & Discussion

We investigated the optical response of the plasmons in micrometer-sized graphene disks in high magnetic fields up to 17.5 T.[1] Our study shows that the plasmon resonance splits into edge and bulk modes in magnetic fields, as shown in **Figure 1**. Due to the linear band structure of graphene, the splitting exhibits a sensitive doping dependence, which is not observed in conventional two-dimensional electron gas systems[1]. Moreover, the lifetime of the two modes can be dramatically modified by magnetic fields, with the edge plasmons developing increasingly longer lifetimes (narrower linewidth) in high fields. The latter behavior can be understood from the suppression of backscattering at the edges.

Conclusions

Our findings, particularly the control of plasmon lifetime by magnetic fields, may lead to applications in magneto-optical devices, such as optical modulators and Faraday isolators. Moreover, this work opens a new avenue to explore the edge physics of graphene.

Acknowledgements

Part of this work was performed at the National High Magnetic Field Laboratory, which is supported by NSF DMR-0654118, the State of Florida, and DOE.

REFERENCES

1. H. Yan *et al., Nano Lett.* **12**, 3766 (2012).
2. H. Yan *et al., New J. of Phys.* **14**, 125001(2012)

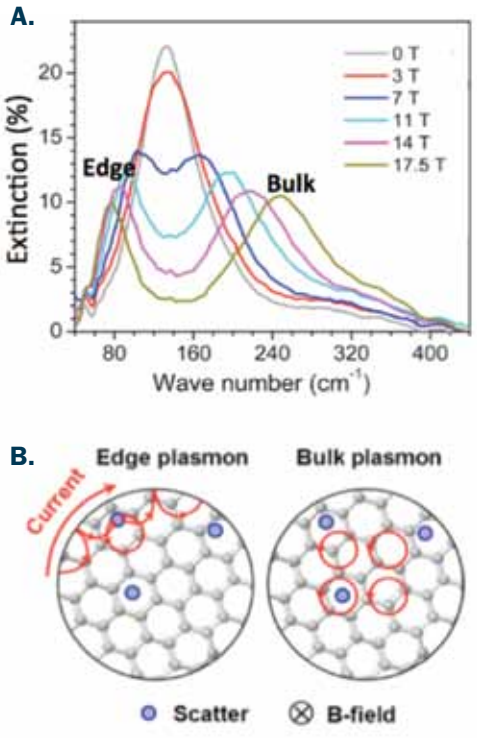


FIGURE 1. A. Extinction in transmission in graphene plasmonic micro-disks in zero and finite magnetic fields. The edge and bulk magneto-plasmons are indicated. **B.** Illustration of the charged carrier motion for the edge and bulk modes. Data were taken at SCM3 of NHMFL.

Graphene

This work is a theoretical study aimed at understanding the unusual electronic properties of Bilayer Graphene. The system is observed experimentally to exhibit unusual and potentially useful response to magnetic fields and more. This work builds upon a symmetry analysis of all allowed electronic couplings. From this analysis, phase transitions are predicted to occur where the computed flows diverge. The analysis is performed at and in the vicinity of the transition points, determining all the corresponding instabilities for each ray.

• Published in *Phys. Rev B,* **86**, 075467 (2012) (Chosen as an Editor's Suggestion)

Electronic Multicriticality in Bilayer Graphene

Oskar Vafek, Vladimir Cvetkovic and Robert Throckmorton (FSU/NHMFL)

Introduction

The low energy effective spectrum of bilayer graphene consists of a pair of Fermi points. At each, two parabolic bands touch. This makes the system susceptible to the effects of electron-electron (e-e) interaction and one expects to find an interaction driven symmetry broken state at low temperatures. In a series of earlier papers[1,2,3] we studied the problem within a zero temperature one-loop RG. Here we develop a finite temperature RG method in the weak coupling limit, demonstrating how either finite temperature or trigonal warping cut-off the RG flows. A finite bare interaction is therefore required in order to have a diverging flow, i.e., an instability toward a symmetry broken phase. We are able to solve the asymptotic behavior of the flows exactly and identify all the stable solutions which lead to a discovery of a rich phase diagram. The flows are studied numerically to determine the dependence of the symmetry breaking channel on the type of bare interaction. We find gapless nematic phase to be the leading instability in the case of forward scattering only (**Figure 1**). It is stable to addition of small finite back and/or layer imbalance scattering. The Hubbard model on bilayer graphene is studied and the results are found to be in agreement with the known exact results. The effect of perpendicular electric field on the phase boundaries is analyzed.

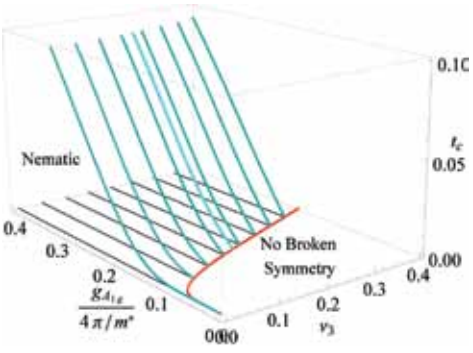


FIGURE 1.

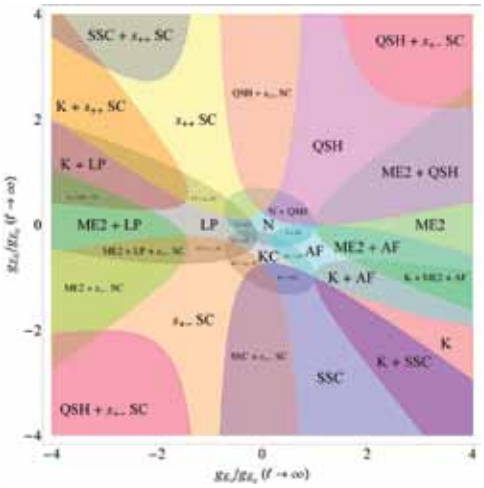


FIGURE 2.

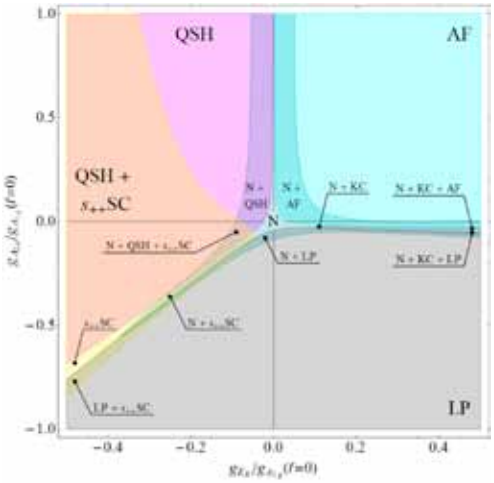


FIGURE 3.

Results & Conclusions

In this work we present the effective low energy theory for Bernal stacked bilayer graphene following symmetry analysis. The interacting problem is stated in the coherent state path-integral formalism at finite temperature. We find the flow equations for all 9 symmetry allowed couplings, as well as the flow for susceptibility toward all (relevant in the RG sense) symmetry breaking states. The transition is defined as the point where the flows diverge. These equations are analyzed at and in the vicinity of the transition point. We find all the possible stable rays for the RG flow ("target plane," **Figure 2**) and the corresponding instabilities for each ray. We consider repulsive density-density interactions and numerically determine the phase diagram (**Figure 3**) as a function of back and layer imbalance scattering (corresponding to the interaction range). The gapless nematic phase, the instability in the case of forward scattering only, is found to be stable to addition of small finite back and/or layer imbalance scattering. The increase of repulsive backscattering leads to anti-ferromagnetic ground state. Other possible ground states for these realistic interaction

parameters we find are layer polarized, Kekule current, quantum spin Hall, and s++-superconducting state. We study the Hubbard model on bilayer graphene lattice and show that the SO(4) symmetry of this model is preserved at all scales. Therefore, we predict that layer polarized and s++-superconducting state have the same susceptibilities in the Hubbard model (repulsive or attractive), and numerically determine these to be the instabilities in the case of attractive Hubbard model, whereas, the repulsive Hubbard interaction leads to anti-ferromagnet. Breaking the SO(4) symmetry with a small finite nearest neighbor interaction term favors either layer polarized or s++-superconducting state depending on the sign of the symmetry breaking term.

Acknowledgements

Supported by the NSF CAREER award under Grant No. DMR-0955561, NSF Cooperative Agreement No. DMR-0654118, and the State of Florida. A part of this work was completed at KITP-UCSB, and supported in part by NSF Grant No. PHY-0551164.

REFERENCES

1. O. Vafek, and K. Yang, *Phys. Rev. B* **81**, 041401(R) (2010).
2. Oskar Vafek, *Phys. Rev. B* **82**, 205106 (2010).
3. R.E. Throckmorton, and O. Vafek, *Phys. Rev. B* **86**, 115447 (2012) .
4. V. Cvetkovic, R.E. Throckmorton, and O. Vafek, *Phys. Rev. B* **86**, 075467 (2012).

Kondo/Heavy Fermion Systems

Progress towards describing quantum criticality depends on measuring the Fermi surface, possible only in specimens with exceptionally high purity. Emergent behavior near a QCP is often strongly influenced by chemical/structural disorder so that the number of heavy fermion systems where the intrinsic quantum critical behavior has been observed is extremely limited (e.g., $CeRhIn_5$).

To address this problem, high purity specimens of the correlated electron antiferromagnets Ce2Rh3Ge5 and Ce2Pt3Si5 were synthesized at MPA-CMMS, LANL. $Ce_2Rh_3Ge_5$ is particularly interesting because the pressure needed to access its QCP is extremely low (P_c ~ 0.45 GPa).[1] In contrast, T_N for $Ce_2Pt_3Si_5$ is unchanged up to P < 1.5 GPa.[2] At ambient pressure and zero magnetic field, these compounds are otherwise similar, with Neél temperatures (T_N) 4.7 K and 6.4 K, respectively. $Ce_2Rh_3Ge_5$ is unusual in that the pressure needed to access its QCP is extremely low (Pc ~ 0.45 GPa). In contrast, T_N for $Ce_2Pt_3Si_5$ is unchanged up to 1.5 GPa. This difference suggests that the mechanism which produces the low pressure QCP in $Ce_2Rh_3Ge_5$ is not present in $Ce_2Pt_3Si_5$. Any theoretical description of quantum criticality will need to be able to explain this type of difference between seemingly similar compounds.

To explore the relationship between these compounds, we undertook measurements at the pulsed field facility at the NHMFL - Los Alamos, which reveal that an applied magnetic field suppresses T_N to 0 at similar magnetic fields (H_c = 22 T and 36 T for $Ce_2Rh_3Ge_5$ and $Ce_2Pt_3Si_5$, respectively), indicating comparable magnetic energy scales. In addition, we observed quantum oscillations in both compounds, a result necessary to characterize their respective Fermi surfaces. The contrasting behaviors of $Ce_2Rh_3Ge_5$ and $Ce_2Pt_3Si_5$ under applied pressure and magnetic field, and our observation of quantum oscillations may provide the information for us to develop an understanding of the easy pressure tuning of $Ce_2Rh_3Ge_5$ but not for $Ce_2Pt_3Si_5$. This information will contribute to developing the theoretical framework for understanding quantum criticality in heavy fermion magnets.

Quantum Oscillation Measurements in Cerium 235s

R.E. Baumbach, E.D. Bauer, X. Lu, R.D. McDonald, F. Ronning, J.D. Thompson (LANL, MPA-CMMS)

Introduction

It is generally accepted that progress in describing quantum criticality depends on determining how the Fermi surface (FS) evolves at the quantum critical point (QCP). To do this, it is necessary to study specimens with exceptionally low crystalline disorder. As a result, the number of heavy fermion (HF) systems where FS reconstruction and QC behavior has been observed is limited (e.g., $CeRhIn_5$). To address this problem, high purity specimens of the HF antiferromagnets $Ce_2Rh_3Ge_5$ and $Ce_2Pt_3Si_5$ were synthesized in the MPA-CMMS group at LANL (T_N = 5.5 K and 6.3 K, respectively). $Ce_2Rh_3Ge_5$ is particularly interesting because the pressure needed to access its QCP is extremely low (P_c ~ 5 kbar).[1] In contrast, TN for $Ce_2Pt_3Si_5$ is unchanged up to P < 15 kbar.[2] In our recent measurements using the MagLab facility at LANL, we undertook to measure quantum oscillations in these compounds in order to quantify their FSs and thereby understand their contrasting behavior, as well as to lay the groundwork to study the FS in $Ce_2Rh_3Ge_5$ across the P driven QCP.

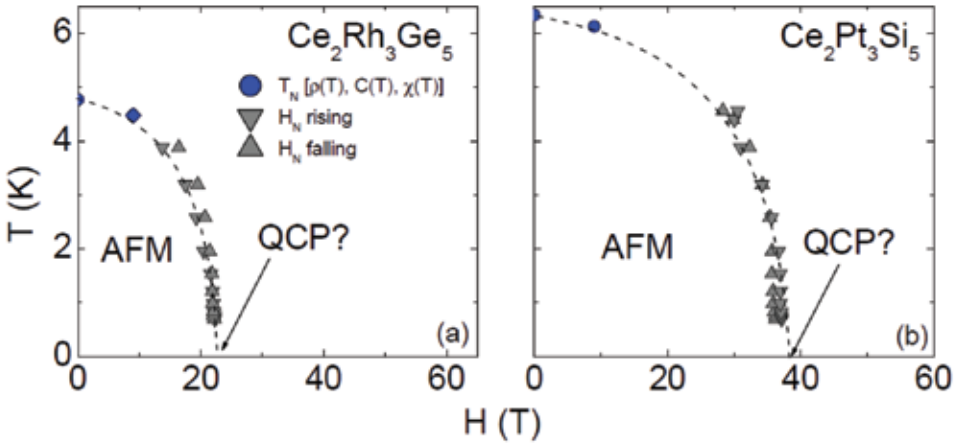


FIGURE 1. Temperature – magnetic field (T-H) phase diagrams for $Ce_2Rh_3Ge_5$ and $Ce_2Pt_3Si_5$ constructed from TDO/PDO measurements.

Experimental

Tunnel diode oscillator (TDO) and proximity diode oscillator (PDO) measurements were performed for temperatures 0.4 K < T < 30 K and magnetic fields

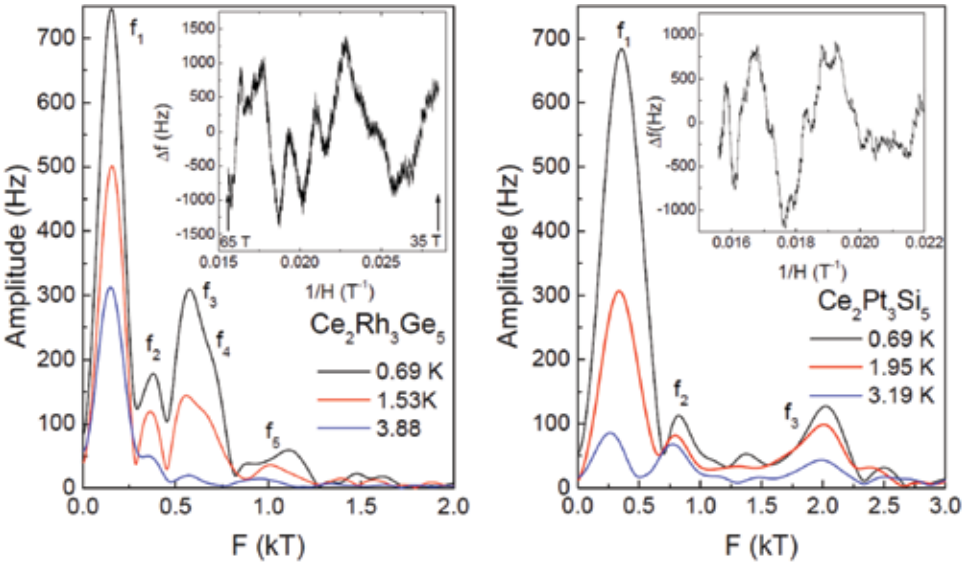


FIGURE 2. Main panels: Fourier transform of the oscillations in Ce2Rh3Ge5 and Ce2Pt3Si5. Insets: Raw TDO data at 0.69 K (after background subtraction) showing quantum oscillations.

H < 60 T for $Ce_2Rh_3Ge_5$ and $Ce_2Pt_3Si_5$ at the pulsed magnetic field facility at LANL.

Results & Discussion

Unexpectedly, we find that the antiferromagnetic ground state is suppressed to T = 0 at similar magnetic fields (H_c = 23 T and 36 T, respectively) (**Figure 1**) for $Ce_2Rh_3Ge_5$ and $Ce_2P_{t3}Si_5$. This result suggests comparable magnetic energy scales in these compounds and is in contrast to what is found in pressure experiments. Therefore, it seems that although these compounds are markedly similar, the mechanism that yields the pressure driven QCP in $Ce_2Rh_3Ge_5$ is not present in $Ce_2Pt_3Si_5$. We are currently investigating differences between these compounds and the mechanisms for their quantum criticality. In particular, our pulsed field measurements allow us to quantify the Fermi surface in each compound, which will be useful to develop a fundamental understanding of their physical properties (**Figure 2**).

Conclusions

We have identified previously unknown magnetic field driven quantum phase transitions in $Ce_2Rh_3Ge_5$ and $Ce_2Pt_3Si_5$. We have also measured quantum oscillations at high magnetic fields for both compounds. Together, these results will help to develop an understanding of their quantum critical behavior.

Acknowledgements

This work was supported by the US Department of Energy, Office of Basic Energy Sciences, Division of Materials Sciences and Engineering, PECASE funding from the US DOE, OBES, Division of Materials Science and Engineering, and funded partly by the Los Alamos Laboratory Directed Research and Development program.

REFERENCES

1. Umeo, K., *et al., Phys. Rev. B*, **64**, 144412 (2001).

2. Baumbach, R.E., *et al.*, manuscript in preparation.

Magnetism & Magnetic Materials

Magnetic frustration, spins on a triangular lattice, in this case spin ½ on Cu in $SrCu_2(BO_3)_2$, show a number of magnetization plateaus and magnetic textures in applied fields. Here, the new 100 T pulse field magnet was used to measure the magnetostriction of a sample of $SrCu_2(BO_3)_2$ to a field of 100.75 T. The results clearly show two new plateaus, one at 73.6 T, the other at 82 T, which are attributed to magnetization plateaus of 2/5 and 1/2 μ_B/Cu atom. This result is also a demonstration of the potential of the 100 T pulsed magnet.

• Published in *Proc. Natl. Acad. Sci. U.S.A.*, **109**, 12404 (2012)

Magnetostriction and Magnetic Texture to 100.75 Tesla in Frustrated $SrCu_2(BO_3)_2$

M. Jaime, S. Crooker and A. Uchida (LANL, NHMFL); **R. Daou** (MPI, CPfS); **F. Weickert** (LANL, CMMS); **A.E. Feiguin** (Univ. of Wyoming, Physics); **C.D. Batista** (LANL, T4); **H.A. Dabkowska and B.D. Gaulin** (McMaster, Physics)

Introduction

Strong geometrical frustration in magnets leads to exotic states such as spin liquids, spin supersolids, and complex magnetic textures. $SrCu_2(BO_3)_2$, a spin-1/2 Heisenberg antiferromagnet in the archetypical Shastry–Sutherland lattice, exhibits a rich spectrum of magnetization plateaus and stripe-like magnetic textures in applied fields. The structure of these plateaus is still highly controversial due to the intrinsic complexity associated with frustration and competing length scales. We discover magnetic textures in $SrCu_2(BO_3)_2$ via magnetostriction and magnetocaloric measurements in fields up to 100.75 T. In addition to observing low-field fine structure with unprecedented microstrain resolution, the data also reveal lattice responses at 73.6 T and at 82 T that we attribute, using a controlled density matrix renormalization group approach, to a unanticipated 2/5 plateau and to the long-predicted 1/2 plateau.[1]

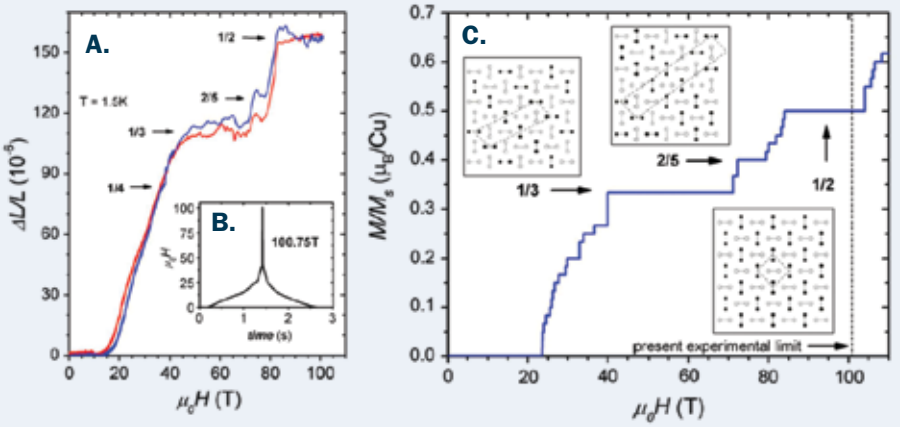


FIGURE 1. A. Magnetostriction vs. magnetic field for ΔL‖H‖ c-axis measured in a 100 T (red and blue) pulsed magnet. Data taken during field upsweep (red) and downsweep (blue) are included. Two new features at 73.4 T and 82.4 T in the high field data are attributed to the onset of the 2/5 and 1/2 magnetization plateaus. This sample was measured while held in place solely by the optical fiber used for magnetostriction. **B.** Field profile of the 100 T repetitively pulsed magnet at the National High Magnetic Field Laboratory. **C.** Normalized magnetization vs. field calculated using a Density matrix Renormalization Group technique in a 4 × 30 site lattice for J_0 = 78 K and J_1/J_0 = 0.62 showing that the most stable magnetization plateaus occur at 1/3, 2/5, and 1/2 of magnetization saturation. Inset: Solid circles represent $Cu2^+$ dimers occupied by spin triplet states, open symbols are spin singlet states, organized in the 1/3, 2/5 and 1/2 states.

Acknowledgements

A.F. acknowledges NSF funding under grant DMRG-0955707. Experiments at the High Magnetic Field Laboratory Dresden (HLD) (not shown) were sponsored by Euro-MagNET II under the EU contract 228043. Work at the NHMFL was supported by the National Science Foundation, the US Department of Energy, and the State of Florida. This research was also supported by the NHMFL Users Collaboration Grants Program (M.J.). M.J. and S.A.C acknowledge support by the U.S. DOE BES project "Science at 100 T"

REFERENCES

1. M. Jaime *et al., Proc. Natl. Acad. Sci* **109**, 12404 (2012).

Magnetism & Magnetic Materials

The magneto-electric effect, inducing an electric polarization via a magnetic field, has been studied in the triangular antiferromagnetic system $Ba_3NiNb_2O_9$. Different magnetic phases exist at different temperatures and magnetic field strength, and they induce an electric polarization that has been measured via the pyroelectric current. The presence of this electric polarization in magnetic collinear phases, however, requires additional symmetry breaking that may be produced by magnetostriction effects. Therefore an additional spin lattice coupling is needed to produce a macroscopic electrical polarization.
• Published in *Phys. Rev.* **109**, 257205 (2012).

Successive Magnetic Phase Transitions and Multiferroicity in Spin-1 Triangular Lattice Antiferromagnet $Ba_3NiNb_2O_9$

J. Hwang and P. Schlottmann (FSU Physics, NHMFL); **E.S. Choi and Y. Xin** (NHMFL); **F. Ye and C.R. Dela Cruz** (Oak Ridge National Lab); **H.D. Zhou** (NHMFL, Univ. Of Tennessee)

Introduction

We have investigated the magnetic phase transitions and magnetoelectric effect of a triangular lattice antiferromagnet (TLAF) $Ba_3NiNb_2O_9$. The TLAFs is one of the most simple geometrically frustrated magnets and has been known to show successive magnetic phase transitions of 120 degree AFM ordering, up-up-down (*uud*) and the oblique phase (coplanar 2:1 canted) with increased magnetic field.[1]

Experimental

The magnetoelectric effect (dielectric constant and the pyroelectric current) and the AC susceptibility were measured on polycrystalline samples using the SCM2 magnet. The DC magnetization measurement was done with a vibrating sample magnetometer in cell 8 with the 35 T resistive magnet.

Results & Discussion

The dielectric constant anomaly (not shown) and the emergence of spontaneous, reversible polarization at low temperatures suggest ferroelectric ground state, whose para-ferroelectric phase boundary also matches with those of magnetic phase transitions as shown in **Figure 3**. The DC magnetization and AC susceptibility studies (**Figure 2**) confirmed magnetic phase transitions following the theoretical prediction with change of spin structures as depicted in **Figure 3**. One notable feature is the multiferroicity in the *uud* and the oblique phase, where the inversion symmetry in the collinear spin structures with underlying triangle lattice does not allow ferroelectric ground state. We speculate a distortion of the triangle lattice driven by magnetostriction breaks the inversion symmetry in favor of the observed multiferroicity.

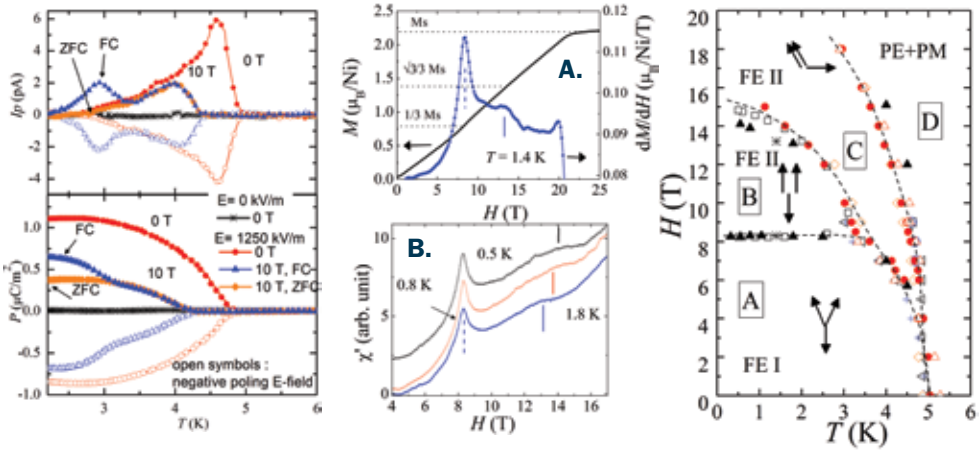


FIGURE 1. (LEFT) The T-dependence of the pyroelectric current (Ip) and the polarization (P) of $Ba_3NiNb_2O_9$.
FIGURE 2. (CENTER) The H-dependence of the **A.** DC magnetization and its derivative (dM/dH) **B.** AC susceptibility of $Ba_3NiNb_2O_9$.
FIGURE 3. (RIGHT) H-T phase diagram for $Ba_3NiNb_2O_9$ from different experimental techniques (please see Reference 2 for detail).

Acknowledgements

This work was supported by NSF-DMR-0654118, the State of Florida and DOE (DE-FG02-98ER45707). "The work at ORNL was supported by Scientific User Facilities Devision, Office of Basic Research, DOE."

REFERENCES

1. Chubkov A.V. and Golosov D.I., *J. Phys. Condens. Matter* **3**, 69 (1991).
2. Hwang J. *et al.*, *Phys. Rev. Lett.* **109**, 257205 (2012).

Magnetism & Magnetic Materials

A record high magnetic hysteresis has been observed in the compound Sr_3NiIrO_6. Single crystals of this compound were measured at low temperatures in fields up to 60 T. With proper alignment, the hysteresis loop shows a record coercive field in excess of 40 T. This extraordinary coercive field is attributed to the strong anisotropy of the Ir magnetic moments.

Giant Magnetic Hysteresis in Sr_3NiIrO_6

Craig Topping, Jae-Wook Kim, Eun-Deok Mun, John Singleton and Vivien Zapf (NHMFL-LANL); **Sang-Wook Cheong** (Rutgers University)

Introduction

Sr_3NiIrO_6 forms a trigonal structure in which Ni and Ir alternate in chains along the c-axis, and the chains form a hexagonal structure in the a-b plane.[1] It belongs to a family of compounds with similar structure including Ca_3CoMnO_6, $Ca_3Co_2O_6$, Sr_3CoIrO_6,[1,2] and others. These materials can have highly frustrated magnetic interactions and in the case of Ca_3CoMnO_6 show multiferroic properties. In particular, when the magnetic moments are Ising-like, these materials may be examples of the Axial Next Nearest Neighbor Ising model (ANNNI).[3] By substituting magnetic 5d Ir^{4+} into the structure, we have the potential to create a high degree of anisotropy. Previous measurements on polycrystals of Sr_3NiIrO_6 show magnetic hysteresis below ~50 K, and a feature in the magnetic susceptibility below 85 K.[1] X-ray absorption of other family members suggest that Ni, which occupies a trigonal bipyramid of oxygen, is divalent and Ir, which occupies an octahedral oxygen cage, is tetravalent.

Experimental

We measured extraction magnetometry in a short pulse magnet up to 60 T in polycrystals and in the first-reported single crystals of this material.

Results

Figure 1 shows the magnetization for H || ab and H || c for a single crystal grown from a Ni-rich flux with $Sr_3Ni_{1.05}Ir_{0.95}O_6$. We find an extremely large coercive magnetic field of 40 T at T = 4 K, in fact the highest coercive fields of any material to our knowledge. The magnetization is highly anisotropic, and for H || ab, the magnetization is roughly linear and not hysteretic in applied magnetic fields up to 60 T. This is consistent with the magnetic moments or their exchange interactions being highly anisotropic. In Ni-rich polycrystalline samples, coercive fields of up to 30 T were also observed.

Conclusions

We observe the highest coercive field (40 T) of any magnetic materials to our knowledge, which we attribute to the strongly anisotropic 5d Ir^{4+} moments. Further measurements are in progress.

Acknowledgements

The measurements at the NHMFL were conducted under the NHMFL core user program grant, funded by the NSF, the DOE, and the State of Florida.

REFERENCES

1. D. Mikhailova *et al., Phys. Rev. B* **86**, 134409 (2012); D. Flahout *et al., Eur. Phys. J. B* **35**, 317 (2003)
2. V. Hardy *et al., Phys. Rev. B* **70**, 064424 (2004); Y. J. Choi *et al., Phys. Rev. Lett.* **100**, 047601 (2008); V. Kiryukhin *et al., Phys. Rev. Lett.* **102**, 187202 (2009).
3. Y. Kamiya and C. D. Batista. *Phys. Rev. Lett.* **109**, 067204 (2012); W. Selke, *Phys. Reports* **170**, 213 (1988).

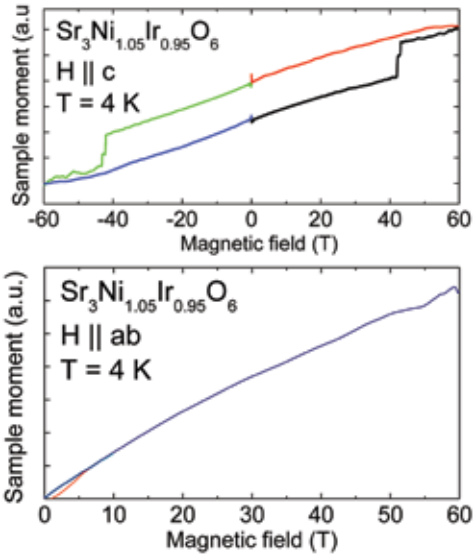


FIGURE 1. Magnetization of single crystalline $Sr_3Ni_{2-x}Ir_xO_6$ grown from a Ni-rich batch with x = 0.95. Measurements performed in a short pulse magnet to 60 T using an extraction magnetometer. The magnitude by 60 T is on the order of 2 mB for H || c and 1 m_B for H || a.

Magnetism & Magnetic Materials

Recent NMR experiments on the quasi-1D frustrated antiferromagnet $LiCuVO_4$ in the 45 T Hybrid magnet have confirmed for the first time the existence of a new exotic state of matter, called the spin-nematic phase, previously predicted only theoretically. Characterized by rotational symmetry breaking and an absence of long ranged spin order, the spin-nematic phase is analogous to liquid crystals and illustrates how such non-trivial quantum states appear in nature. In this system, the competing ferromagnetic nearest-neighbor and anti-ferromagnetic next-nearest-neighbor interactions result in a bound state of magnon pairs which undergo a Bose-Einstein Condensation (BEC) above a critical field of ~40 T.

Spin-nematic Phase in the S = 1/2 Antiferromagnet $LiCuVO_4$ Probed by NMR at 45 T

N. Büttgen (Center for Electronic Correlations & Magnetism, University of Augsburg/Germany); **M. Hagiwara** (KYOKUGEN, Osaka University/Japan); **P.L. Kuhns and A.P Reyes** (NHMFL); **L. Svistov** (Kapitza Institute, Moscow/Russia)

Introduction

From the well known values of the exchange integrals of the Cu^{2+} ions in $LiCuVO_4$, a long-range ordered spin-nematic phase for applied magnetic fields H in the vicinity of $\mu_0 H_{sat}$ = 45 T is predicted theoretically.[1] In this project we elucidate the fingerprint of spin-nematics with the local probes of NMR studying the nuclei of the nonmagnetic ions Li and V. For the spin-nematic phase a single-line shaped NMR spectrum is expected, where the NMR resonance field follows the magnetization M of the sample.

Experimental

We performed our NMR experiments of the ^{7}Li and ^{51}V nuclei using spin-echo techniques with a pulse sequence 3μs-τ-3μs in the hybrid magnet of the DC field facility, NHMFL, Tallahassee. All spectra were collected with τ=15μs by sweeping the applied magnetic field H at constant frequencies. Temperatures down to T = 380 mK were achieved within a ^{3}He cryostat.

Results & Discussion

Figure 1 shows the ^{51}V NMR spectra of the magnetically ordered phase at 380 mK within the range 34 < $\mu_0 H$ < 45 T of the applied magnetic field H oriented H || c. The origin at 0 T gives the diamagnetic reference field of the line shift. The double-horn shaped pattern for lower fields H at the bottom resemble our previous results,[2] where we established the spin-modulated magnetic structure in $LiCuVO_4$. Around the value of the applied magnetic field $\mu_0 H$ = 40.4 T (cf. arrows in **Figure 1**) the double-horn shape starts to disappear in favor of a single-line pattern with one solitary spectral line towards higher fields H. The transition takes place in a narrow field range, probably due to demagnetization fields of the single-crystalline sample. The single-line shaped pattern is maintained up to 45 T. The field dependence of the resonance positions of the ^{51}V spectra are shown in **Figure 2** (top panel, left axis). These local fields trace the magnetization data[3] (top panel, right axis,)up to fields $\mu_0 H$ ~ 41.4 T. For higher fields H the magnetization M is field dependent, whereas the NMR resonance is field independent. In **Figure 2** (bottom panel) μ_m is the mean magnetic moment of Cu^{2+} and μ_1 is the modulation strength of the spin-modulated structure.

Conclusions

Our NMR experiments establish the parameters of the spin-modulated phase in the full field range. At higher fields H > H_{c3}, the ^{51}V NMR line is single-line shaped, as it is expected for the spin-nematic phase. Additionally, μ_m detected from NMR spectra follows μ_m obtained from magnetization data only up to $\mu_0 H$ ~ 41.4 T. This evidences that spin-nematic correlations in $LiCuVO_4$ are active in the narrow field range 40.4 < $\mu_0 H$ < 41.4 T. Herein, the magnetization of the sample changes by 15…20 % of H_{sat}, satisfying theoretical predictions for 1D spin-chains.[4]

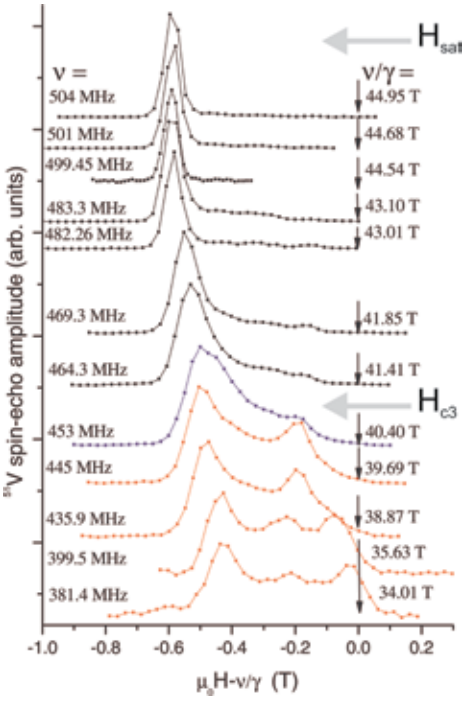


FIGURE 1.

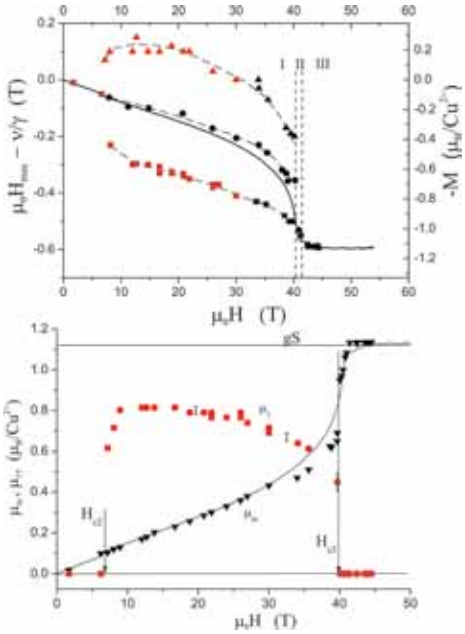


FIGURE 2.

Acknowledgements

Russian Foundation for Basic Research by Grants 12-02-00557-a, 10-02-01105-a of the Program of Russian Scientific Schools; the German Research Society (DFG) within TRR 80; and the NSF by NHMFL, Tallahassee.

REFERENCES

1. Zhitomirsky, M.E., *et al.*, *Europhys. Lett.* **92**, 37001 (2010); Sato, M., *et al.*, *Phys. Rev. Lett.* **110**, 077206 (2013)

2. Büttgen, N., *et al., PRB* **85**, 214421 (2012).

3. Svistov, L, *et al., JETP Letters* **93**, 21 (2011).

4. Heidrich-Meissner, F., *et al., PRB* **80**, 144417 (2009).

Magnetism & Magnetic Materials

Ghannadzadeh *et al.* have shown that external pressure can be used to drive a Jahn-Teller switch in $CuF_2(H_2O)_2(pyz)$, leading to an abrupt reduction in the magnetic dimensionality, providing the ability to tune the magnitude of the Cu-Cu exchange interaction *J* from 11.4 K to 5.5 K. This experiment is a great demonstration of the tune-ability and flexibility of this family of compounds, where magnetic interactions "by design" permit the manipulation of magnetic dimensionality and frustration, a true dream playground to test state of the art modeling, numerical computations and simulation.

• Published in *Phys. Rev. B.*, **87**, 241102(R) (2013).

Evolution of Magnetism in a Jahn-Teller Driven Magnetic Dimensionality Switch

S. Ghannadzadeh and P.A. Goddard (Oxford University); **S.W. Tozer and D. Graf** (NHMFL); **Jamie Manson** (Eastern Washington University); **J.A. Schleuter** (Argonne National Lab)

Introduction

Of interest is the effect of pressure on polymeric magnets based on hetero-ligand Jahn-Teller (JT) active metals centers, where the transition metal ion sits in a position of octahedral symmetry, surrounded by an asymmetric ligand environment. In such systems, each unique metal-organic ligand provides an additional degree of freedom on the JT-axis, meaning that small perturbations of the metal-ligand environment can be enough to switch the JT-axis and radically modify the material properties.

Recently it has been shown that $CuF_2(H_2O)_2(pyz)$ (see **Figure 1A**) undergoes two structural phase transitions as a function of pressure, accompanied by a switching of the JT-axis and orbital orientations. With the application of pressure, the elongated JT switches from the N–Cu–N to the O–Cu–O direction at 9 kbar.[1] At ambient pressure this material is a quasi-two-dimensional antiferromagnet (AFM), and so it has been proposed that this JT-axis switching and orbital reorientation may lead to a dramatic change of the magnetic behavior.

Experimental

The magnetization of single crystals of $CuF_2(H_2O)_2(pyz)$ was measured up to 35 T (NHMFL, Cell 12) using a novel radio-frequency technique.[2] All measurements were performed at 1.4 K, with the applied magnetic field parallel to the Cu–pyz–Cu chain direction (a-axis). A piston cylinder cell (MP35N) was used to achieve the pressure, which was calibrated in-situ using the luminescence of ruby.

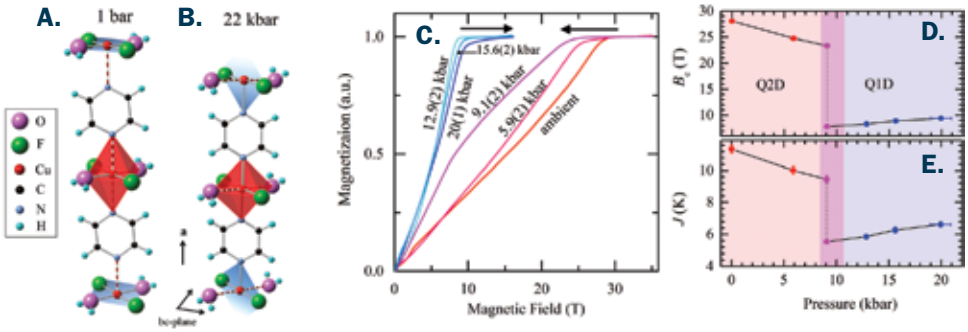


FIGURE 1. A. and **B.** Crystal structure along the a-axis[1], showing the JT octahedra (red) and the plane of the magnetic orbitals (blue). Also shown is **C.** the magnetization, **D.** the critical field and **E.** the exchange energy *J*, as a function of pressure.

Results & Discussion

$CuF_2(H_2O)_2(pyz)$ was found to be a two-dimensional AFM up to 6 kbar, with an exchange energy of approx. 11.4 K, which is reduced gradually with pressure due to distortions within the hydrogen-bonding motif. We observe a dramatic drop in the critical field and exchange energies at 9 kbar, a direct confirmation of a transition from two-dimensional to one-dimensional magnetism, due to the reorientation of magnetic orbitals associated with the JT-axis. This results in the primary exchange being mediated by pyrazine molecules via the Cu–pyz–Cu chain, thus allowing one-dimensional AFM to evolve. In this phase, we also observe a steady increase in the exchange energy *J* with pressure, which we attribute to a reduction in the Cu–N bond lengths.

Conclusions

We have shown that pressure can be used to drive a JT switch in $CuF_2(H_2O)_2(pyz)$, leading to an abrupt reduction in the magnetic dimensionality. It was demonstrated that pressure can be used to take control of the magnetic properties, providing the ability to tune the exchange energy *J* from 11.4 K to 5.5 K.

REFERENCES

1. Halder, G.J., *et al., Angew. Chem. Int. Ed.*, **50**, 419 (2011).
2. Ghannadzadeh, S., *et al., Rev. Sci. Instrum.*, **82**, 113902 (2011).
3. Ghannadzadeh *et al., Phys. Rev. B* **87**, 241102(R) (2013)

Quantum Fluids & Solids

The quantum magnet dichloro-tetrakis-thiourea-nickel (DTN) forms a magnetic order that is equivalent to a Bose-Einstein condensate (BEC) at ultra-low temperatures and high magnetic fields. It had been predicted that with the introduction of disorder the BEC state could be localized to form a Bose Glass. This BEC-Bose Glass transition has been observed in measurements of the magnetic susceptibility down to 1 mK at the High B/T Facility. The transition can be carefully controlled by magnetic field, allowing one to sensitively probe its properties and test the theory of boson localization.
• Published in *Nature*, **489**, 379-384 (2012)

Observation of a Bose Glass State in Doped Quantum Magnet

R. Yu (Rice U.)**; T. Roscilde** (ENS, Lyon)**; A. Padhuan-Filho and N. Oliveira** (Univ. Sao Paulo)**; V. Zapf, C.F. Miclea, F. Weickert, R. Movshovich, E.-D. Mun and B.L. Scott** (Los Alamos National Lab)**, S. Haas** (Univ. Southern Cal.)**; A. Steppke** (Max Planck Inst., Dresden)**; L. Yin and J. S. Xia** (Univ. Florida Physics)

Introduction

Dichloro-tetrakis-thiourea-nickel (DTN) consists of S=1 Ni^{2+} ions oriented along the c-axis and coupled in the a-b plane. The ground state is equivalent to that of a Mott insulator of bosons with each spin close to the $|m_s=0>$ state separated by an energy gap of about 3.8 K from the excited spin states. The application of a magnetic field of 2.1 T can close the gap leading to a Bose-Einstein condensation of the bosonic states. At much higher magnetic fields H ~ 12.2 T the spins become saturated and the system transits from a BEC to a Mott insulator. This is a particularly clean system for exploring the effect of disorder on the BEC transition because the Cl atoms can be readily replaced by Br thereby modifying the magnetic interactions. In this study the magnetization was measured for a single crystal sample with 8% Br substitution.

Experimental

The magnetic susceptibility of the doped DTN sample was measured at the NHMFL High B/T Facility as a function of temperature down to 1 mK and applied fields up to 15 T, using a high sensitivity magnetic susceptometer.[1] The temperatures were obtained using a $PrNi_5$ nuclear demagnetization refrigerator. Thermal contact to the sample was secured by immersing the sample in a bath of liquid ^{3}He.

Results & Discussion

The observed field dependence of the ac magnetic susceptibility is shown in **Figure 1**.[2] In contrast to the results for pure DTN[3] for which a single sharp transition is observed, a double transition is observed. This behavior is expected for a transition from the macroscopic BEC phase to a Bose glass state, followed by a transition to a Mott insulator.

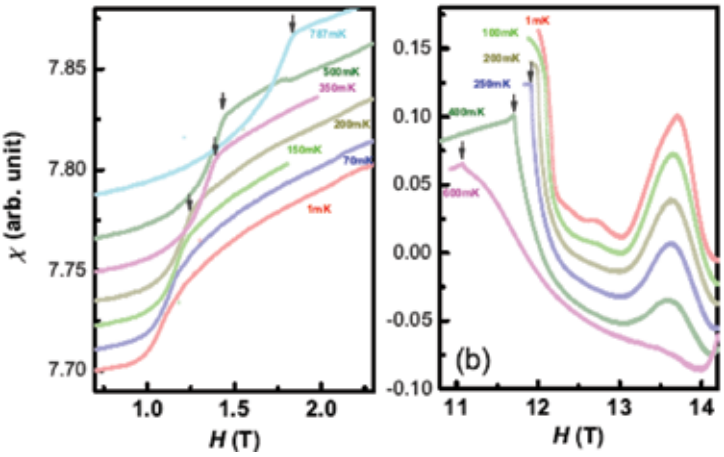


FIGURE 1. Field dependence of the ac magnetic susceptibility for Br-doped DTN at (i) the lower critical filed and (ii) the upper critical field. Clear evidence of a Bose glass state is seen for 12.2<H<13.5 T.

Conclusions

High sensitivity measurements of the magnetic susceptibility of a doped quantum magnet show the formation of regions of a Bose glass state on either side of the BEC phase for Br substituted dichloro-tetrakis-thiourea-nickel.

REFERENCES

1. Yin, L.; Xia, J.S.; Zapf, Z.; and Sullivan, N.S.; *J. Low Temp. Phys.* **158**, 710 (2010).
2. Yu, R. *et al.; Nature* **489**, 379 (2012).
3. Yin, L. *et al.; Phys. Rev. Lett.* **101**, 187205 (2008).

Quantum Fluids & Solids

Very clean two-dimensional electron systems in semiconductor quantum wells continue to reveal novel collective states arising from the dominance of the Coulomb interaction energy over the kinetic energy and the disorder potential. This report describes the observation of insulating phases near Landau level filling factors ν=4/5 and 6/5, more than twenty years after they were first anticipated.

• Published in *Phys. Rev. Lett.*, **109**, 036801 (2012).

Reentrant Integer Quantum Hall Effect in the Lowest Landau Level

Y. Liu, C.G. Pappas, M. Shayegan, L.N. Pfeiffer, K.W. West and K. W. Baldwin (Princeton Univ., Dept. of Electrical Engineering)

Introduction

It has been well established for over 20 years that an insulating phase, reentrant around the filling factor $\nu = 1/5$, is present in very high-quality 2D electron systems (2DESs). This phase is widely believed to be a manifestation of an electron Wigner crystal (WC) state, pinned by the disorder potential. Based on particle-hole symmetry, one would expect the appearance of similar insulating phases near filling factors $\nu = 1\pm1/5$ but, surprisingly, such phases have not been observed until now. We report here the first observation of reentrant integer quantum Hall effect (RIQHE) states in the lowest Landau level near $\nu = 4/5$ and 6/5 in very clean 2DESs confined to relatively wide GaAs quantum wells.

Experimental

Each of our samples consists of a GaAs quantum well bounded on its sides by undoped $Al_{0.24}Ga_{0.76}As$ spacer layers. The density (n) is controlled by carefully applying front- and back-gates, and keeping the charge distribution symmetric. The QHE measurements were carried out in SCM1 and resistive magnets.

Results & Discussion

Figure 1 highlights our main findings. A sharp contrast is seen in the data taken at two different densities in a 42-nm-wide GaAs quantum well. At the lower density, the R_{xx} and R_{xy} traces show what is normally seen in very clean 2DESs: strong QHE states at ν = 1 and 2/3 and, between these fillings, several fractional QHE states at ν = 4/5, 7/9, 8/11, and 5/7. At the higher density, however, a RIQHE (marked by down arrows in **Figure 1B**) is observed near 1/ν = 1.20, as evidenced by an R_{xx} minimum and an R_{xy} quantized at h/e^2. Also evident is a developing RIQHE state between ν = 4/5 and 7/9, evinced by a dip in R_{xy} (up arrow in **Figure 1B**), which becomes deeper at higher densities and R_{xy} approaches h/e^2.

We observe these RIQHE states only above a critical density (n_c) which is larger for narrower quantum wells. The RIQHE states can be interpreted as electron-hole counterparts of WC formed near ν = 1/5. In the present case, electrons at $\nu = 1\pm\nu^*$ can be considered as a filled Landau level, which is inert, plus excess electrons/holes with filling factor ν* which could conduct. At sufficiently small values of ν* and at very low temperatures, these excess electrons/holes crystallize into a WC phase which is pinned by disorder and does not participate in transport. Thus the magnetotransport coefficients R_{xx} and R_{xy} approach those of the ν = 1 integer QHE.

Conclusions

The RIQHE states in all samples are triggered by a sharp disappearance and reappearance of the ν = 4/5 FQH state near a critical density n_c, which is smaller in wider QWs. The ratio between the well width W and the magnetic length l_B is around 5~6 in all QWs. We believe it is the thick wave function in the z-direction that softens the short-range interaction and favors the formation of WC in our samples.

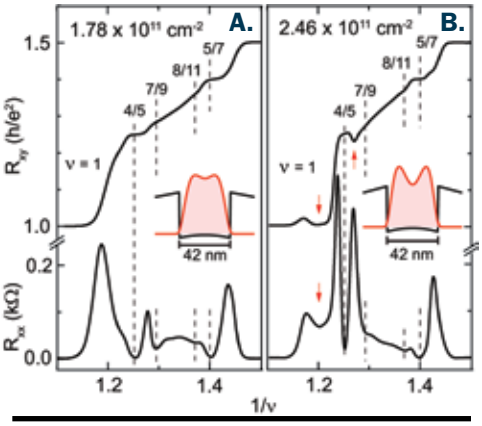


FIGURE 1. Rxx and Rxy vs. 1/ ν traces at T = 30 mK for a 42-nm-wide GaAs quantum well at two densities: **A.** n = 1.78, and **B.** 2.46 × 10^{11} cm^{-2}. In **B.** the RIQHE phases observed on two sides of $\nu = 4/5$ are marked by arrows.

Acknowledgements

This work was supported by NSF, DOE, and the Moore and Keck Foundations. We thank T. Murphy, J.H. Park, G. Jones and E. Palm for technical help.

REFERENCES

1. Y. Liu, C.G. Pappas, M. Shayegan, L.N. Pfeiffer, K.W. West, K.W. Baldwin, *Phys. Rev. Lett.* **109**, 036801 (2012).

Semiconductors

Alloying is a primary tool for tuning the optical and electronic properties of semiconductors for photovoltaic and solid-state lighting applications. The dilute nitride III-V alloys, such as $GaAs_{1-x}N_x$, are of special interest, but the effects of adding N to GaAs are not well understood. For example, discontinuous changes in the electronic properties of $GaAs_{1-x}N_x$ as a function of N concentration have been attributed to the percolation transition of N clusters, but probing their properties has been a challenge. This report demonstrates the use of a high magnetic field to reveal N cluster states, and to track and tailor their evolution through the percolation threshold.

• Published in *Phys. Rev. B*, **86**, 205203 (2012); *Phys. Rev. Lett.*, **110**, 156405 (2013).

Magneto-Photoluminescence Measurements of Dilute $GaAs_{1-x}N_x$

K. Alberi, B. Fluegel and A. Mascarenhas (NREL); **Scott A. Crooker** (NHMFL-Los Alamos)

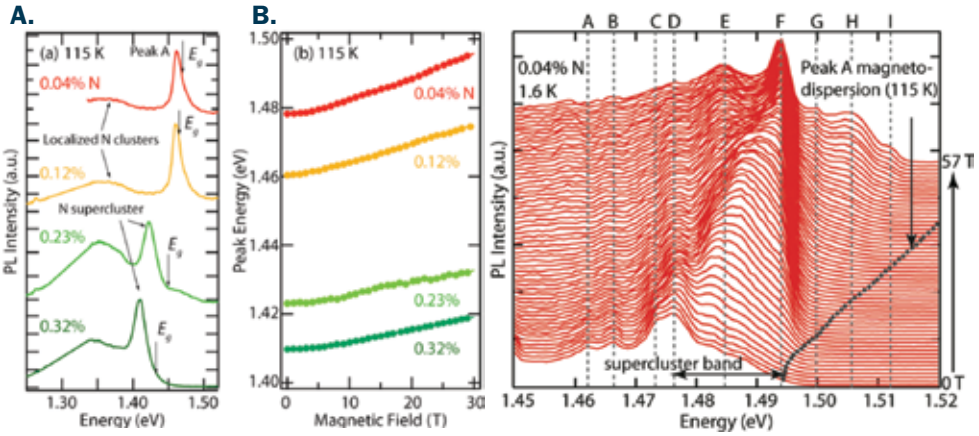


FIGURE 1. (LEFT) A. 0 T spectra of select $GaAs_{1-x}N_x$ samples. The bandgaps, E_g, as measured by electroreflectance, are marked with arrows. The PL peaks in samples with 0.23% and 0.32% N correspond to N superclusters **B.** PL peak energy as a function of applied magnetic field. The dispersion of the N supercluster peaks suggests that these states are delocalized.

FIGURE 2. (RIGHT) A. Magneto-PL spectra of the $GaAs_{1-x}N_x$ sample with 0.04% N. The magneto-dispersion of peak A in Figure 1 (measured at 115 K and shifted in energy to account for the temperature difference) is marked by black dots.

Introduction

GaAs exhibits unusual behavior upon the addition of dilute concentrations of N, including a strong drop in the bandgap energy, a sharp reduction in electron mobility and a large rise in the electron effective mass. Nitrogen is known to introduce a resonant level in the GaAs conduction band that modifies the electronic structure. However, bound states associated with N pairs and clusters are also thought to play a role in the transition of this material from isoelectronically-doped GaAs:N to a $GaAs_{1-x}N_x$ alloy. We demonstrate that localized N cluster states undergo a transition into an extended band of N-supercluster states at 0.23% N and form an associated mobility edge.[1] We additionally demonstrate that high magnetic fields can be used to tune the overlap of the N cluster states and reverse the transition.[2]

Experimental

Photoluminescence (PL) measurements on $GaAs_{1-x}N_x$ (0 to 0.5% N) samples were performed at the Los Alamos NHMFL with the 60 T Long-Pulse Magnet. Evolution of the PL from extended states as a function of magnetic field was probed at 115 K using a diode-pumped solid-state laser (515 nm), while the behavior of the localized N-cluster states was evaluated at 1.6 K.

Results & Discussion

Measurements performed at 115 K confirm that the bound N cluster states in samples with N concentrations less than 0.23% show no magneto-dispersion and are localized. The highest energy N cluster states in samples with higher N concentrations, on the other hand, exhibit a magneto-dispersion, suggesting that they form an infinite delocalized supercluster (**Figure 1**).[1] Furthermore, the application of very high magnetic fields ejects resonant N cluster states from the conduction band as it moves to higher energies.[2] Reduction of the exciton Bohr radius causes further fragmentation of the cluster states, producing sharp peaks in the PL spectra, as shown in **Figure 2**. The ability to controllably adjust the overlap of impurity states via a magnetic field presents a powerful avenue for investigating percolation-induced phenomena in a wide range of materials.

Acknowledgements

This work was supported by the Department of Energy Office of Science, Basic Energy Sciences (DE-AC36-08GO28308) and the NSF (NSF-DMR-0654118).

REFERENCES

1. Fluegel, B., *et al., Phys. Rev. B*, **86**, 205203 (2012).

2. Alberi, K., *et al., Phys. Rev. Lett.*, **110**, 156405 (2013)

Basic Superconductivity

Resonant Ultrasound Spectroscopy, a NHMFL signature technique, was enhanced and extended to explore the zero-field behavior of untwinned single crystal YBCO. The work, published in *Nature*, and with "News and Views" written about it also in *Nature*, and with a review article coming out in *Physics Today*, demonstrates the important NHMFL capabilities in technique development and instrumentation development essential for the successful pursuit of high-field studies on this system.

A) The measurements revealed a sharp kink in the T-dependence of the resonant frequency at the pseudogap line thus giving the ultimate proof of the thermodynamic character of transition into the pseudogap phase.

B) Most importantly, the pseudogap phase transition was detected under the superconducting dome at higher doping concentrations confirming, firstly, the existence of the highly anticipated quantum critical point on the phase diagram of cuprates; and, secondly, suggesting a competition between superconductivity and the pseudophase order parameter.

• Published in *Nature*, **498**, 75-77 (2013)

Resonant Ultrasound Spectroscopy (RUS) Measurements on Ultra-high Quality YBCO Single Crystal Cuprates

A. Shekhter, B. Ramshaw, J.B. Betts and A. Migliori (LANL, NHMFL); **R. Liang, W. Hardy and D. Bonn** (Physics, UBC, Canada)

Introduction

Recent polarized neutron diffraction measurements in underdoped cuprates of several families (YBCO,Hg1201,LSCO) reveal that the pseudogap phase, originally identified by anomalies in the Fermi surface structure and transport properties, is characterized by a distinct magnetic order. Resonant ultrasound spectroscopy is a natural tool to map and characterize the (doping-temperature-magnetic field) phase diagram in cuprates. One of the experimental challenges (specific to RUS probes) is the small size (sub-milligram range) of ultrahigh quality single crystal samples available today.

Experimental

At this stage, the work has been focused on a development of the RUS probe that works with crystals of very small size. There are several design goals: (i) achieving the free mechanical resonator conditions for these crystals, (ii) reducing the ultrasonic power to achieve linear elastic response, (iii) collect larger data set to increase accuracy of the determination of resonance frequency and width (iv) speeding up the measurement without compromising the quality of the data to achieve finer temperature steps in the obtained temperature evolution of elastic properties of the crystal. These goals have been met with the probe design that uses balsa wood as mechanical isolation effective in the broad temperature range and precision made pivot system to reduce load on a crystal during the measurement. Furthermore, to address goals (ii – iv), the software side of the measurement apparatus has been rethought from ground up. In particular, (i) the peak analysis software now uses full (in-phase and quadrature) information to determine resonance frequency and width and is much more robust against the noise. This yields high-quality data in a low power scans. Furthermore, the frequency scans over a large number of resonances has been sped up by about a factor of hundred without compromising the ring-up time by implementing a nonuniform in frequency scan across a set of resonance peaks that are adaptively followed as they move with temperature.

Results & Discussion

These measurements provide the first observation of the jump in the elastic moduli across the superconducting transition in cuprates. Such jump is required by thermodynamics of conventional superconductors. The temperature dependence of the resonance frequency has a sharp break in slope across the pseudogap phase

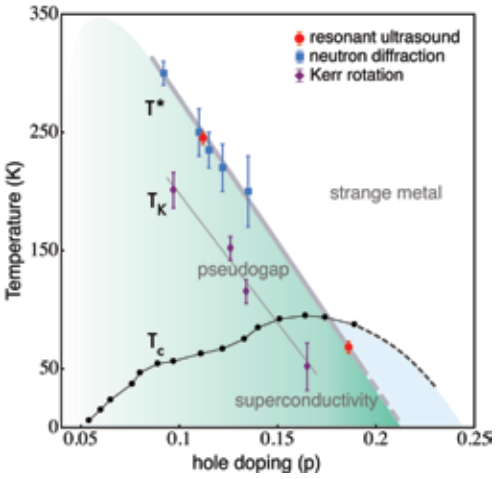


FIGURE 1. The phase diagram of YBCO cuprates. The pseudogap boundary in YBCO cuprates is indicated by a thick grey line (guide to the eye), as determined by neutron diffraction measurements (blue squares) and resonant ultrasound (red circles). The superconducting transition temperature is indicated by black circles. The temperature of the onset of Kerr rotation where recent X-ray measurements detect an onset of charge order is shown in purple diamonds. Error bars represent the uncertainty in the determination of the onset temperature. The thin grey line is a guide for the eye.

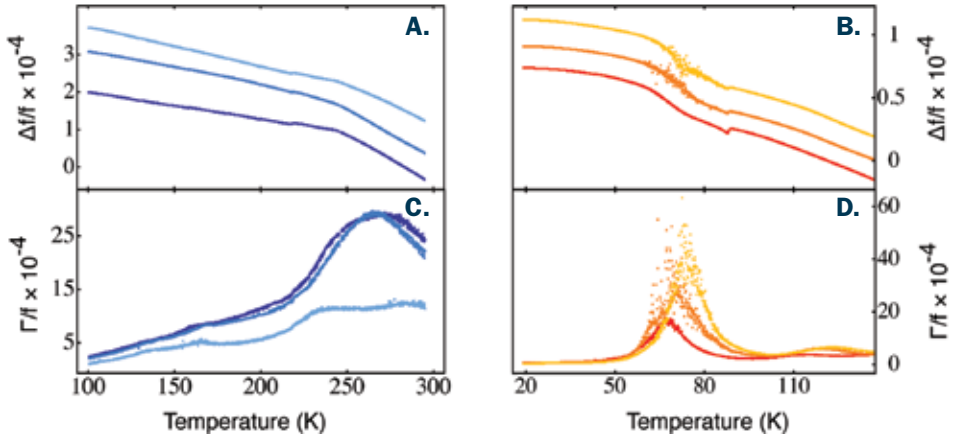


FIGURE 2. The temperature evolution of resonances across the pseudogap phase boundary. At both dopings a discontinuous change in slope of the temperature dependence of the frequency reveals a phase transition: underdoped **A.** at T^* = 245K, and overdoped **B.** at T^* = 68K. At both dopings the resonance width has a broad maximum above T^* (underdoped **C.** and overdoped **D.**). The break in slope is 5K wide in the underdoped crystal, 3K wide in overdoped. The increase in scatter of points near the break in slope in panel **B.** is a result of strong increase in resonance width at this temperature, panel **D**.

boundary — a standard thermodynamic signature for a phase transition. The width of the resonance (attenuation) reveals the complex dynamics with the physics of the pseudogap.

These measurements provide evidence for a phase transition at the pseudogap phase boundary. Furthermore, observation of the pseudogap transition below superconducting temperature in overdoped YBCO suggests that the pseudogap phase boundary has a termination point at zero temperature inside the superconducting dome.

Conclusions

The sophisticated resonance probe of elastic properties of the material has been demonstrated as a new and essential tool in studying the fascinating physical phenomena in modern condensed matter systems.

Acknowledgements

This work was supported by NSF, DOE, and the Moore and Keck Foundations. We thank T. Murphy, J.H. Park, G. Jones and E. Palm for technical help.

REFERENCES

1. Shekhter, A.; Ramshaw, B.J.; Liang, R.; Hardy, W.N.; Bonn, D.A.; Balakirev, F.F.; McDonald, R.D.; Betts, J.B.; Riggs, S.C. and Migliori, A., Bounding the pseudogap with a line of phase transitions in $YBa_2Cu_3O_{6+\delta}$, *Nature*, **498**, 75-77 (2013)

Basic Superconductivity

The use of the unique LANL facilities with high magnetic field up to 100 tesla made it possible to resolve the satellite frequencies of the quantum oscillations in underdoped YBCO that come about from splitting of the basic frequency due to the interlayer tunneling. (Beside the Fourier analysis, the authors employed the sinusoidal fits.)
• Published in *Phys. Rev. Lett.*, **108**, 196404 (2012)

Unprecedented Fermi Surface Spectral Resolution in the Underdoped High T_c Superconductor $YBa_2Cu_3O_{6+x}$ Obtained Using 100 Tesla Magnetic Fields

N. Harrison and **C.H. Mielke** (LANL); **S.E. Sebastian** and **G.G. Lonzarich** (Cavendish Lab., Cambridge Univ., UK); **R.-X. Liang, D.A. Bonn** and **W.N. Hardy** (Univ. British Columbia, Canada)

In signal processing, an increase in the time interval over which a signal is sampled leads to an increase in the amount of information that can be extracted within a given frequency bandwidth. The same principle also applies to the measurement of magnetic quantum oscillations in metals as a function of the reciprocal magnetic field. An increase in the range in reciprocal magnetic field over which quantum oscillations are measured (obtained by extending measurements to both lower and higher magnetic fields) leads to an increase in spectral information that can be extracted regarding the Fermi surface geometry.

The recent achievement of magnetic fields exceeding 100 tesla in the 100 tesla multishot magnet in Los Alamos provided the ideal opportunity to increase the resolution and precision to which the Fermi surface of the underdoped high T_c superconductor $YBa_2Cu_3O_{6+x}$ can be measured, enabling us to achieve substantial progress in our understanding of the origin of the small Fermi surface.[1]

A key distinguishing feature of the quantum oscillation waveform in underdoped $YBa_2Cu_3O_{6+x}$ is the beat pattern giving rise to nodes (at which the amplitude is suppressed) at $1/B = 0.033$ and 0.022 T^{-1}. A Fourier transform of the oscillations reveals the beat pattern in the dominant amplitude quantum oscillation frequency (of 534 T) to be caused by the presence of two smaller amplitude frequencies that are separated from the main frequency peak by +/- 90 T. The values of the frequencies obtained in the Fourier transform are further confirmed by performing sinusoidal fits to the quantum oscillation data.

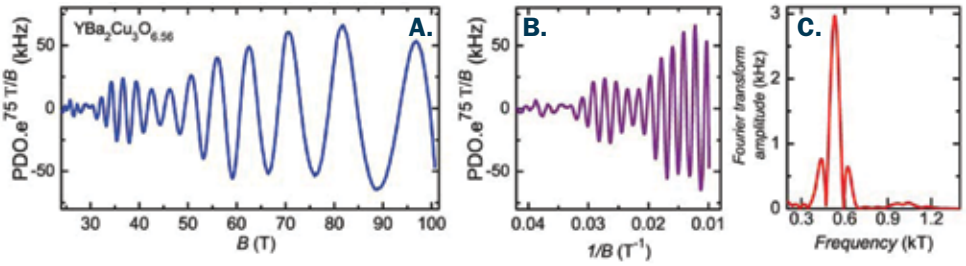


FIGURE 1. Quantum oscillations in $YBa_2Cu_3O_{6+x}$ obtained using the contactless conductivity technique shown versus magnetic field **A.** and reciprocal magnetic field **B**. **C.** shows a Fourier transform in which a Blackman window has been applied to the data.

Rather than corresponding to three individual sections of Fermi surface, the observed distribution of frequencies in which a central peak is equally flanked by two adjacent peaks of similar amplitude can be shown to be the simple consequence of quasiparticles tunneling between two concentric Fermi surface orbits that differ slightly in size.[2] Such an observation is expected for a bilayer Fermi surface that is split into separate bonding and antibonding cross-sections by the presences of a direct coupling between the layers. A simple model that includes the effect of the tunneling is shown to provide an explanation for both the frequency distribution and the magnetic field-dependent quantum oscillation amplitude and beat pattern.

Acknowledgements

We acknowledge support of the Department of Energy, Basic Energy Sciences project "Science at 100 tesla."

REFERENCES

1. Sebastian, S.E., *et al., Phys. Rev. Lett.*, **108**, 196403 (2012).
2. Yernoso, A.A., *et al., Phys. Rev. B*, **78**, 115312 (2008).

Basic Superconductivity

The vortex behavior in the iron-based high-Tc superconductors is a key point towards their application into technology, yet it still holds many surprises for us. By studying the flux flow in the "1111" SmFeAs (O,F) in the presence of the magnetic field oriented with high precision in the (ab) – plane and current along the c-direction, the authors have found a sharp increase in the flow and correspondingly, a decrease in the critical current. They successfully interpreted this phenomenon as a change in the structure of vortices from a "thick" 3d (Abrikosov) vortex to the interlayer Josephson vortices.
• Published in *Nature Materials*, **12**, 134-138 (2013)

Transition from Slow Abrikosov to Fast Moving Josephson Vortices in Iron-Pnictide Superconductors

P.J.W. Moll, J. Karpinski, N.D. Zhigadlo and B. Batlogg (ETH Zurich, Solid State Physics)**; V. Geshkenbein and G. Blatter** (ETH Zurich, Theoretical Physics)**; Luis Balicas** (NHMFL)

Introduction

Magnetic flux may penetrate superconducting systems, such as artificial Josephson junctions or the more anisotropic cuprate superconductors, in the form of Josephson instead of Abrikosov vortices, which occur in homogeneous materials. Typically these two phenomena are clearly separated by the materials interlayer coherence length; either one or the other is observed. We have investigated the vortex matter of the pnictide superconductor SmFeAs(O,F) with T_c~48-50K and found the superconducting parameters to conspire in such a way that both kinds of vortices exist in the same material in different temperature regimes, Abrikosov at high and Josephson at low temperatures[1]. Superconducting applications based on these compounds will always operate deep in the Josephson regime, thus the particular pinning of pancake segments in the iron-pnictides is found to be technologically most relevant.

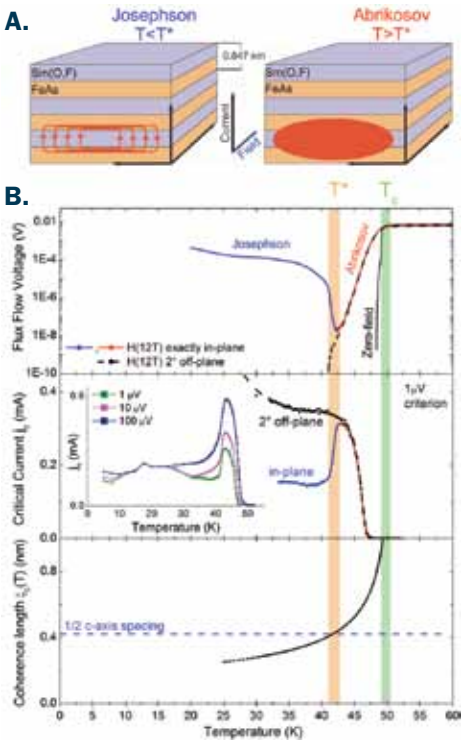


FIGURE 1. A. Sketch of a Josephson-vortex below T* and an anisotropic Abrikosov-vortex above T*. **B.** Flux-flow (FF) voltage and critical currents along the c-axis at 12 T, well aligned and 2° misaligned with the FeAs layers. These two cases are the same in the Abrikosov regime, but strongly differ in the Josephson regime: A sharp jump in FF voltage and a drop in critical currents signals the transition into the Josephson state.

Experimental

We have investigated the critical currents and flux flow voltages perpendicular to the FeAs layers in fields up to 35 T in a resistive magnet at the NHMFL in Tallahassee. Two main experimental challenges had to be overcome to observe Josephson vortex motion in the system: (1) Reliable transport measurements on micron-sized crystals shaped by the FIB[2] technique had to be performed and (2) precise and stable field alignment (<0.05°) with the FeAs layers is essential to observe the effect. This has been well achieved using the Cell 12 rotator.

Results & Discussion

We discovered a distinct change in the nature of the vortices from Abrikosov-like to Josephson-like upon cooling below a temperature T*~41-42K well below T_c~48-50K, despite its moderate electronic anisotropy γ~4-6. This transition is hallmarked by a sharp drop of the critical current and accordingly a jump of the flux flow voltage in a magnetic field precisely aligned along the FeAs layers, indicative of highly mobile vortices. T* coincides well with the temperature where the coherence length ξ_c perpendicular to the layers matches half of the FeAs-layer spacing (**Figure 1B**). For fields slightly out-of-plane (>0.1°-0.15°) the vortices are completely immobilized as well-pinned Abrikosov segments are introduced when the vortex crosses the FeAs layers. We interpret these findings as a transition from well-pinned, slow moving Abrikosov vortices at high temperatures to weakly pinned, fast flowing Josephson vortices at low temperatures.

Acknowledgements

This work was supported by DOE-BES through award DE-SC0002613, NSF through NSF-DMR-0084173, the State of Florida, the Swiss National Science Foundation SNF and the Swiss National Center of Competence in Research MaNEP.

REFERENCES

1. P.J.W. Moll, *et al., Nature Materials*, **12**, 134-138 (2013)
2. P.J.W. Moll, *et al., Nature Materials* **9**, 628-633 (2010)

Topological Matter

The discovery of mobile charge carriers at interfaces between insulating perovskite oxides has opened up new scientific opportunities, such as the investigation of 2D electron gases in $SrTiO_3$. Shubnikov-de Haas oscillations in a quantizing magnetic field establish the 2D character of these electron gases and elucidate their properties. Here, Shubnikov-de Haas oscillations are observed in $GdTiO_3/SrTiO_3$ heterostructures and used to confirm the 2D behavior of the electron gas at the interface. The Shubnikov-de Haas oscillations are attributed to the electrons in the strongly confined d_{xy}-derived subbands in $SrTiO_3$.
•Published in *Appl. Phys. Lett.*, **101** (15), 151604 (2012)

Quantum Oscillations from a 2D Electron Gas at a Mott/band Insulator Interface

P. Moetakef and S. Stemmer (UCSB, Materials); **D.G. Ouellette and S.J. Allen** (UCSB, Physics); **J.R. Williams and D. Goldhaber-Gordon** (Stanford, Physics)

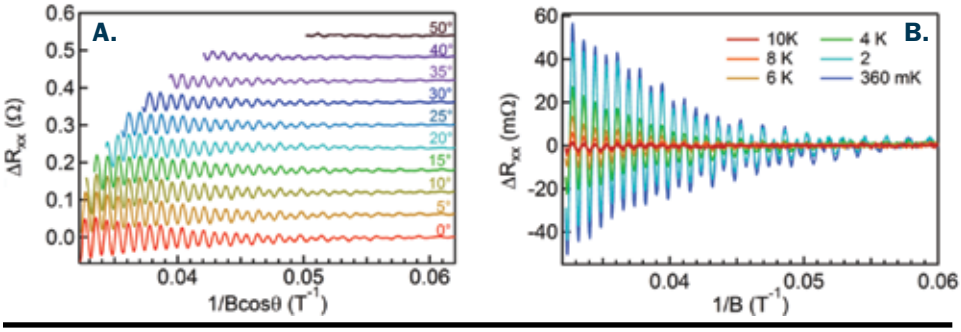


FIGURE 1. Shubnikov de-Haas oscillations as a function of **A.** tilt angle, and **B.** temperature.[1]

Introduction

The discovery of mobile charge carriers at interfaces between insulating perovskite oxides has opened up new scientific opportunities, such as the investigation of 2DEGs in $SrTiO_3$. Shubnikov-de Haas (SdH) oscillations in a quantizing magnetic field (B) establish the 2D character of these electron gases and elucidate the 2DEG properties. Several studies have reported on SdH oscillations from $LaAlO_3/SrTiO_3$ interfaces, which have mobile carrier densities on the order of ~10^{13} cm^{-2}. Further understanding can be obtained by examining alternative interfaces, such as $GdTiO_3/SrTiO_3$, which show mobile carrier densities (residing on the $SrTiO_3$ side) on the order of ~3×10^{14} cm^{-2}, closely corresponding to the density needed to compensate the polar discontinuity. The high carrier density is expected to produce tighter spatial confinement.

Experimental

$GdTiO_3$ and $SrTiO_3$ were grown on (001) $(LaAlO_3)_{0.3}(Sr_2AlTaO_6)_{0.7}$ single crystals by molecular beam epitaxy. The sample consisted of an 80 nm $SrTiO_3$ layer followed by an 8 nm $GdTiO_3$ layer. Magneto-transport measurements were performed with the contacts arranged in van der Pauw geometry on a 10×10 mm^2 sample in a 31 T magnet at the National High Magnetic Field Laboratory (NHMFL) at temperatures between 360 mK and 10 K. The sample was mounted on a rotator probe. The angle 0° indicates that B is perpendicular to the interface.[1]

Results & Discussion

The Hall mobility at 2 K was 322 cm^2/Vs. For B greater than 16 T, SdH oscillations were detected in measurements. The non-oscillating background was subtracted using multiple polynomial fits. **Figure 1A** shows the oscillations measured at 360 mK as a function of $(B\cos\theta)^{-1}$, for different tilt angles (θ) of the B-field. Simpler characteristics compared to oscillations reported for $LaAlO_3/SrTiO_3$ interfaces are observed. Periodic oscillations in $1/B$ and appearance of maxima (and minima) at the same $(B\cos\theta)^{-1}$ for all angles confirms the 2D behavior of the electron system. **Figure 1B** shows the oscillations measured at 0° at different temperatures from 360 mK to 10 K. The effective electron mass, m^*, was extracted from the temperature dependence of the oscillations and was found to be about 1.08 m_e (m_e is the free electron mass). This low effective mass points to the oscillations being due to the more strongly confined d_{xy}-derived subbands in $SrTiO_3$, which also explains their strongly 2D character.[1]

Conclusions

SdH oscillations observed in a $GdTiO_3/SrTiO_3$ sample confirmed the 2D behavior of the electron gas. The SdH oscillations were attributed to the electrons in the strongly confined d_{xy}-derived subbands in $SrTiO_3$.

Acknowledgements

We thank Alexey Suslov for help at the NHMFL.

REFERENCES

1. Moetakef, P., *et al., Applied Physics Letters* **101**, 151604 (2012).

Topological Matter

In as-grown crystals of the topological insulator (TI) Bi_2Te_2Se (BTS), the Fermi energy E_F typically lies high above the Dirac point, making the ordinarily-observed charge carriers more ordinary. This hampers the investigation of novel properties of the states near the Dirac point, the energy point where the carriers reflect the unusual properties of topological insulators. By using ionic liquid gating to tune the carrier energy, both the period and amplitude of the surface Shubnikov de Haas oscillations were observed to change systematically with the applied gating voltage. This approach provides a promising way to improve the quality of the topological insulator surface states.

• Published in *Phys. Rev. B* **88**, 035128 (2013).

Tuning the Quantum Oscillations of Dirac Surface Electrons in a Topological Insulator by Ionic Liquid Gating

J. Xiong, Y. Khoo, S. Jia, R.J. Cava and N.P. Ong (Princeton University)

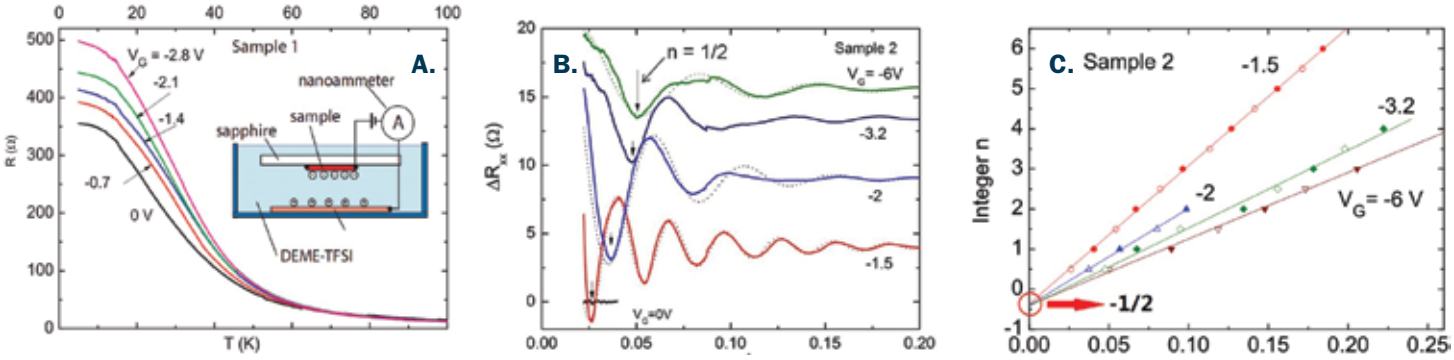


FIGURE 1. A. Plots of the resistance R vs. T in BTS for selected gate voltages V_g. The inset shows the cell used for IL gating. **B.** The SdH oscillations in MR for values of V_g = 0 to -6 V. Both the period and amplitude increase with $|V_g|$. **C.** The Landau index plot of the fields at the resistivity maxima vs. integers n. At all negative gating voltages, the intercepts in the limit $1/B \rightarrow 0$ gives $n = -½$ consistent with the π-Berry phase for the Dirac spectrum from Reference 1.

Introduction

In as-grown crystals of the topological insulator (TI) Bi_2Te_2Se (BTS), the Fermi energy E_F typically lies high above the Dirac point. This hampers the investigation of novel properties of the states near the Dirac point. We have used ionic liquid (IL) gating to tune E_F. Both the period and amplitude of the surface Shubnikov de Haas (SdH) oscillations were observed to change systematically with the applied gating voltage V_g. Analysis of the SdH period shows that E_F can be shifted towards Dirac point by ~50%. The surface mobility is also enhanced by IL gating. This approach provides a promising way to improve the quality of the TI surface states.

Experimental

Measurements were performed at the NHMFL in the 45 tesla hybrid (Cell 15). The BTS sample and Au gate electrode are immersed in the ionic liquid DEME-TFSI inside a cell as shown in the inset of Figure 1a. To set the gate voltage V_g, we warm the sample above the glass transition of DEME-TFSI (220 K).

Results & Discussion

The as-grown BTS crystals are n-type with resistivity values of 1-4 Ωcm at 4 K. As shown in **Figure 1A**, the sample resistance R at 4 K is increased by ~40% with V_g = -2.8 V, consistent with the depletion of bulk carriers by a negative V_g. **Figure 1B** plots the SdH oscillations in curves of R vs. B (a smooth background has been subtracted). Initially, at V_g = 0 V, the oscillations are too weak to be resolved, even at B = 45 T. However, at V_g = -1.5 V the SdH oscillations become well-resolved. As V_g is changed from 0 to -6V, we observe an increase in the oscillation period, consistent with a decrease in the 2D Fermi surface. At V_g = -6V, E_F is

reduced to only 88 meV above the Dirac point. The SdH amplitudes also increase with $|V_g|$, consistent with enhanced surface mobility. A fit to the standard Lifshitz expression gives a mobility of 3,000 $cm^2/(Vs)$ at V_g = -6V. **Figure 1C** plots the fields at the resistivity maxima vs. the integers. At 45 T, we have entered the n=1 Landau Level of the Dirac surface states. The combination of high *B* and IL gating allows the Berry phase in BTS to be determined more accurately. The extrapolation to $1/B \rightarrow 0$ gives an intercept at n = -1/2, confirming the π-Berry phase predicted for Dirac surface states.

Acknowledgements

The research is supported by grants from the National Science Foundation (DMR 0819860), the Army Research Office (ARO W911NF-11- 1-0379) and DARPA (SPAWAR Grant N66001-11-1-4110).

REFERENCES

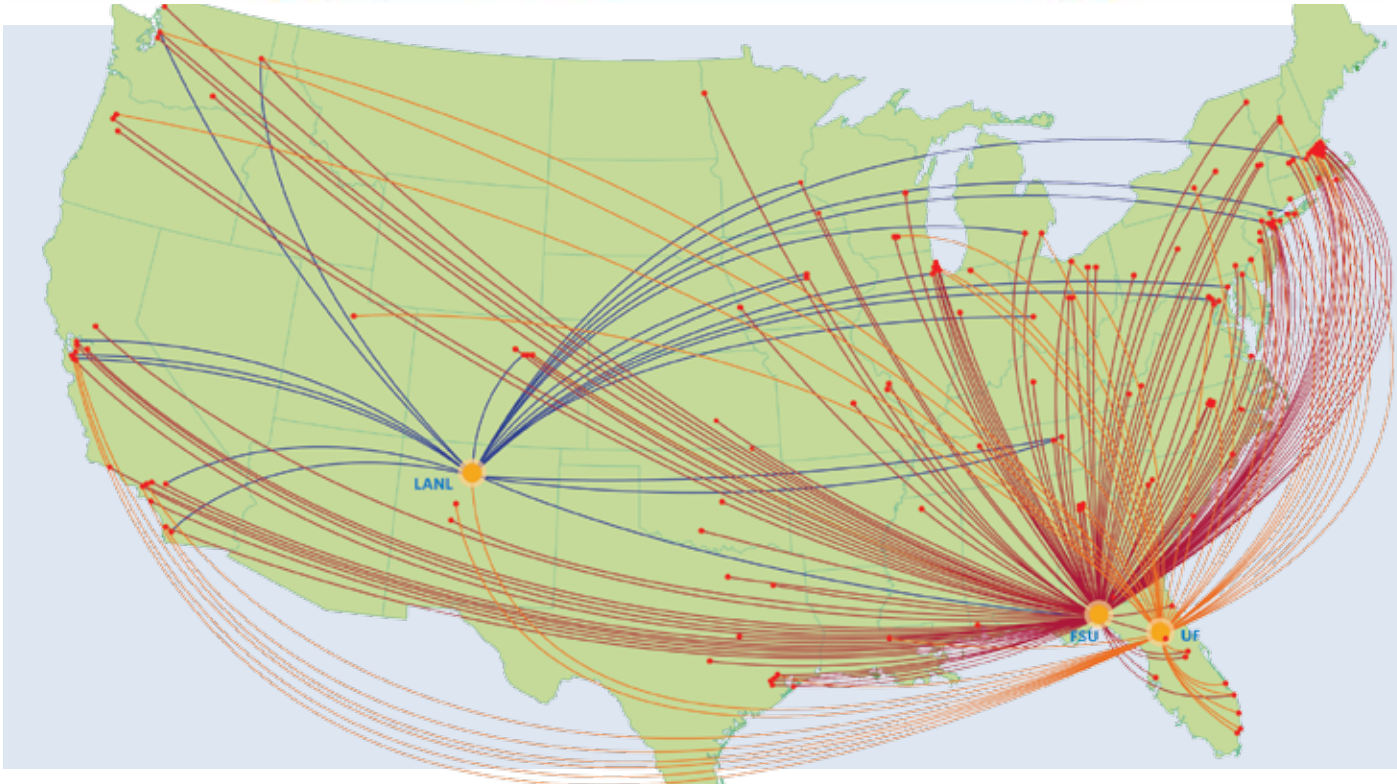
1. J. Xiong, Y. Khoo, S. Jia, R.J. Cava, N.P. Ong, "Tuning the quantum oscillations of surface Dirac electrons in the topological insulator Bi_2Te_2Se by liquid gating," arXiv: 1211.1906v2.

2. J. Xiong, Y. Khoo, S. Jia, R.J. Cava, N.P. Ong, *Phys. Rev. B* **88**, 035128 (2013).

MagLab users represent 159 univers companies in the United States and

In 2012, our facilities supported the science and engineering research projects of over 1





The Ame

- **BRAZIL** (4)
  Federal University o
  State University of F
  State University of C
  University of São Pa
- **CANADA** (16)
  Brock University
  Calfrac Well Service
  Environment Canad
  McGill University
  McMaster University
  Queen's University
  Sherbrooke Universi
  University of Alberta
  University of British
  University of Guelph
  University of New Br
  University of Otawa
  University of Saskat
  University of Toronto
  University of Victoria
  University of Windso

Europe &

- **BELGIUM** (1)
  Catholic University
- **DENMARK** (2)
  Aarhus University
  Haldor Topsoe

United S

- **WESTERN REG**
  Agilent Technologies
  Brigham Young Univ
  California Institute o
  Eastern Washington
  Huntington Medical
  Lawrence Berkeley N
  Lawrence Livermore
  Los Alamos National
  National Renewable
  NIST Boulder Labora
  New Mexico Tech
  Oregon Health & Sci
  Oregon State Univer
  Pacific Northwest Na
  Sandia National Lab
  San Diego State Uni
  SLAC National Accel
  Blue Marble Space I
  Stanford University
  University of Alaska,
  University of Californ
  University of Californ
  University of Californ
  University of Californ
  University of Californ
  University of Californ
  University of Californ
  University of Californ
  University of Colorad
  University of Colorad
  University of Oregon
  University of Southe

ities, government labs, and private 118 other institutions worldwide

1,350 users, about 30% of whom were graduate students and 13% were postdocs.

ricas (20)

f Pernambuco
Rio Grande do Norte
Campinas
ulo

s Ltd.
a

ty
Columbia
runswick
chewan
a Genome BC Proteomics Center
or

& Russia (60)

of Leuven

♦ **FRANCE** (10)
Atomic Energy & Alternative Energies Commission
CNRS Grenoble
École Polytechnique, CNRS
ENS Lyon
ESPCI ParisTech
French Institute of Petroleum
Lille University of Science & Technology
Materials, Microelectronics & Nanoscience Institute of Provence "IM2NP", CNRS
University of Nantes
University of Paris-Sud

♦ **GERMANY** (18)
Bielefeld University
Dresden University of Technology
Free University of Berlin
Fritz Haber Institute of the MPG
Helmholtz-Zentrum Berlin
Helmholtz-Zentrum Dresden-Rossendorf
Humboldt University of Berlin
IFW Dresden (Leibniz Institute)
Jacobs University
Leipzig University
Martin Luther University of Halle-Wittenberg
MPI for Chemical Physics of Solids
MPI of Colloids & Interfaces
Technical University of Berlin
University of Augsburg
University of Cologne
University of Freiburg
University of Stuttgart

♦ **GREECE** (1)
University of Crete

♦ **ITALY** (2)
Civic Museum of Natural History, Ferrara
CNR Institute SPIN

♦ **THE NETHERLANDS** (1)
Utrecht University

♦ **POLAND** (2)
Polish Academy of Sciences (Wrocław)
Wrocław University of Technology

♦ **PORTUGAL** (1)
Nuclear & Technological Institute, Sacavém

♦ **RUSSIA** (6)
A.F. Ioffe Physical Technical Institute, RAS
Lomonosov Moscow State University
Kazan State University
National University of Science & Technology "MISIS"
Russian Academy of Sciences (Moscow)
Institute of Metal Physics, RAS

♦ **SLOVAKIA** (2)
Slovak Technical University
University of St. Cyril & Methodius

♦ **SPAIN** (3)
Rovira i Virgili University
University of Barcelona
University of Santiago de Compostela

♦ **SWEDEN** (1)
University of Lund

♦ **SWITZERLAND** (2)
Swiss Federal Institute of Technology, Lausanne
Swiss Federal Institute of Technology, Zurich

♦ **UNITED KINGDOM** (6)
Bristol University
Cambridge University
Keele University
Oxford University
University of Edinburgh
Warwick University

♦ **UKRAINE** (2)
Institute of Organic Chemistry, NAS Ukraine
Taras Shevchenko University

Australia & Asia (38)

♦ **CHINA** (8)
Beijing Academy of Agriculture & Forestry Sciences
Hefei National Laboratory
Institute of Physics, CAS
Second Military Medical University
Tsinghua University
University of Science & Technology of China
Wuhan Institute of Physics & Mathematics, CAS
Xiamen University

♦ **INDIA** (1)
University of Calcutta

♦ **ISRAEL** (2)
Weizmann Institute of Science
Tel Aviv University

♦ **JAPAN** (15)
Central Research Institute of Electric Power Industry
Japan Atomic Energy Agency
Japan Petroleum Energy Center
Kanazawa University
Kyoto University
Mie University
Nagoya University
National Institute for Materials Science
Osaka City University
Osaka Prefecture University
Osaka University
RIKEN
Tokyo Institute of Technology
Tokyo University of Agriculture & Technology
University of Tokyo

♦ **NEW ZEALAND** (2)
Massey University
University of Auckland

♦ **SOUTH KOREA** (10)
Chung Ang University
Ewha Woman's University
Korea Advanced Institute of Science & Technology
Korea Basic Science Institute, Daegu Center
Kyung Hee University
Kyungpook National University
Pohang University of Science & Technology
Pukyong National University
Seoul National University
Yonsei University

tates (159)

GION (33)
s (CA)
ersity (UT)
of Technology
University
Research Institutes (CA)
National Lab (CA)
National Lab (CA)
l Laboratory (NM)
Energy Laboratory (CO)
atories (CO)

ence University
sity
ational Laboratory (WA)
oratories (NM)
versity (CA)
erator Laboratory (CA)
nstitute of Science (WA)
(CA)
Anchorage
nia, Berkeley
nia, Davis
nia, Irvine
nia, Los Angeles
nia, Riverside
nia, San Diego
nia, Santa Barbara
lo, Denver
lo School of Medicine

rn California

University of Washington
Western Washington University

♦ **MIDWESTERN REGION** (28)
Air Force Research Laboratory (OH)
Ames Laboratory (IA)
Argonne National Laboratory (IL)
Iowa State University
Kent State University (OH)
Lawrence University (WI)
Mayo Clinic (MN)
Missouri University of Science & Technology
Northwestern University (IL)
Oberlin College (OH)
Ohio State University
Ohio State University Medical Center
Purdue University (IN)
Roosevelt University (IL)
University of Akron (OH)
University of Chicago (IL)
University of Illinois at Chicago
University of Illinois College of Medicine at Chicago
University of Michigan
University of Minnesota
University of Missouri, St. Louis
University of Nebraska, Omaha
University of North Dakota
University of Notre Dame (IN)
University of Wisconsin, Madison
University of Wisconsin School of Medicine
Wayne State University (MI)
Washington University in St. Louis (MO)

♦ **SOUTHERN REGION** (50)
All Things Bugs (FL)
Barry University (FL)
Christopher Newport University (VA)
ConocoPhillips (TX)
Doty Scientific, Inc. (SC)
Duke University (NC)
East Carolina University (NC)
Emory University (GA)
Florida A&M University
Florida Atlantic University
Florida State University
Georgia Institute of Technology
Georgia State University
Halliburton Energy Services (OK)
Louisiana State University
Mayo Clinic in Jacksonville (FL)
Medical University of South Carolina
Morehouse College (GA)
Nalco Energy Services (TX)
North Carolina State University
Oak Ridge National Laboratory (TN)
Old Dominion University (VA)
Rice University (TX)
RTI International (NC)
Sanford-Burnham Medical Research Institute (FL)
Scripps Research Institute (FL)
Shell Global Solutions Inc. (TX)
Smithsonian Marine Station (FL)
Texas A&M University
University of Central Florida
University of Florida
University of Houston (TX)
University of Kentucky
University of Mississippi
University of North Carolina, Chapel Hill
University of North Carolina, Wilmington
University of Oklahoma
University of South Alabama
University of South Carolina
University of South Florida
University of Tennessee, Knoxville
University of Texas at Austin
University of Texas Health Science Center at Tyler
University of Texas Medical Branch
University of Texas Southwestern Medical Center
USDA Center for Medical, Agricultural, and Veterinary Entomology (FL)
Valdosta State University (GA)
Vanderbilt University (TN)
Virginia Tech
Wichita State University

♦ **NORTHEASTERN REGION** (46)
BioTherapeutics R&D (MA)
Boston College (MA)
Boston University School of Medicine (MA)
Brandeis University (MA)
Brookhaven National Laboratory (NY)
Brown University (RI)
Brucker Biospin (MA)
Carmagen Engineering, Inc. (NJ)
Carnegie Institution for Science (DC)
City College of New York
Clark University (MA)
Columbia University (NY)
Cornell University (NY)
Dana-Farber Cancer Institute (MA)
Dartmouth College (NH)
Dartmouth Medical School (NH)
Georgetown University (DC)
Hamilton College (NY)
Harvard University (MA)
Harvard Medical School (MA)
IBM TJ Watson Research Center (NY)
Johns Hopkins University (MD)
Massachusetts Institute of Technology
National Institute of Standards & Technology (MD)
National Institutes of Health (MD)
New York University
Northeastern University (MA)
Penn State University
Queens College of CUNY (NY)
Primus Green Energy (NJ)
Princeton University (NJ)
Rensselaer Polytechnic Institute (NY)
Roberts Consulting Group (MA)
Rutgers University (NJ)
Smith College (MA)
Stony Brook University (NY)
Stroud Water Research Center (PA)
Tufts University (MA)
University at Albany, SUNY (NY)
University of Delaware
University of Massachusetts, Amherst
University of Pennsylvania
University of Pittsburgh
University of Vermont
Woods Hole Oceanographic Institute (MA)
Yale University (CT)

♦ **PUERTO RICO** (2)
University of Puerto Rico, Mayaguez
University of Puerto Rico, San Juan

Topological Matter

Typically the energy of an electron behaves in much the same way as a ball flying through the air: their energy of motion increases as the square of their speed. Some high-energy electrons, like those in Large Hadron Collider, behave differently and their energy increases linearly with the speed, a behavior that results directly from Einstein's special relativity. Such electrons are referred to as "Dirac" electrons. The Dirac electrons turn out to be essential to the long-standing pursuit of the quantum computer. The manuscript by Lawson, Hor and Li presents the first observation of quantum oscillations in the topological superconductor, copper doped bismuth selenide. The results demonstrate that the electrons in the material are indeed Dirac electrons, even though the electrons move much slower than those in LHC. The Dirac electrons have the ability to clump together into a new kind of qubit that changes the properties of the material in a way that's detectable to an observer, but not to the qubits. So the qubits can carry on calculating without knowing they're being watched. Their work suggests that copper doped bismuth selenide is a promising material for quantum computation.

• Published in *Phys. Rev. Lett.*, **109**, 226406 (2012)

Dirac Electrons in Topological Insulator Candidates

B.J. Lawson, G. Li, T. Asaba, F. Yu and L. Li (Univ. Michigan); **Y.S. Hor** (Missouri S.T.)

Introduction

The discovery of topological insulators and possible topological superconductors opens a new area of study and brings hope to more exciting applications such as topological quantum computation.[1] In Cu doped Bi_2Se_3 single crystals, a superconducting ground state was observed at T < 3.8 K. However, the magnetic and electronic structure is not well understood in the normal state of Cu doped Bi_2Se_3. The material is diamagnetic even in the normal state. The estimate of effective mass in the ARPES results well above T_c is very different from that of the heat.[2, 3] More importantly, the exact Fermi surface topology was not clearly determined in the ground state since the quantum oscillation of the bulk state has not been observed. Our solution is to study the magnetic and electronic structure using high-resolution torque magnetometry.[4, 5, 6] Recently, we were able to resolve the quantum oscillations[7] of Cu doped Bi_2Se_3, providing a sensitive probe to the Fermi surface of the topological superconductor candidate Cu doped Bi_2Se_3.

Experimental

High-resolution torque magnetometry was used to measure the magnetic moment of the samples. Torque is measured as the change of the capacitance between the metal cantilever and a nearby metal plate.

Conclusions

Our quantum oscillations results confirm the 3D Fermi surface in Cu-doped Bi_2Se_3. The doping of Cu changes the carrier density, but the Fermi velocity stays the same. Our result suggests the conduction electrons are in the Dirac-like band in Cu-doped Bi_2Se_3.

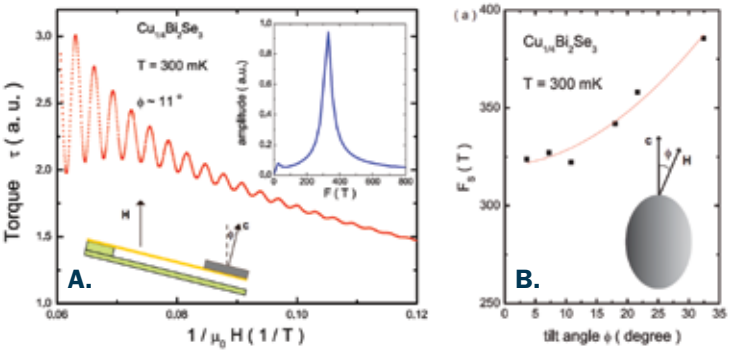


FIGURE 1. de Haas-van Alphen effect of topological superconductor Cu doped Bi_2Se_3. **A.** Quantum oscillation pattern observed in the torque magnetometry. The lower left panel shows the sketch of the measurement set-up. **B.** Angular dependence of the oscillating frequency. The lower insert shows a sketch of the estimated Fermi surface.

Acknowledgements

We thank the support from the University of Michigan.

REFERENCES

1. Y.S. Hor, *et al., PRL*, **104**, 057001 (2010).
2. L. A. Wray, *et al., Nature Physics*, 6, 855 (2010).
3.M. Kriener, *et al., PRL*, **106**, 127004 (2011).
4. Lu Li, *et al., Nature Physics*, **7**, 762-766 (2011).
5. Lu Li, *et al., Nature Physics*, **7**, 762-766 (2011).
6. Lu Li, et al., Science, 321, 547-550 (2008).
7. B. J. Lawson, Y.S. Hor, Lu Li, PRL 109, 226406 (2012).

Magnet Technology

After 25 years of Bi-2212 coil technology with limited current densities, recent improvements in conductor processing via overpressure heat treatments and improvements in insulation now make it possible to more than double the current density. This makes compact high-field coils possible with Bi-2212 and provides a welcome alternative to coated conductor technology for specific applications as each conductor type has different characteristic features.

High Field Magnets with $Bi_2Sr_2CaCu_2O_{8+x}$ /Ag Alloy Round Wire

U.P. Trociewitz, M. Dalban-Canassy, P. Chen, N. Craig, E.E. Hellstrom, J. Jiang, M. Matras, Y. Viouchkov and D.C. Larbalestier (NHMFL)

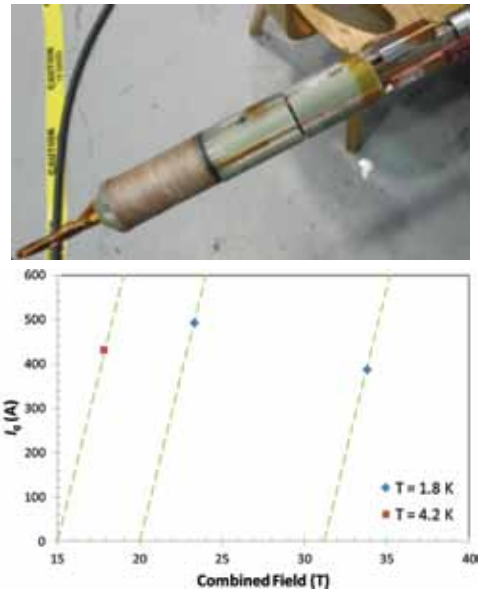


FIGURE 1. (TOP) Bi-2212 layer wound coil mounted on the probe. The coil specifications are: 71.2 mm long, 14.3 mm ID, 36 mm OD, ~30 m total conductor length.
FIGURE 2. (BOTTOM) Quench current vs. field relationship of coil for different bath temperatures.

Introduction

$Bi_2Sr_2CaCu_2O_{8+x}$ (Bi-2212) is the only High Temperature Superconductor (HTS) available in round wire form. However, relatively low critical current densities and thick and chemically incompatible insulations[1] have long been the limiting factors for high field magnet applications. Recent progresses in the understanding of Bi-2212 wire processing have led to more than double their critical current density[2] (more than 600 A/mm^2 at 20 T), by using an overpressure heat treatment that densifies the wire during the heat treatment processing. In addition, a newly developed commercial temperature tolerant 15 µm thick TiO_2 based insulation has become available that is 10 times thinner than the current alumino-silicate or silica braided insulations provided by the conductor manufacturers, which significantly enhances the winding current density in coils.

Experimental

A small test coil was wound using Bi-2212 round wire insulated with the TiO_2 based insulation. The coil was heat treated in synthetic air at a total pressure of 10 atm. After the heat treatment the coil was epoxy impregnated and instrumented for low temperature in-field measurements. The coil was tested in-house in the 31.2 T resistive magnet.

Results & Discussion

The coil generated an additional magnetic field of 2.6 T for a total of 33.8 T at a helium bath temperature of 1.8 K, corresponding to a winding current density of 187 A/mm^2 at quench *i.e.* a conductor engineering current density of about 225 A/mm^2. Though the coil was safely quenched multiple times for different ramp rates, the coil was limited by the performance of the terminals. Due to space restrictions of the currently solely available over pressure furnace, the coil was heat treated with the terminals reaching into the non-homogeneous zone of the furnace. The terminal sections were thus heat treated at lower temperatures than the coil, yielding their lower transport performance. This was corroborated by the finding that short samples cut as witness samples from the ends of the coil, *i.e.* in the terminal region, performed significantly below expectations. Nevertheless, the transport properties of the coil showed a more than two-fold increase of the winding current density over previous coils.

Conclusions

The performance of this coil clearly demonstrates that Bi-2212 round wire is becoming a viable conductor for high magnetic field applications whose limits have yet to be explored in coils. These results open up a whole area of potential applications ranging from NMR to High Energy Physics, where a round electromagnetically isotropic wire that can be easily cabled is highly preferable over the highly aspected tape conductors.

Acknowledgements

This work was supported by the NSF under DMR award 0654118.

REFERENCES

1. M. Dalban-Canassy, *et al., Supercond. Sci. and Technol.*, **25**, no. 11, p. 115015, Nov. 2012.
2. J. Jiang, *et al., Supercond. Sci. Technol.*, **24**, no. 8, p. 082001, Aug. 2011.

Magnet Technology

Magnets using HTS conductors will attain higher products of field and field gradient than ever seen in LTS magnets. Consequently, bubbles of He gas will have a downward magnetic force and will no longer rise and will become trapped in the bore of the magnet. This might have a very negative impact on the cooling of the magnet. The 32 T magnet at the MagLab will include plates to enhance the radial thermal conductivity of the coil to prevent the helium bubble from being too warm, thereby allowing the coil to remain superconducting and serviceable. Consequently this work is essential to enabling the 32 T magnet to become operational. We expect most subsequent HTS magnets built worldwide will benefit from this development.

• Published in *IEEE Trans. Appl. Supercond.*, **23** (3), 1051-8223 (2013)

Thermal Conductivity Test of YBCO Coated-Conductor Tape Stacks Interleaved with Insulated Stainless Steel Tapes

H. Bai, W.D. Markiewicz, J. Lu and H.W. Weijers (FSU, MST)

Introduction

A 32 Tesla, all-superconducting user magnet, which consists of two HTS YBCO inner coils producing a field of 17 T in an LTS Nb_3Sn and NbTi outer magnet producing a background field of 15 T, is being developed at the National High Magnetic Field Laboratory. The YBCO coils are pancake-wound as opposed to layer-wound for a variety of reasons including available conductor piece length.[1] The degradation of epoxy-impregnated YBCO coils resulted in selection of the dry-wind approach for the 32 T YBCO coils to avoid de-lamination of the tape.[2] The inter-turn insulation uses a sol-gel alumina-insulated co-wound stainless steel tape. The YBCO inner coils are to be cooled at 4.2 K liquid helium in normal operation. The heat losses in the coils, such as Joule-heating in the joints, the heat loss from the current leads and the ramping loss (AC loss) during ramping up/down the magnet, have to be transferred away to the external surfaces of the coil and then to LHe. Such internal cooling depends on the effective heat conduction of the coils. There are hundreds of contact interfaces between the YBCO conductors and stainless steel tapes in the radial direction of the coil, and the cross section of YBCO tapes are not strictly rectangular, which makes a prediction of the thermal conductivity generally impossible because the thermal contact resistances may play an important role.



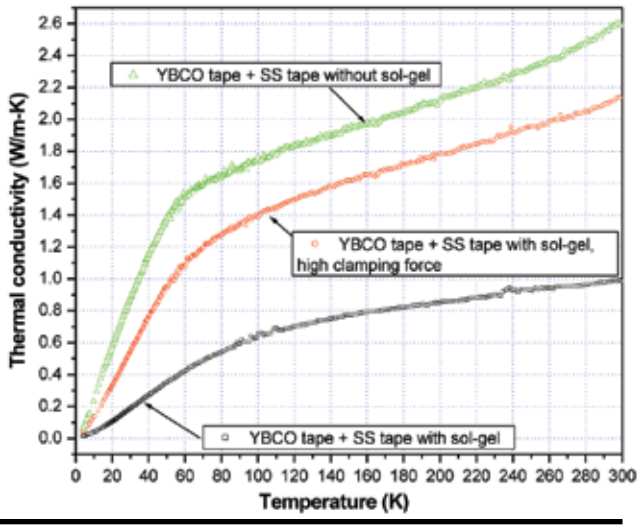


FIGURE 1. (LEFT) Assembly of the sample with two YBCO stacks installed symmetrically in the Thermal Transport Sample Puck.
FIGURE 2. (RIGHT) Thermal conductivity for three different cases: 1, YBCO tape and sol-gel coated SS tape under moderate clamping force. 2, YBCO tape and sol-gel coated SS tape under high clamping force; 3, YBCO tape and SS tape without sol-gel coating under moderate clamping force.

Experimental, Results & Discussion

The thermal conductivity was measured in the Physical Property Measurement System (PPMS) of Quantum Design. The test sample consists of two stacks and each stack has 15 YBCO tape pieces and 15 stainless steel tape pieces stacked together. Two identical stacks were made for the test and they are installed and clamped in a copper frame by two bolts at both ends, shown in **Figure 1**. Tests were done in a continuous measurement mode and the measurements were taken

automatically as the temperature ramped up from 4.2 K to 80 K or 300 K. **Figure 2** shows the results.

The estimated radial conductivity turns out to be about 1.2 W/m·K at 4.2 K without including the thermal contact resistance. This is almost two orders of magnitudes higher than the experimental value. It is mainly because the thermal contact resistance plays a dominant role in the heat conduction. In the YBCO tape fabrication process, the stabilizing copper is electroplated in the final step. The final conductor thickness is determined by the copper thickness and this thickness is found to vary on the conductor. The cross section of YBCO tapes are of a dog bone shape. This causes gaps between turns that result in the very poor thermal contacts between the turns. The turn insulation is made by insulated co-wound stainless steel tape between bare conductors. This insulation decreases the radial thermal conductivity further.

REFERENCES

1. W.D. Markiewicz, *et al., IEEE Trans. Appl. Supercond.*, **22** (3), 1051-8223(2012).
2. T. Takematsu, *et al., Physica C* **470**, 674-677(2010).

Magnet Technology

HTS cables that carry current in the 5-20 kA range in high magnetic fields are needed in the next generation of large-bore superconducting and hybrid magnets. At this time, there are at best three viable concepts but almost no actual cable samples or high-field data. This work represents the promising first steps in the development of such cables.

Comprehensive Analysis of Binary Current Leads for the NHMFL Series Connected Hybrid Magnet in the Course of their Development

A.V. Gavrilin, W.S. Marshall, P.D. Noyes, S. Napier and M.D. Bird (NHMFL)

Introduction

The NHMFL MS&T Division is finalizing the design of binary 20-kA class current leads (CLs) to be used in the Series Connected Hybrid Magnet (SCH) (**Figure 1**). The lead is to consist of a resistive nitrogen-vapor-cooled section of original design (jellyroll type) and a conduction-cooled HTS section connected together by a liquid nitrogen intercept. The HTS part is to be made up of REBCO tape stacks fitted to a stainless steel pipe going to work as a support structure and a protecting shunt resistance in the event of quench.

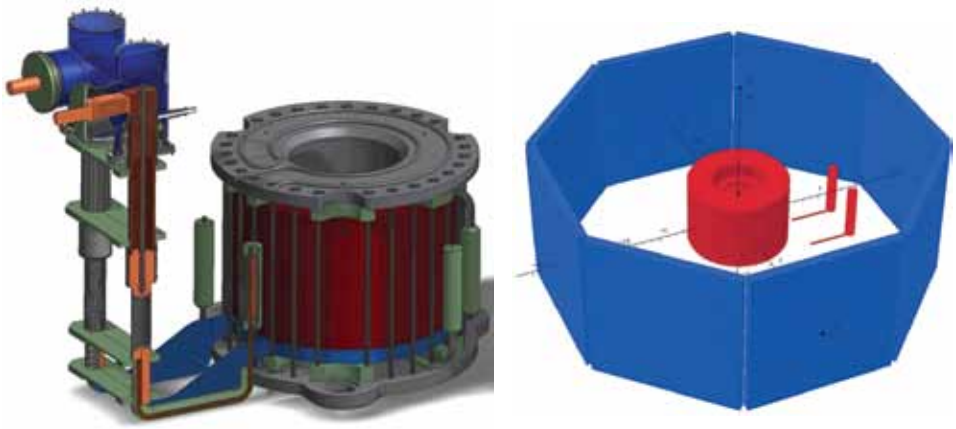


FIGURE 1. (LEFT) Isometric view and cross-section of the SCH binary current leads located not so far from the magnet.
FIGURE 2. (RIGHT) FE model of SCH magnet system with components to be included in the analysis of magnetic field in the CLs' HTS section area: SCH coils, iron shield plates, multi-stack HTS sections of the CL pair, and bus-bars. OPERA by Vector Fields is employed.

Analyses to be done in the course of the current leads development

As opposed to multi-kA binary CLs developed by others, the NHMFL CLs, being installed not so far from the magnet, are supposed to operate in a rather high fringe magnetic field that is a challenging option never tried before. Particularly, this fact invited a comprehensive FEA of the superposition of magnetic field from the SCH magnet coils and the CLs' self-field in the presence of a massive magnetic iron shield with a view to calculating precisely the critical current reduction of the REBCO tapes so as to find the appropriate number of them (based upon in-house measurements of the critical current depending on the magnetic field and the field vector angular orientation). In addition, the attractive forces (first and foremost acting upon the HTS section) turn out to be rather high and should be reliably computed to be supported. OPERA by Vector Fields was used to fulfill the tasks (**Figure 2**). A FEA by ANSYS was employed to simulate the current transition from the resistive section to the HTS one through the nitrogen intercept.

Also, detailed thermal analyses, both steady-state and transient ones, of the entire CLs, including the resistive and HTS parts, at the rated and idle currents were performed to optimize the CLs thermally and minimize the heat input to the nitrogen intercept and at the cold end of HTS section as well. The transient analysis, which typically is sophisticated and not customary, was done because the NHMFL SCH major operation scenario is a so-called cyclic operation, when the magnet is ramped up to the field and then ramped down to zero on a periodical basis. The thermal analysis is followed by a thermal stress analysis to complete the picture.

Such a complex, comprehensive analysis is unprecedented and assumed to enable us to succeed with the CLs development.

Acknowledgement

The work is supported by the National Science Foundation under Grant DMR-060342.

REFERENCES

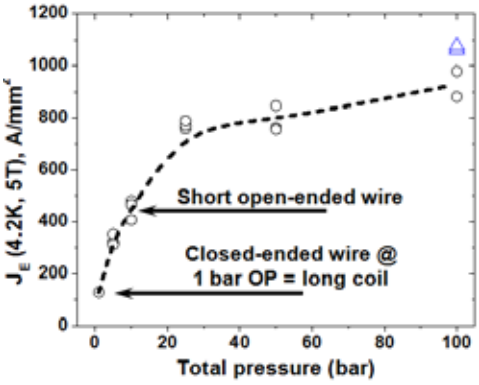
1. Marshall, W.S., *et al.*, Presented at the Cryogenics Engineering Conference, 2013, Anchorage, AK

Applied Superconductivity

This work, done late in 2012, has made Bi-2212 round wire a new and viable magnet technology. It has generated a lot of interest and new funding, and has been a wonderful R&D effort targeted at understanding a very complex material that has been not well understood for over 20 years. It will be a very good basis for high field NMR magnet technology.

Overpressure Processing as the Route to Dense, High Critical Current Density, Coil-Length Bi-2212 Round Wires

J. Jiang, M.R. Matras, N.C. Craig, F. Kametani, P.J. Lee, U.P. Trociewitz, E.E. Hellstrom and D.C. Larbalestier
(Applied Superconductivity Center, NHMFL, FSU)



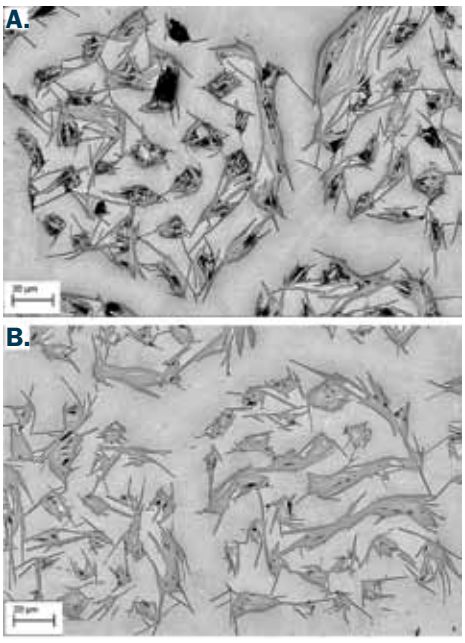


FIGURE 1. (TOP) J_E (4.2K, 5T) as a function of total pressure for overpressure processed wires. **FIGURE 2. (BOTTOM)** SEM images of Bi-2212 wires processed under **A.** 5 bar with I_c (4.2K, 5T) = 177 A, **B.** 100 bar with I_c (4.2K,5T) = 463 A.

Introduction

$Bi_2Sr_2CaCu_2O_x$ (Bi-2212) is the only cuprate superconductor that can be made in round wire with high critical current density (J_c), but its magnet use is restricted because gas bubbles form during the reaction, causing wire expansion, leakage and filament dedensification that greatly reduces J_c in coil-length wires compared to short samples with open ends. Here we report that applying total pressures of 10 to 100 bars with a constant oxygen partial pressure of 1 bar during the heat treatment greatly controls the dedensification, eliminates leakage, and hugely raises J_c.

Experimental

Bi-2212 wires with 37 x 18 filaments, 0.8 mm in diameter received a standard heat treatment schedule[1] under pressures ranging from 5 to 100 bars and a constant oxygen partial pressure of 1 bar. The diameter, microstructure and critical current of the fully-processed wires were measured.

Results

We found that 5 bar overpressure (OP) processing limits Bi-2212 wire expansion and prevents leakage, while pressures > 10 bar can densify the wire. As shown in **Figure 1**, the engineering critical current density, J_E (4.2K, 5T), for wires processed at 25 and 50 bar was nearly doubled, compared to short samples with open ends, and increased ~ 7 times compared to closed-ended wire processed under 1 bar. A record J_E (4.2K) of 1064 A/mm^2 at 5 T was achieved in wire processed under 100 bars. **Figure 2** shows that the 100 bar sample has much denser filaments and smaller impurity phases than the 5 bar sample.

Conclusions

Our results provide the essential proof of principle that round-wire Bi-2212 conductors are now ready for serious high-field magnet applications since the densification effect of OP processing is the same for short and long wires with closed ends.

Acknowledgements

The work at the NHMFL was supported by an ARRA grant of the US Department of Energy Office of High Energy Physics and by the NHMFL which is supported by the National Science Foundation under NSF/DMR-0654118 and by the State of Florida.

REFERENCES

1. Jiang, J, *et al., Supercond. Sci. Technol.*, **24**, 082001 (2011).
2. Larbalestier, D.C., *et al.*, arXiv:1305.1269 [cond-mat.supr-con]

Applied Superconductivity

The ability to transmit high current density J_c in polycrystalline forms of the high temperature superconductors (*e.g.* cuprates or Fe-based superconductors) is essential to any magnet applications. Thus, the properties of grain boundaries, especially randomly oriented ones, are of great interest. Here magneto-optical imaging shows that supercurrent flows uniformly over the full size of cm-sized untextured polycrystalline bulk samples of $(Ba_{1-x}K_x)Fe_2As_2$ that attain $J_c > 10^5$ A/cm^2. Because these materials also have upper critical fields exceeding 80 T and almost no anisotropy, they are potentially very useful as a new high field superconductor.

Magneto-Optical and Electromagnetic Study of Intergrain Critical Current in Fine-Grain $(Ba_{0.6}K_{0.4})Fe_2As_2$ Wire and Bulks

A.A. Polyanskii, J.D. Weiss, C. Tarantini, J. Jiang, F. Kametani, D.C. Larbalestier, and E.E. Hellstrom
(Applied Superconductivity Center, NHMFL, FSU)

Introduction

Magneto-Optical Imaging (MOI) together, supplemented by other electromagnetic techniques, SEM and TEM, were successfully applied to new forms of Fe-based superconductors, where the balance of pinning and connectivity between grains (weak links) is still under debate. Here we report that under certain synthesized conditions untextured polycrystalline $(Ba_{0.6}K_{0.4})Fe_2As_2$ bulks and round wires with high grain boundary density have transport critical current well over 10^5 Acm^{-2} (SF, 4.2 K), more than 10 times higher than critical current density of any other ferropnictide wire. The high global critical current was well supported by MOI.

Experimental

Magneto-Optical Technique, Electromagnetic Measurements, as well SEM and TEM were used for the characterization of physical properties of bulk and wire materials. The very fine grains with size ~200 nm, after the ball-milling, were synthesized under high pressure using chemical reaction at temperature well below the melting temperature of secondary phases.

Results & Discussion

Figure 1 demonstrates uniform high density global critical current in a rectangular piece of K-doped Ba-122 bulk material with magnetic fields perpendicular to plain of the sample (thickness = 0.7 mm).

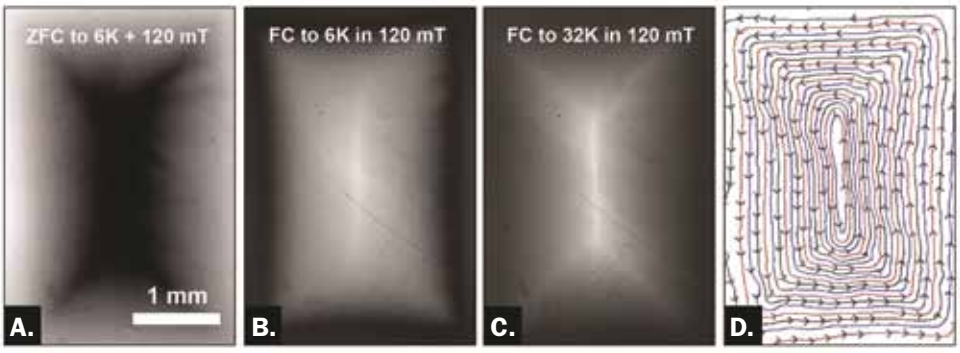


FIGURE 1.

(**Figure 1A**) magneto-optical image of partial flux penetration after zero-field-cooling (ZFC) the sample to 6 K and applying a magnetic field of 120 mT. (**Figure 1B**) Magneto-optical image of trapped magnetic flux in a sample field-cooled (FC) to 6 K in an external magnetic field of 120 mT. (**Figure 1C**) Magneto-optical image of trapped magnetic flux in a sample FC to 32 K in an external magnetic field of 120 mT. Current stream lines (**Figure 1D**) calculated for (**c**) illustrates that even at temperature near T_c global current circulates inside the bulk reasonably uniform.

Like this procedure, described in experimental section, minimizes the formation of current-blocking FeAs secondary phases and do not wet GBs. TEM observation confirms that the better part of GBs are clean and well-connected and as result, they do not block significantly critical current in bulk and wire $(Ba_{0.6}K_{0.4})Fe_2As_2$.

Conclusions

Our research showed that high global critical current density in the pnictide compound $(Ba_{0.6}K_{0.4})Fe_2As_2$ with small and randomly oriented grains is possible and that there is much less sensitivity to grain misorientation than is seen in the cuprates. The J_c values are close to those needed for practical applications.

Acknowledgements

This work is supported by NSF DMR-1006584, by the National High Magnetic Field Laboratory which is supported by the National Science Foundation under NSF/DMR-0084173 and by the State of Florida.

REFERENCES

1. J.D. Weiss, *et al., Nature Materials* **11**, 682-685 (2012).

Chemistry

This report represents a hot topic in materials science: novel blue dyes, superior to the traditional ones. Their optical properties need to be correlated with the magnetic ones.

HFEPR of Magnetic Materials with Unusual Optical Properties: $YIn_{1-x}Fe_xO_3$

P. Jiang and M.A. Subramanian (Oregon State U., Chemistry); **J. Telser** (Roosevelt U., Chemistry); **A. Ozarowski and J. Krzystek** (NHMFL)

Introduction

A new class of magnetic materials has recently been prepared by Subramanian and co-workers.[1] These materials are based on $YInO_3$, in which the In^{3+} ions are replaced by M^{3+} to give $[YIn_{1-x}M_xO_3]$, where $0 \le x \le 1$, and $M^{3+} = Mn^{3+}$ ($3d^4$, $S = 2$)[2], Fe^{3+} ($3d^5$, $S = 5/2$)[3]. $YInO_3$ is white, as expected for a closed shell system (Y^{3+}, $[Kr]4d^0$; In^{3+}, $[Kr]4d^{10}$, both $S = 0$). The doped systems exhibit intense colors: blue for Mn and yellow to orange to red to red-brown for Fe, as a function of x. These materials already have applications as pigments and as IR-reflective screens. Their structure is shown in **Figure 1**. The relation between their optical and magnetic properties is thus of great interest.

Experimental

The EMR Facility and its 15/17-T superconducting magnet was used to record HFEPR spectra of powdered $YIn_{1-x}Fe_xO_3$, with $x = 0.1 - 0.5$.

Results & Discussion

We have often had difficulty in observing satisfying HFEPR spectra from complexes of Fe^{3+} (and of Fe^{2+}), but not so here. High-quality spectra, in terms of S/N and linewidth, were recorded for the whole range of Fe concentrations, and in a wide temperature range from liquid helium to room temperature. Higher dilution reduced the S/N and lower dilution led to excessive line broadening due to spin-spin magnetic interactions. **Figure 2** shows an HFEPR spectrum of Fe^{3+} at 203.2 GHz and 10 K. The frequency dependence of HFEPR resonances has been mapped (not shown) and computer fitting of this pattern allowed determination of the $S = 5/2$ spin Hamiltonian parameters for the Fe^{3+} sites. For example, the sample with $x = 0.1$ yields: $D = -1.095(2)$ cm^{-1}, $E = 0.003(4)$ cm^{-1}, $g_\perp = 2.007(1)$, $g_{||} = 2.004(3)$. The current study complements the relatively few ferric systems investigated by HFEPR, and is the first representative of trigonal bipyramidal geometry.

Conclusions

The $[YIn_{1-x}Fe_xO_3]$ pigments have shown great promise for HFEPR investigations. Future work will involve the relation of the parameters derived from HFEPR with the optical properties of these materials and with other Fe^{3+} systems.

Acknowledgements

The work at Oregon State University is supported by NSF (DMR-0804167).

REFERENCES

1. Smith, A.E., *et al., J. Am. Chem. Soc.*, **131**, 17084-17086 (2009).
2. Mizoguchi, H., *et al., Inorg. Chem.*, **50**, 10-12 (2011).
3. Jiang, P., *et al., Inorg. Chem.*, **50**, 5858-5860 (2011).

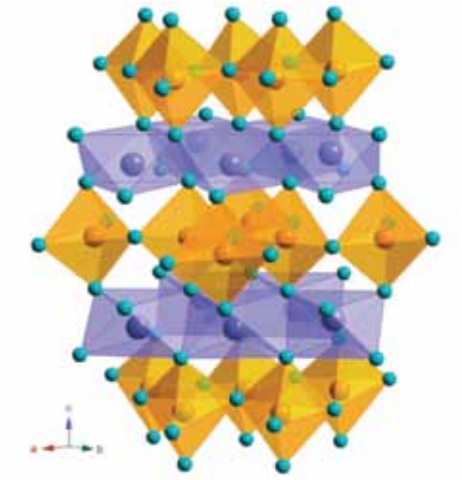


FIGURE 1. Structure of $YIn_{1-x}Fe_xO_3$ (Y, purple; In and Fe, orange; O, turquoise spheres).

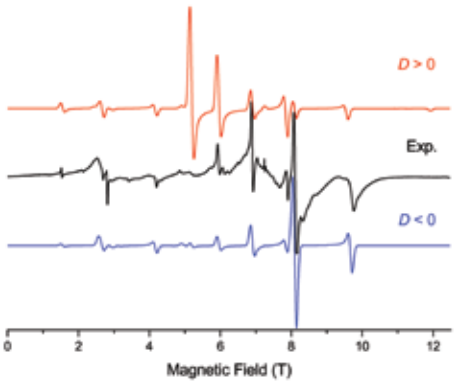


FIGURE 2. HFEPR spectrum of $YIn_{0.9}$ $Fe_{0.1}O_3$ recorded at 203.2 GHz and 10 K (black trace) together with powder pattern simulations using spin Hamiltonian parameters as in text. Red trace: positive D; blue trace: negative D.

Chemistry

This report deals with magnetic interactions within a di-metallic complex. Understanding such interactions in simple systems is crucial for modeling properties of single-molecule magnets.

• Published in *Dalton Trans. Chem.*, **42**, 207-216 (2013)

EPR Studies of a Mn(III)–Cu(II) Dimer Containing a Jahn–Teller Compressed Mn Ion

N. Berg and L.F. Jones (National U. of Ireland, Galway, Chemistry); **T.N. Hooper and E.K. Brechin** (U. of Edinburgh, Chemistry); **J. Liu** (NHMFL and UF Physics); **C.C. Beedle** (NHMFL); **S.K. Singh and G. Rajaraman** (Indian Institute of Technology, Mumbai, India); **S. Piligkos** (U. of Copenhagen, Denmark); **S. Hill** (NHMFL and FSU Physics)

Introduction

The heterobimetallic complex [Cu(II)Mn(III)(L)$_2$(py)$_4$](ClO$_4$)·EtOH (1), where L is 2,2´-biphenol, is a rare example of a dimeric [Cu(II)Mn(III)] compound, and the first example to exhibit a Jahn-Teller compressed Mn(III) center[1] (**Figure 1A**). Analysis of high-field and high-frequency EPR, magnetic susceptibility and DFT studies reveal that this interesting complex exhibits antiferromagnetic interactions between the Cu and Mn centers (J = –33.4 cm^{-1}) resulting in an S = 3/2 ground state.

Experimental

Powder EPR data were collected in a transmission-type spectrometer employing a 17 T superconducting magnet. A phase-locked oscillator, in conjunction with a series of multipliers and amplifiers, was employed as a microwave source covering the frequency range from 50 to 600 GHz.

Results & Discussion

At frequencies below 200 GHz (**Figure1B**), the spectra exhibit three strong resonance branches that pass through the origin, which represent the x, y and z-transitions within the ground-state Kramers doublet (open red, blue and black circles, respectively). Above 200 GHz, additional resonance branches are evident at low fields (solid black squares and circles) (**Figure 1B**). These resonances meet at a finite frequency at zero field, which corresponds to the zero-field splitting between the two lowest Kramers doublets (381±5 GHz). The frequency-dependent EPR data were simulated employing the spin Hamiltonian (1) with S = 3/2, yielding the parameters: D_S = +6.27 cm^{-1}, E_S = ±0.57 cm^{-1}, $g_{S,x} = g_{S,y}$ = 1.97 and $g_{S,z}$ = 1.98.

$$\hat{H}_s = \mu_B \vec{B} \cdot \vec{g}_s \cdot \hat{S} + D_s \hat{S}_z^2 + E_s(\hat{S}_x^2 - \hat{S}_y^2)$$

In these simulations, the magnitude of D_s (axial cluster anisotropy) is well constrained by the zero-field intercept, while the rhombic term, E_s, is constrained by the sizable splitting exhibited by the x (red circles) and y (blue circles) intra-Kramers branches. Projection of the single-ion $D_{Mn(III)}$ value onto the S = 3/2 ground state of the coupled dimer leads to the prediction $D_{Mn(III)} = 0.71 D_S$ = +4.45 cm^{-1}, which agrees with magnetic measurements.[1]

Conclusions

Spectroscopic studies have been carried out on an interesting antiferromagnetically coupled Cu-Mn dimer that reveals an S = 3/2 ground state experiencing significant easy-plane type magnetic anisotropy, which is consistent with a Jahn-Teller compressed Mn(III) ion.

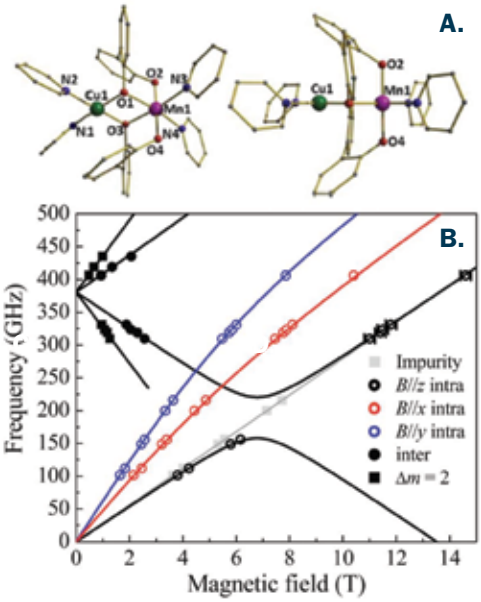


FIGURE 1. A. Ortep drawings of complex 1. **B.** Frequency versus field powder EPR data for 1 showing intra- (open circles) and inter-Kramers transitions (solid circles); the solid curves represent simulations.

Acknowledgements

Funding: LFJ – NUI Galway Millennium Fund and IRCSET; EKB – Leverhulme Trust and EPSRC; SH – NSF (CHE0924374); NHMFL – NSF DMR-0654118 and the State of Florida; SP – Danish Natural Science Research Council and Sapere Aude Fellow 10081659; GR – Govt. of India SR/S1/IC-41/2010; CB – Shuler fellowship.

REFERENCES

1. Berg, N., *et al., Dalton Transactions*, **42**, 207-216 (2013).

Chemistry

This report answers some basic questions in coordination chemistry of nickel (and other metal ions). It was published in the Journal of the American Chemical Society.

• Published in *JACS*, **135** (8), 3017-3026 (2013)

Giant Ising-type Magnetic Anisotropy in Trigonal Bipyramidal Ni(II) Complexes

L. Batchelor and T. Mallah (U. Paris Sud, France); **J. Liu** (UF Physics, NHMFL); **R. Ruamps, R. Maurice, M. Boggio-Pasqua and N. Guihery** (U. de Toulouse, France); **A.-L. Barra** (LNCMI, Grenoble, France); **E.-E. Bendeif, S. Pillet** (U. de Lorraine, France); **S. Hill** (NHMFL and FSU Physics)

Introduction

High-field, high-frequency electron paramagnetic resonance measurements performed on a single crystal of [Ni(Me$_6$tren)Cl](ClO$_4$) (**1**) reveal a giant uniaxial magnetic anisotropy with an experimental D_{exp} value [zero-field splitting (zfs) between the $M_S = \pm1$ and $M_S = 0$ components of the ground spin state S = 1] estimated to be between -120 cm^{-1} and -180 cm^{-1}.[1] Theoretical studies show that, for an ideally trigonal Ni(II) complex, the orbital degeneracy leads to a first order spin-orbit coupling that results in a splitting of the $M_S = \pm1$ and $M_S = 0$ components of *ca.* -600 cm^{-1}. In spite of the Jahn-Teller (JT) distortion that removes the ground term degeneracy and reduces the effects of the first order spin-orbit interaction, the D value remains very large. A good agreement between theoretical and experimental results (theoretical D_{th} between -100 cm^{-1} and -200 cm^{-1}) is obtained.[1]

Experimental

Angle-dependent, single-crystal high-field EPR measurements were carried out on **1** in a 31 T, wide bore (50 mm) resistive magnet at the DC field facility in Tallahassee. A Millimeter Vector Network Analyzer and several different multipliers were used as a microwave source and detector.

Results & Discussion

The extreme zfs of this compound precludes detection of the usual $M_S = \pm1$ to $M_S = 0$ transitions that enable a straightforward and precise evaluation of D_{exp}. However, by rotating the applied magnetic field into the hard plane ($\perp$ to easy-axis), one can observe nominally forbidden transitions within the $M_S = \pm1$ doublet, as seen in **Figure 1**. The JT distortion breaks the trigonal symmetry of **1**, giving rise to a rhombic anisotropy, E, as seen from the clear zero-field intercept (= 2E) of the data in the figure. Although the local trigonal symmetry is broken, the average crystallographic symmetry remains trigonal, i.e., the JT distortion gives rise to three differently oriented molecules – hence the observation of more than one EPR signal (A and B resonances). Fits to the two resonance branches enable an estimate of D_{exp}.

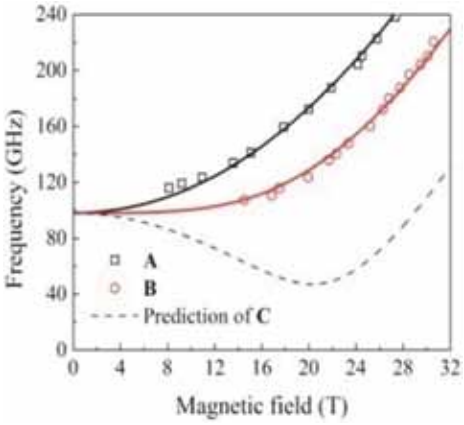


FIGURE 1. EPR peak positions observed with the field aligned in the hard plane of the A (black squares) and B (red circles) molecules. The solid lines are fits to the data; the dashed line represents the predicted positions of the EPR transitions associated with the C molecules.

Conclusions

Theory combined with EPR results and structural analysis at 10 K lead to the important conclusion that the JT effect only weakly distorts the structure of complex **1**. As a consequence a giant axial anisotropy parameter is found, resulting from a non totally quenched orbital angular momentum.

Acknowledgements

We thank the CNRS (Centre National de la Recherche Scientifique), the Université Paris Sud 11, the Université Paul Sabatier-Toulouse III, and the Agence Nationale de la Recherche ANR (project TEMAMA ANR-09-BLAN-0195-01) for financial support. Work performed at the National High Magnetic Field Laboratory was supported by the NSF (grant nos. DMR0654118 and CHE0924374) and the State of Florida.

REFERENCES

1. Ruamps, R., *et al., J. Am. Chem. Soc.* **135** (8), 3017-3026 (2013)

Chemistry

The key to the expansion of mass spectrometric applications is the ability to ionize an increasing number of chemically diverse species. This report highlights a method that expands ionization to alkane (wax-type) classes of molecules that have historically been problematic in ionization. They typically fragment upon ionization and yield limited molecular ion information. Here, laser-induced acoustic desorption is used to liberate the alkane species from a titanium foil into the gas phase where they are subsequently ionized by chemical ionization. Alkane, cycloalkane and branched alkanes are detected as molecular ions with little or no fragmentation products.

• Published in *Anal. Chem.*, **84**, 7131-7137 (2012)

Atmospheric Pressure Laser-Induced Acoustic Desorption Chemical Ionization Mass Spectrometry for Analysis of Saturated Hydrocarbons

L. Nyadong, J.P. Quinn and C.S. Hsu (NHMFL, Chemistry); **C.L. Hendrickson, R.P. Rodgers, and A.G. Marshall** (FSU, NHMFL, Chemistry)

Results & Discussion

We present atmospheric pressure laser-induced acoustic desorption chemical ionization (AP/LIAD-CI) with O_2 carrier/reagent gas as a powerful new approach for the analysis of saturated hydrocarbon mixtures. Non-thermal sample vaporization with subsequent chemical ionization generates abundant ion signals for straight-chain, branched, and cycloalkanes with minimal or no fragmentation. $[M\ H]^+$ is the dominant species for straight-chain and branched alkanes. For cycloalkanes, $M^{+\bullet}$ species dominate the mass spectrum at lower capillary temperature (<100 °C) and $[M\text{-}H]^+$ at higher temperature (> 200 °C). The mass spectrum for a straight-chain alkane mixture (C_{21} C_{40}) shows comparable ionization efficiency for all components (see **Figure 1**). Coupling of the technique to Fourier transform ion cyclotron resonance mass spectrometry (FT-ICR MS) for the analysis of complex hydrocarbon mixtures provides unparalleled mass resolution and accuracy to facilitate unambiguous elemental composition assignments: e.g., 1,754 peaks (rms error = 175 ppb) corresponding to a paraffin series (C_{12}-C_{49}, double bond equivalents, DBE = 0) and higher DBE series corresponding to cycloparaffins containing 1 to 8 rings. Isoabundance-contoured plots of DBE vs. carbon number highlight steranes (DBE = 4) of carbon number C_{27} to C30 and hopanes of C_{29} to C_{35} (DBE = 5), with sterane to-hopane ratio in good agreement with field ionization (FI) mass spectrometry analysis, but performed at atmospheric pressure. The overall speciation of nonpolar, aliphatic hydrocarbon base oil species offers a promising diagnostic probe to characterize crude oil and its products.[1]

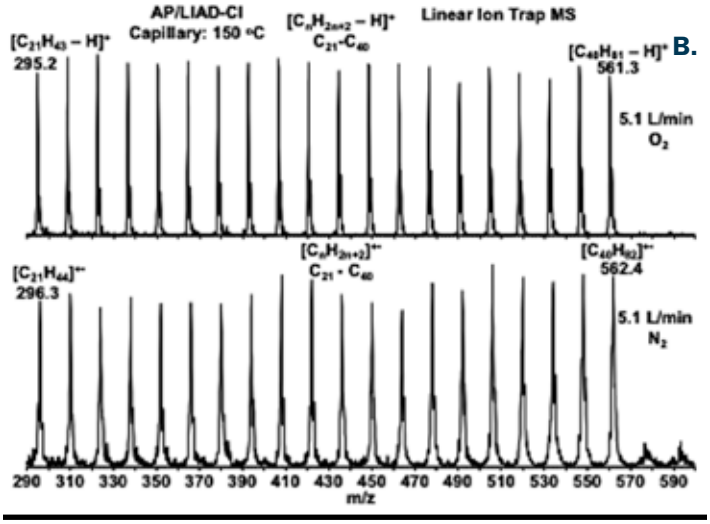


FIGURE 1. AP/LIAD-CI linear ion trap mass spectra for a mixture (40 µg/mL each) of straight-chain alkanes (C_{21}-C_{40}) for O_2 (top) or N_2 (bottom) carrier/reagent gas.

Acknowledgements

This work was supported by NSF Division of Materials Research through DMR-06-54118 and the State of Florida. The authors thank Daniel McIntosh for assistance with fabrication of the sample holder and Dr. Vladislav Lobodin for insightful discussions.

REFERENCES

1. Nyadong, L., *et al., Anal. Chem.*, **84**, 7131-7137 (2012).

Chemistry

The formation mechanism of closed-caged nanomaterials (such as fullerenes) still remains a mystery. This research utilizes a ^{13}C-labeled growth substrate (^{13}C graphite) to elucidate the growth mechanism of higher carbon-numbered species from $^{12}C_{60}$. Since the substrate is entirely composed of ^{13}C, the addition of carbon to the $^{12}C_{60}$ starting material can be monitored by ultra-high resolution mass spectrometry that resolves the isotopic envelope of the starting material and reaction products. Thus, analysis of the product isotopic distributions reveals that C_{60} grows by successive additions of $^{13}C_2$ through a closed network growth (CNG) mechanism.

• Published in *Nature Communications*, **3**, 855 (2012)

Closed Network Growth of Fullerenes

P.W. Dunk and H.W. Kroto (FSU, Chemistry); **N.K. Kaiser and J.P. Quinn** (NHMFL, Chemistry); **C.L. Hendrickson and A.G. Marshall** (FSU, NHMFL, Chemistry); **C.P. Ewels** (Université de Nantes, Institut des Matériaux Jean Rouxel); **Y. Nakanishi, Y. Sasaki and H. Shinohara** (Nagoya U., Chemistry)

Results & Discussion

Enormous advances in nanoscience have been made since the discovery of the fullerenes; however, the formation of these closed-caged nanomaterials still remains a mystery. Here we reveal for the first time that fullerenes self-assemble through a closed network growth (CNG) mechanism by ingestion of atomic carbon and C_2. The growth processes have been elucidated through experiments that probe direct growth of fullerenes upon exposure to carbon vapor, analyzed by state-of-the-art FT-ICR mass spectrometry. The key aspect is to expose gas-phase $^{12}C_{60}$ to amorphous ^{13}C graphite—the resulting isotopic distributions then definitively prove that $^{12}C_{60}$ grows by successive additions of $^{13}C_2$ (see **Figure 1**).[1]

Our results shed new light on the fundamental processes that govern self-assembly of carbon networks, and the process of fullerene growth is likely involved in formation of other carbon nanostructures from carbon vapor, such as nanotubes and graphene. Further, the results should be of importance for illuminating astrophysical processes near carbon stars or supernova that result in C_{60} formation throughout the universe.

Conclusions

Theory combined with EPR results and structural analysis at 10 K lead to the important conclusion that the JT effect only weakly distorts the structure of complex 1. As a consequence a giant axial anisotropy parameter is found, resulting from a non-totally quenched orbital angular momentum.

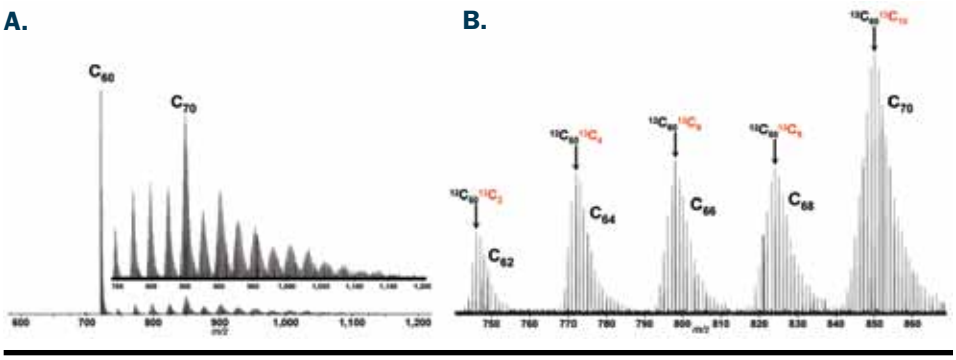


FIGURE 1. Results of exposure of C_{60} to ^{13}C-enriched carbon vapor. **A.** Positive ions generated from a target comprised of amorphous ^{13}C (99% atom ^{13}C) target mixed with C_{60} under the same conditions as in the C_{60}-graphite experiment (**B.**), with mass scale expansion of C60 illustrating the occurrence of atom exchange events. **B.** C_{62}-C_{70} mass region expanded to show growth of C_{60} to larger fullerenes by successive ^{13}C ingestion events.

Acknowledgements

We thank M. A. Duncan for critical information regarding cluster source design, G.T. Blakney for modular ICR data system work, D. McIntosh for machining of custom ion source parts, and V.V. Lobodin for discussion. C.P.E thanks A. Zobelli for discussions. This work was funded by NSF Division of Materials Research through DMR-06-54118 and the Florida State University Research Foundation.

REFERENCES

1. Dunk, P.W., *et al., Nature Commu.*, **3**, 855 (2012). doi: 10.1038/ncomms1853.

Chemistry

Single-walled carbon nanotubes (SWCNT) have gained interest in recent years for their biocompatibility and multifunctional applications, such as drug delivery. They have shown the ability to encapsulate metals that are useful as contract reagents in magnetic resonance imaging. The problem is that some metals display decreased performance at higher magnetic fields. Here, the performance of ultra-short SWCNT doped with Gd and Dy were compared in hopes of identifying species that maintain, or have higher performance at high magnetic field. Due to the high relaxivities demonstrated both in solutions and with intracellular labeling, Gd^{3+} and Dy^{3+} encapsulated US-tubes should provide excellent cell detectability for in vivo MRI-based cellular tracking.

Encapsulated Gadolinium and Dysprosium Ions Within Ultra-Short Carbon Nanotubes for MR Microscopy at 11.75 and 21.1 T

J.T. Rosenberg and F. Calixto-Bejarano (NHMFL); **M.L. Matson, B.T. Cisneros and L.J. Wilson** (Rice U., Chemistry); **M. Sokoll** (Florida State U., Chemical and Biomedical Engineering); **S.C. Grant** (Florida State U., Chemical and Biomedical Engineering, NHMFL)

Introduction

Single-walled carbon nanotubes (SWCNT) have gained interest in recent years for their biocompatibility and multifunctional applications, such as drug delivery.[1,2] Ultra-short SWCNT have demonstrated the capability to encapsulate Gd^{3+} (GNT) and have been used to label cells for MRI.[3] In contrast to Gd, which displays decreased relaxation rates at high magnetic fields, Dy^{3+} shows the opposite trends above 3 T. The hollow interior and carbon surface may present additional benefits for lanthanide-doped US-tubes at higher magnetic fields due to nanoscale confinement and favorable water exchange. This study evaluates GNT and Dy-doped SWCNT (DNT) at 11.75 and 21.1 T both in solution and with a murine microglial cell line (Bv2).

Experimental

GNT and DNT were synthesized with methods outlined by others.[3,4] MRI was performed at 11.75 T and 21.1 T at the NHMFL. For solution experiments, GNT and DNT were serial diluted from stock solution at four concentrations to measure r_1 and r_2 relaxivity. For in vitro cell experiments, a rat Bv2 microglia cell line was used following methods outlined previously.[3,5] Bv2 cells were transfected for 12 h with DNT and GNT at a final lanthanide concentration of 17 μM. Following harvest, 150,000 cells were immobilized with 2% agarose in a 10-mm NMR tube. DNT and GNT labeled cells were imaged together with cells exposed only to empty SWCNT (no lanthanide) and with unlabeled cells as controls. For T_1 and T_2 relaxation measurements, single slice 2D spin-echo (SE) sequences were used with TR and TE times varied. In addition, a 3D gradient recalled echo (GRE) sequence was acquired at 50-μm isotropic resolution with TE/TR = 7.5/150 ms.

TABLE 1

Relaxivity of DNT and GNT *at 11.75 and 21.1 T*

	r_1 ($mM^{-1}s^{-1}$)		r_2 ($mM^{-1}s^{-1}$)	
	11.75 T	21.1 T	11.75 T	21.1 T
DNT	1.05	1.91	322.7	472.2
Adj R2	1.0	0.99	1.0	1.0
GNT	17.25	8.62	352.4	400.9
Adj R2	0.94	0.94	1.0	1.0

Results

Comparing the effect of increased field strength in solution (**Table 1**), GNT show an overall larger r_1 that decreases at 21.1 T. DNT, on the other hand, shows an increase in r_1 value consistent with theoretical expectations.[6,7] For r_2, both DNT and GNT show an increase with field strength with DNTs having a larger increase. At 21.1 T, DNTs outperform GNTs as expected with the square dependence on magnetic field. When GNTs and DNTs are incorporated into Bv2 cells, T_1 contrast is quenched while T_2 and T_2^* are the dominating contrast mechanisms

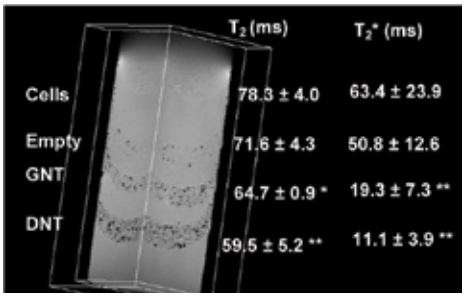


FIGURE 1. 3D GRE at 21.1 T showing increased contrast for DNT.

(**Figure 1**). As in solution, the DNTs are the more effective intracellular contrast agent with a 5.2 ms shorter T_2 and a much larger susceptibility effect with a 8.2 ms shorter T_2*.

Conclusions

This study demonstrates that the DNTs provide a strong T_2/T_2*-agent at 21.1 T, potentially with higher contrast and detectability than the GNTs. Furthermore, both of these nanoparticle agents outperform many MRI contrast agents at high magnetic field, including some iron oxides. Due to the high relaxivities demonstrated both in solutions and with intracellular labeling, Gd^{3+} and Dy^{3+} encapsulated within US-tubes should provide excellent cell detectability for *in vivo* MRI-based cellular tracking.

Acknowledgements

Funding was provided by the NSF (DMR-0084173), the NHMFL UCGP to SCG, and the American Heart Association (10GRNT3860040). The Welch Foundation (Grant C-0627) to LJW also provided support of this work.

REFERENCES

1. Chen, J., *et al., Am Chem Soc.*, **130**, 16778-16785 (2008).
2. Bianco, A., *et al., Curr Opin Chem Biol.*, **9**, 674-679 (2005).
3. Tang, A.M., *Contrast Media Mol. Imaging*, **6**, 93-99 (2010).
4. Ashcroft, J., *et al., Nanothechnology*, **20**, 5033 (2006).
5. Rosenberg, J.T., *et al., Contrast Media Mol. Imaging*, **7**, 121-129 (2011).

Chemistry

NHMFL scientist Riqiang Fu and collaborators at the FSU College of Engineering and Xiamen University in China have developed Stray Field Imaging (STRAFI) for study solid material interface such as electrode/electrolyte in lithium-ion battery. They have achieved 15μm spatial resolution using the very strong stray field gradient of the 19.6T magnet. The unprecedented resolution allows quantitative measurement of Li-ion migration *in situ* for better understanding of the charge-discharge process and ultimately enables them to improve battery performances such as energy capacitance, efficiency, safety and cycle life time.

• Published in *J. Magn. Reson.*, **225**, 93-101 (2012)

High-Resolution Imaging Probe for STRAFI Studies of Solid-Materials

J.A. Tang, J.A. Kitchen and R. Fu (NHMFL); **G. Zhong and Y. Yang** (Xiamen U.); **S. Dugar** (Florida State U., NHMFL)

Introduction

Examining the physical properties of solid materials as they are being utilized would provide useful information to improve and further develop their functions. *In situ* studies are often difficult to execute since many techniques are destructive or alter the structure from their original states. Magnetic resonance methods are often utilized since they are non-invasive allowing for a true representation of their mechanisms. A material that has garnered much attention for *in situ* studies is lithium ion batteries. The charge-discharge mechanism of Li-rechargeable batteries is important to understand so that their energy capacitance, efficiency and cycle lifetime can be improved. Most often, however, high resolution images are not easily attainable with conventional MRI methods since extremely strong gradients are not producible with typical setups. An alternative approach to MRI is stray field imaging (STRAFI) where the strong magnetic field gradients (> 50 T/m) in the fringe field of a superconducting magnet are exploited. In this work we have produced a high-resolution STRAFI probe to study solid materials. In addition to the strong gradients, hardware design, shaped pulses and power levels are examined for enhancing image resolution.

Experimental

Experiments were performed on a 19.6 T magnet with a Bruker DRX console using a custom single channel broadband probe (**Figure 1**). Shaped pulses were generated using Bruker's shaped pulse tool. LiBr solutions and $LiCoO_2$ electrodes were prepared in house.

Results & Discussion

Figure 2 shows the 1D ^{7}Li profile of a LiBr solution using shaped pulses. The uniform excitation profiles from the Gaussian and Sinc pulses reduce the amount of excitation in adjacent slices, typically produced by side lobes of the excitation profile, allowing us to obtain an image resolution of ~15 μm. With high resolution achievable, a battery phantom with electrodes ~0.25 mm thick is easily resolved (**Figure 3**). The presence of metal disks do not affect the image profile showing the possibility of studying batteries *in situ* with STRAFI[1].

Conclusions

STRAFI provides a powerful alternative to MRI when studying solid material samples. Such a high-resolution 1D imaging method can be applicable to other systems including thin films and layered systems.



FIGURE 1. Broadband STRAFI probe for materials imaging.

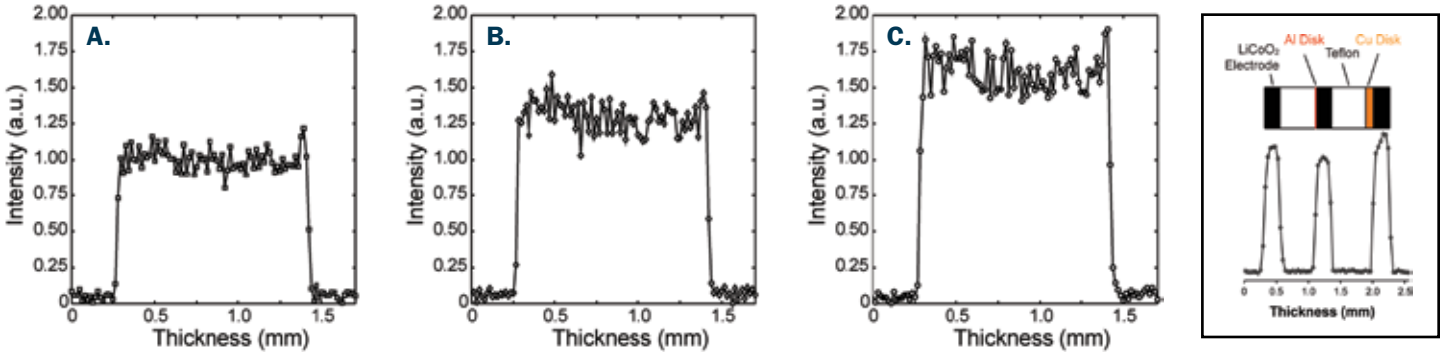


FIGURE 2. (LEFT) 1D ^{7}Li STRAFI of concentrated LiBr in D_2O using **A.** Rectangular, **B.** Gaussian and **C.** Sinc shaped pulses.
FIGURE 3. (RIGHT) 1D STRAFI profile of a battery phantom.

Acknowledgements

The authors would like to thank Prof. Jim Zheng at College of Engineering for helpful discussions and use of lab space. This work is supported by the NHMFL UCGP program.

REFERENCES

1. Tang, J.A., *et al., J. Magn. Reson.*, **225**, 93-101 (2012).

Biochemistry

Polenova's group at the University of Delaware uses solid state NMR to characterize the structure and dynamics of Gag protein from HIV-1 virus. A collection of state-of-art multi-dimensional experiments performed at the ultra-high 900 MHz magnetic field using the low-E magic-angle spinning probe technology at the NHMFL allows them to obtain detail structure and dynamic information of capsid-CA protein and capsid-spacer peptide (CA-SP1) at atomic resolution. The goal of their study is to establish the full 3D structure and investigate their interaction with inhibitor molecules of the HIV-1 protein assembly.

Solid-State NMR Structural and Dynamics Studies of HIV-1 Protein Assemblies

G. Hou, Y. Han, C. Suiter, H. Zhang and T. Polenova (U. of Delaware, Chemistry & Biochemistry); **Z. Gan, W. Brey, I. Hung and P. Gor'kov** (NHMFL)

Introduction

Gag polyprotein from HIV-1 virus is responsible for assembly of virions from infected cells. Gag and its two products, capsid CA protein and capsid-spacer peptide 1 (CA-SP1) are the focus of this research. CA organizes and protects the viral genome by assembling into conical capsids. Following the viral entry into the host, CA disassembles to allow release of the viral genetic material into the host cytoplasmic compartment (uncoating). CA and the Gag processing intermediate CA-SP1 have recently become attractive targets of HIV-1 uncoating and capsid maturation inhibitors. The current research on the development of inhibitors is hampered by lack of understanding of the molecular mechanisms for the maturation and uncoating and of their temporal regulation. The objective of our work is to gain atomic-level insight on structure and dynamics of Gag, CA, and CA-SP1 HIV-1 protein assemblies and their interactions with host proteins and small-molecule inhibitors, through state-of-the-art solid-state NMR spectroscopy.[1]

Experimental

Solid-state NMR spectra were acquired at 21.1 T (900 MHz) outfitted with a 3.2 mm Low-E triple-resonance HXY probe developed and built at NHMFL. 2D (DARR, NCA, and NCACX) and 3D (INADEQUATE, NCACX, DIPSHIFT and RNCSA) spectra for structure and dynamics characterization were acquired on U-^{13}C,^{15}N-labeled CA and CA-SP1 assemblies of tubular morphology. All spectra were processed in NMRPipe and analyzed in Sparky.

Results & Discussion

As detailed in our May 2012 research report, we have i) accomplished resonance assignments for a significant portion of the residues in tubular assemblies of CA and CA-SP1; ii) discovered that SP1 tail is unstructured in the assembled CA-SP1; and iii) obtained surprising and interesting insights into the dynamic behavior of CA (reported in part in Reference 2). Since May, we have conducted MD simulations of CA, and the results are generally in good agreement with the experimental ^{1}H-^{15}N dipolar order parameters (manuscript in preparation). To test our results that SP1 tail is unstructured in tubular CA-SP1 assemblies, we conducted additional dipolar-based (NOESY) and scalar-based (INADEQUATE) experiments, to rule out the dynamic disorder. The results shown in **Figure 1** corroborate our find-

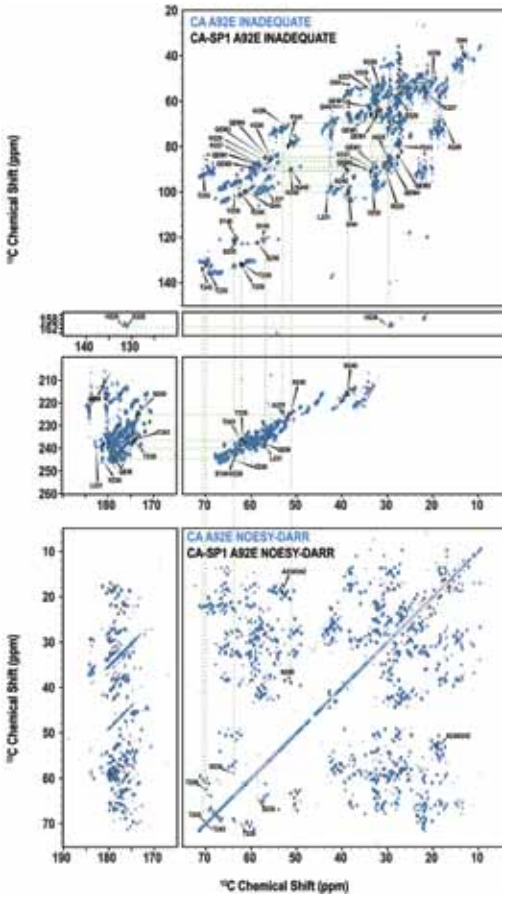


FIGURE 1. 21.1 T 2D homonuclear dipolar- and scalar-based MAS correlation spectra of U-^{13}C,^{15}N-enriched CA and CA-SP1 assemblies illustrating that the SP1 tail is unstructured in tubular assemblies.

ings. Another manuscript is in preparation to report resonance assignments of CA and conformation of SP1 tail.

Conclusions

We have continued structural and dynamics characterization of tubular assemblies of HIV-1 capsid proteins. Experiments are under way to establish the full 3D structure of the assembled CA and CA-SP1 and examine their interactions with inhibitor molecules.

Acknowledgements

This work was supported by the National Institutes of General Medical Sciences (P50GM082251) and, is a contribution from the Pittsburgh Center for HIV Protein Interactions.

REFERENCES

1. Han, Y., *et al., J. Am. Chem. Soc.*, **132**, 1976-1987 (2010).
2. Byeon, I.-J. L., *et al., J. Am. Chem. Soc.*, **134**, 6455-6466 (2012).

Biochemistry

NMR spectroscopy was utilized to establish the presence of the biological pigment eumelanin, in fossils from the Jurassic Period. Results indicate this biopolymeric material persists in the fossil record for 160 million years, the oldest determination to date.
• Published in *Proc. Natl. Acad. Sci.*, **109**, 10221-20223 (2012)

Solid-State NMR Evidence for Eumelanin from the Jurassic Period

K. Glass (Duke U. Chemistry) **and J.D. Simon** (UVa Chemistry)**; C.R. Bowers** (UF Chemistry)

Introduction

Melanin is a ubiquitous pigment found in bacteria, fungi, plants, and animals. It has a diverse range of ecological and biochemical functions. Evidence of melanin in fossil organisms previously relied entirely on indirect morphological and chemical analyses. Recently, direct chemical techniques were applied to categorically demonstrate the preservation of eumelanin in two > 160 Ma Jurassic cephalopod ink sacs and to confirm its chemical similarity to the ink of the modern cephalopod, *Sepia officinalis*[1]. This chemical analysis included solid-state carbon-13 MAS-NMR experiments performed in the NHMFL-AMRIS facility.

Experimental

The Peterborough Member of the Oxford Clay Formation (Middle Jurassic, 162 Ma) at Christian Malford, Wiltshire and the Blue Lias Formation (Lower Jurassic, 195 Ma) at Lyme Regis, Dorset, yield coleoid cephalopods containing black ink sacs preserved in three dimensions. SEM images of a specimen from each of these deposits, reveal that the ink is composed of globular granules similar in size and shape to that of the modern coleoid *S. officinalis*. To verify that the organic functional groups present in the surface of the sample also pervade the bulk of the pigmented fossil, CP-MAS NMR spectra were acquired using AMRIS' 600 MHz NMR spectrometer.

Results & Discussion

As seen in **Figure 1A**, three characteristic spectral regions were identified: 10–90 ppm, aliphatic carbons, most likely due to proteinaceous material; 90–160 ppm, aromatic carbons, including indole or pyrrole type carbons within the polymer; and 160–225 ppm, carbonyl carbons from amides, carboxylates, and quinones which may be associated with the melanin polymer as well as the proteinaceous material. Variable CP contact time experiments where performed to further differentiate protonated aliphatic carbon atoms at 90–130 ppm from non-protonated aliphatic carbon atoms at 130–160 ppm. The spectrum for the GSM 122841 sample is shown in **Figure 1A.** The sediment spectra for GSM 122841, shown in **Figure 1B**, lacks the aromatic carbon and carbonyl carbon peaks found in melanin.

Conclusions

The NMR results helped to demonstrate that eumelanin persists in the fossil record for at least 160 million years, the oldest determination to date. Within the limits of the techniques used, the preserved pigment exhibits properties that are chemically similar to modern phylogenetically related *S. officinalis*. The results further our understanding of the distribution of melanin in ancient organisms.

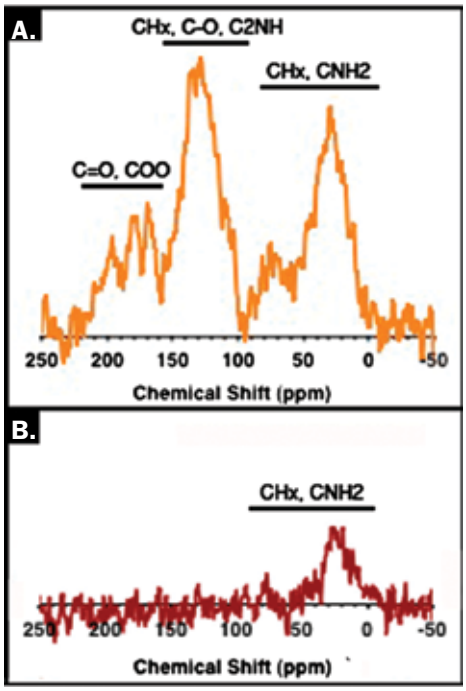


FIGURE 1. A. CP-MAS SSNMR spectrum of the Peterborough cephalopod sample. The presence of the functional groups revealed in the XPS data is confirmed for the bulk sample through its SSNMR spectrum. **B.** The result of the XPS analysis of the sediment is corroborated by the lack of key melanin aromatic and carbonyl signals in its SSNMR spectrum.

Acknowledgements

Fossil samples were provided by the British Geological Survey and Mr. Paddy Howe. Technical assistance received from Professor Joanna Long is gratefully acknowledged.

REFERENCES

1. Glass, K. *et al. PNAS* **109**, 10221-10223 (2012).
2. Adhyaru, B.B. Akhmedov, N.G.; Katritzky, A.R.; Bowers, *C.R. Magn. Reson. Chem.* **41**, 446 (2003).

Biochemistry

This work presents a valuable step in the development of self-assembling nanofiber structures to be used in forefront medical applications. It clarifies that the fiber assembly is likely based on a repetitive hairpin structure of a relatively simple amino acid and thereby provides a path forward.

Solid State NMR Structural Characterization of MAX8 Peptide Nanofibers

S.R. Leonard, A.R. Cormier, X. Pang, M.I. Zimmerman and H.X. Zhou (Florida State U., Institute of Molecular Biophysics); **A.K. Paravastu** (Florida State U., Chemical and Biomedical Engineering)

Introduction

The peptide MAX8 (VKVKVKVK^{D}PPTKVEVKVKV-NH_2) was designed by Schneider *et al.* to self-assemble controllably in order to form a 3-dimensional support structure for implanted stem cells and cell cultures. The peptide was designed to form a hairpin structure composed of 2 β-strand segments in the presence of salt. Self-assembly into a nanofiber network is hypothesized to be initiated by molecular hairpin formation.[1] In this project, we employed solid state nuclear magnetic resonance (NMR) spectroscopy on MAX8 nanofiber samples in order to produce a detailed molecular model.

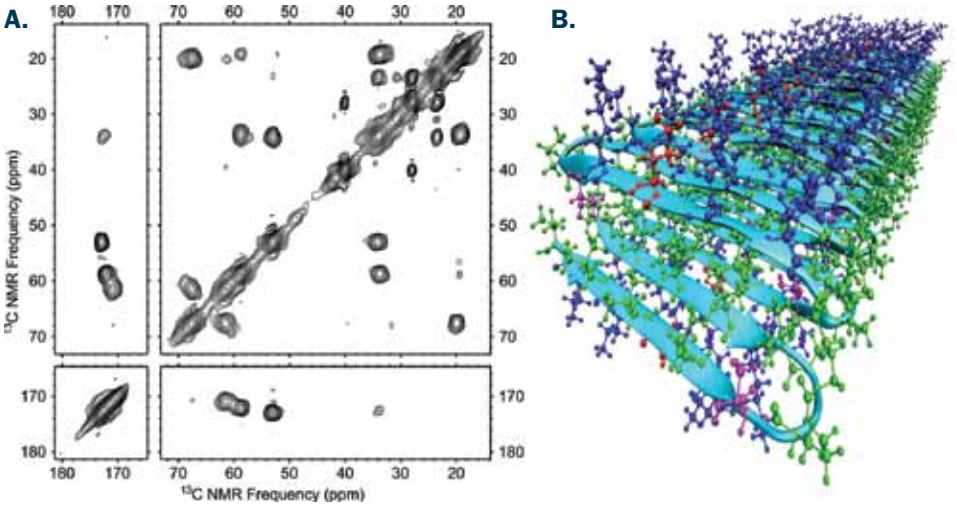


FIGURE 1. A. 2D fpRFDR spectrum of uniformly ^{13}C-labeled V3, T12, and K17 MAX8, **B.** A possible all-atom molecular model for the MAX8 nanofiber.

Experimental

Structural constraints determined by NMR were introduced into annealing molecular dynamics computer simulations to produce the molecular model. NMR constraints include site-specific ^{13}C NMR peaks positions, which report on secondary structure, and inter-atomic distances between selectively ^{13}C-labeled sites, which test predictions based on inter-molecular packing schemes. Site-specific knowledge of NMR peak positions is determined by 2D-exchange finite pulse radio frequency driven recoupling (fpRFDR) spectroscopy (**Figure 1A**).[2] Decays of NMR peak intensities under the PITHIRDS-CT ^{13}C-^{13}C dipolar recoupling experiment[3] provide more quantitative information on inter-atomic proximities.

Results & Discussion

Characteristic secondary shifts of lysine and valine α- and β-carbons, as determined by fpRFDR spectroscopy, are consistent with linear β-strand secondary structure.[4] Narrow linewidths indicate a well-ordered system though NMR spectra indicate that approximately 10% of the sample consists of a minority structure possessing different secondary structure. PITHIRDS-CT data for selectively ^{13}C-labeled MAX8 nanofiber samples corroborate the formation of a closed hairpin, as reported by Schneider, *et al.*,[5] while also providing additional constraints which indicate further assembly into parallel β-sheets. Additional structural constraints are required to fully characterized the between sheet structure of MAX8 nanofibers though a possible molecular model is presented (**Figure 1B**).

Conclusions

These results show that a simple repetitive amino acid sequence can produce nanofibers with well-defined molecular structure. However, the work also indicates that we presently have little predictive ability when it comes to

several details of intermolecular packing. A known structure provides a basis for future work on assembly under different conditions and mechanistic studies of molecular structure formation.

Acknowledgements

This research was supported by funds from the National Science Foundation Grant DMR-105521 to AKP, an NHMFL User Collaboration Grant award to AKP, and the National Institute of Health Grant GM88187 to HXZ.

REFERENCES

1. Haines-Butterick, L., *et al., Proc. Natl. Acad. Sci.*, **104**, 7791 (2007).
2. Ishii, Y., *et al., Chem. Phys.*, **266**, 231 (2001).
3. Tycko, R., *J. Chem. Phys.*, **126**, 064506 (2007).
4. Leonard, S.R., *Biophys. J.*, **105**, 222 (2013).
5. Ozbas, B., *Macromolecules*, **37**, 7331 (2004).

Biology

Direct imaging of tissue sodium *in vivo* was performed using the advanced imaging capabilities on the 900 MHz UWB magnet system. The results of this study demonstrate that the initial sodium concentration in the tumor could provide important information about the level of drug resistance before tumor therapy. *In vivo* sodium signal from the rat head was detected using an optimized MRI sequence that included back-projection MRI with a short readout times. In addition imaging of water diffusion was achieved using a proton MRI sequence with optimized diffusion gradients. Using both imaging modalities, tumor pathophysiology and anatomy can be monitoring in the live animal.

• Published in *Magnet. Reson. Med*, **67**, 1159-1166 (2012)

Emerging Tumor Resistance and Sodium-Diffusion MRI

V.D. Schepkin, P.L. Gor'kov and W.W. Brey (NHMFL); T. Morgan, S. Gower-Winter and C.W. Levenson (Florida State U., College of Medicine)

Introduction

MRI is an important tool in cancer detection and treatment. The high magnetic field of 21.1 T dramatically improves our capability to perform *in vivo* MRI. It is known that tumor progression, especially after therapeutic intervention, may dramatically change tumor resistance to therapies. Consequently, a much higher concentration of a chemotherapeutic drug is required to achieve the same response; otherwise, the chemotherapy is unlikely to be successful. Sodium concentration and diffusion are usually higher in brain tumors than in a normal brain and our studies reveal an attractive correlation between sodium/diffusion concentrations and glioma drug resistance.[1,2] The hypothesis in this study is that the increased tumor resistance is determined by a more efficient energy metabolism in such cells which can be detected by the corresponding decrease of glioma sodium concentration and diffusion.

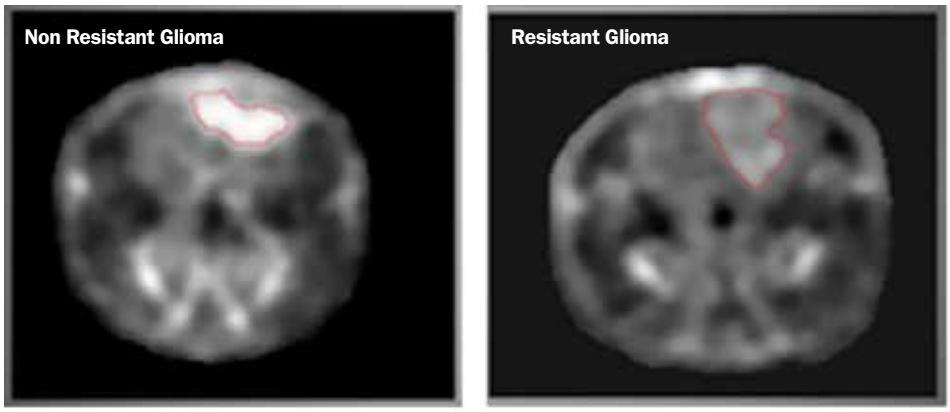


FIGURE 1. Sodium MRI of non-treated rat glioma originated from 9L cells having different chemotherapeutic resistances to carmustine. Sodium MRI with resolution 0.5x0.5x0.5 mm demonstrate energy deficit in non-resistant glioma (left) and superior prognosis for chemotherapy.

Experimental

Sodium MRI in this study was performed using advanced *in vivo* sodium MRI capability at 21.1T. Complete sodium signal from rat head was detected by back-projection MRI with a short readout time of 2.2 ms. Diffusion MRI pulse sequence had a special shape of the diffusion gradients and the back projection acquisition. Both measures were selected to allow for motion compensations. 9L rat glioma model, was used in this study, sodium MRI was done by 3D pulse sequence with repetition time of 100 ms to avoid saturation of the MR signal which required a total scan time of 27 min. Resolution of sodium images was 0.5 mm. Diffusion MRI was performed by 2D pulse sequence with a slice thickness of 0.7 mm, the rest of parameters are often used by others.

Results & Discussion

Sodium concentration in glioma at ~ 11 days after tumor implantation is given in **Figure 1**. The difference is very noticeable without processing. The naïve 9L cells generated tumor with a high tumor sodium concentration relative to the normal brain, while the resistant glioma line showed a much lower sodium contrast pattern.

The most resistant glioma has the lowest tumor sodium concentration and the lowest diffusion values. The question arises whether sodium in tumors can be

related to energy metabolism in cancer cells. The Na/K pump is the major extrusion mechanism of sodium out of the intracellular space, and it may consume up to ~ 60% of total ATP to perform this task. It is also known that increased intracellular Na content leads to an additional activation of the Na/K pump and to a higher consumption rate of ATP. Thus, increased sodium can be an indicator of energy deficit in cancer cells and it can be detectable by MRI. Naïve cells (less resistant) have the largest deficit of energy and such cells are the most vulnerable to therapeutic interventions. The absence of an energy deficit in resistant tumor cells is an advantage to such cells in their fight against drug interventions.

Conclusions

The results of this study demonstrate that emerging tumor resistance can be detected by sodium and diffusion MRI. The evaluation can be done noninvasively and prior to therapy. It is important to note here that we are speaking not only about resistance to carmustine. It is expected that an energy-based MRI indicator of tumor resistance can be predictive for a range of different therapeutic interventions. The prompt evaluation of tumor resistance may help to formulate individual treatment and avoid unsuccessful therapies.

Acknowledgements

Special thanks to Ashley Blue, Richard Desilets, Jason Kitchen, Fabian Calixto-Bejarano, Manuel Ozambela Jr. and Deborah Morris for their invaluable contributions to the project.

REFERENCES

1. Schepkin, V.D., *et al.*, Proceedings of ISMRM, Melbourne, Australia, #184 (2012).

2. Schepkin, V.D., *et al., Magnetic Resonance in Medicine*, **67**, 1159-1166 (2012).

Biology

The allure of high field MRI is not only the use of increased nuclear spin polarization resulting in higher signal to noise (SNR) for increased spatial resolution but also increased temporal resolution. In addition to increased SNR, utilizing accelerated imaging sequences commonly used at low fields can increase temporal resolution. High magnetic fields represent additional challenges for accelerated imaging due to increased susceptibility gradients and other artifacts that distort not only anatomical information but also quantification. In this report, Leftin et al. demonstrate the use of a new suite of super-resolved ultrafast single-shot spatiotemporally encoded (SPEN) imaging sequences that are robust in the presence of high-field artifacts and offer high temporal resolution. They demonstrate the usefulness of these sequences in a live rodent model of cerebral infarction following stroke on the 900MHz UWB magnet system.

Ultrafast *in vivo* Diffusion Imaging of Stroke at 21.1 T by Spatiotemporal Encoding

A. Leftin, E. Solomon and L. Frydman (Weizmann Institute, Chemical Physics)**; J.T. Rosenberg, F. Calixto-Bejarano** (NHMFL)**; S.C. Grant** (Florida State U., Chemical and Biomedical Engineering, NHMFL)

Introduction

Two of the most pressing concerns in MRI have been the enhancement of image signal-to-noise and speed of image acquisition. The former has motivated a push to higher magnetic fields while the later issue has inspired echo-planar imaging (EPI), parallel imaging and compressed sensing. These solutions also can degrade image quality by introducing susceptibility gradients and other artifacts that distort not only anatomical information but also quantification. Fortunately, a new suite of super-resolved ultrafast single-shot spatiotemporally encoded (SPEN) imaging sequences[1] are robust in the presence of high-field artifacts and offer high temporal resolution.

Experimental

Using an EPI readout, SPEN employs a 90° excitation achieved with a chirped pulse in the presence of a gradient.[1] For slice selection, a standard three-lobed 180° sinc pulse is used, with diffusion encoding gradients surrounding the pulse. Fully refocused SPEN signals were acquired with a 30-40 ms EPI readout covering a FOV of 32×32×2 mm using a matrix size of 100×100. SPEN-DWI was obtained at six b-values. Standard DW-EPI and DW-SE experiments were conducted using SE excitation and diffusion parameters similar to the SPEN-DWI experiments. For *in vivo* experiments, stroke was induced by middle cerebral artery occlusion (MCAO) using a 2-3-mm rubber coated filament according to methods previously described.[2] The two-hour occlusion created a stroke in the right striatum and cortex; 3 MCAO stroked rats and 2 control rats were scanned one day after stroke.

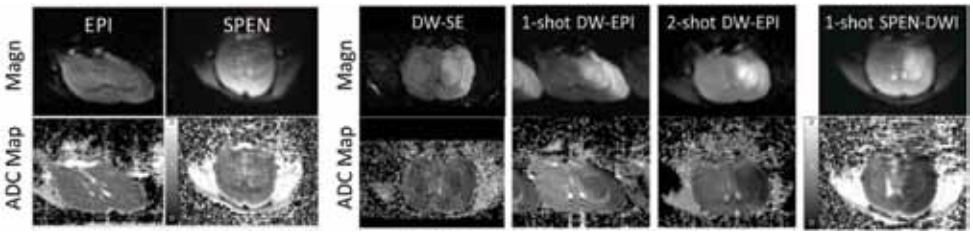


FIGURE 1. Control rat magnitude MRI & ADC maps acquired at 21.1 T.
FIGURE 2. Stroked rat magnitude DW-MRI (b = 1000) & ADC maps for different acquisition schemes.

Results & Discussion

Figures 1 and 2 show representative magnitude images and ADC maps (μm^2/ms) for each of the acquisition techniques. At 21.1-T, the SPEN-DWI sequence is immune to susceptibility artifacts that are particularly strong in non-segmented DWI-EPI using similar acquisition parameters. SPEN-DWI reveals a large hyperintense stroke region characteristic of toxic edema and swelling associated with the MCAO. Though the DW-SE provides the best quality images, the required acquisition time (>19 min) severely restricts diffusion measurements to a reduced number of b-values. For all acquisitions, decreased ADCs were evident in the stroke lesion compared to contralateral and control measurements, but SPEN-DWI ADC values and lesion extent differ from DW-EPI.

Conclusions

Overall, the quality of the SPEN-DWI and resulting ADC maps make this form of single-shot acquisition a clear choice for comprehensive, high-throughput *in vivo* stroke studies at ultra-high fields and/or heterogeneous signal regions.

Acknowledgement

All work has been conducted in accordance with FSU Animal Care and User committee. Funding provided by the American Heart Association (10GRNT3860040) and NHMFL-UCGP (S.C.G). Funding at the Weizmann Institute provided by Fulbright Award and NSF IRFP CHE 1064075 (A.L) and Minerva Foundation, Metaflux (L.F.).

REFERENCES

1. Ben-Eliezer, *Magn. Reson. Med.*, **63**, 1594–1600 (2010).
2. Rosenberg, J.T., *et al., Cytotherapy.* 15(3):307-22. (2013).
3. Solomon, E., *et al., J. Magn. Reson.* 232:76-86. (2013)

Biology

A combination of methods, including NMR spectroscopy and mass spectrometry, were used to investigate pheromones in nematodes. Nematodes are microscopic worms inhabiting a broad range of environments, impacting human health, crops and animals. Results confirm a female-specific attractant and male specific attractant made by the opposite sex with possibly separate genetic regulation.

• Published in *P. Natl. Acad. Sci. USA*, **109**, 20949-20954 (2012)

Identification of Male and Female Mating Pheromones in *Panagrellus redivivus*

A. Choe, A.A. Kolawa (Caltech, Biology)**; T. Chuman, A.T. Dossey, R. Ajredini and A.S. Edison** (UF, Biochem & Mol Bio)**; S.H. von Reuss, J. Yim, F.C. Schroeder** (Boyce Thompson Institute, Cornell University)**; F. Kaplan, H.T. Alborn and P.E. Teal** (USDA, Gainesville, FL)**; P.W. Sternberg** (HHMI & Caltech, Biology)

Introduction

Nematodes are the most abundant animal on earth, and they live in virtually every ecological niche on earth. Parasitic species have a significant health and economic impact through the infection of crops, domestic animals, and humans. Therefore, we are working to unravel the chemical language used by nematodes, with the ultimate goals of better understanding the role of small molecules in regulating behavior and of developing new approaches to control nematode parasites. We and others have shown that nematodes produce a family of signaling molecules called ascarosides that act as pheromones that regulate,[1,2] mating attraction,[3] aggregation,[4] and dispersal.[5] Von Reuss and co-workers have developed an efficient liquid chromatography-mass spectrometry (LC-MS) screen for ascarosides and have found over 150 different molecules in the model nematode Caenorhabditis elegans,[6] and using this screen Choe and co-workers discovered ascarosides in many free-living and parasitic nematode species. In this study, we used both traditional activity-guided fractionation (AGF) and metabolomics screening to identify both the male and female mating pheromones in the free-living nematode, Panagrellus redivivus.[7]

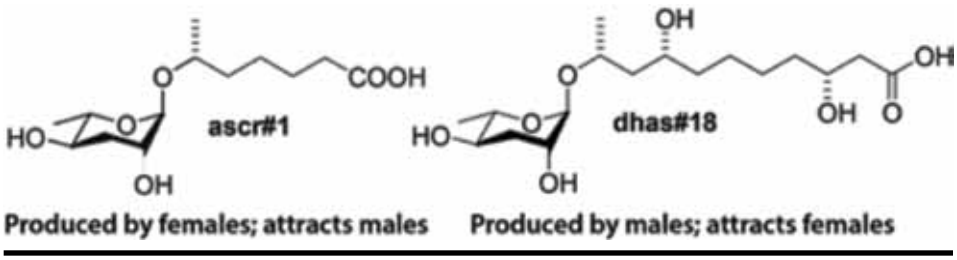


FIGURE 1.

Experimental

We used NMR, LC-MS, synthetic chemistry and behavioral assays to identify the pheromones. These are all described in detail in our recent publication.[7]

Results & Discussion

Using AGF, we found that males were strongly attracted to ascr#1 and females to dhas#18. This was conducted using mixed cultures from both males and females. Using the LC-MS metabolomic screen6 we found that these compounds were made exclusively by the opposite gender.

Conclusions

This study is the first to show a female-specific attractant in nematodes. These results suggest different types of genetic regulation of biosynthesis in males and females. We were especially pleased that two independent approaches, AGF and metabolomics, yielded the same conclusion.

Acknowledgements

Supported by NIH R01GM085285 to ASE.

REFERENCES

1. Jeong, P. Y. *et al.*, *Nature* **433**, 541–545 (2005).
2. Butcher, R.A., Fujita, M., CC, S.F. & Clardy, J., *Nature chemical biology* **3**, 420–422 (2007).
3. Srinivasan, J. *et al.*, *Nature* **454**, 1115–1118 (2008).
4. Srinivasan, J. *et al.*, *PLoS Biol* **10**, e1001237 (2012).
5. Kaplan, F. *et al.*, *PloS one* **7**, e38735 (2012).
6. Reuss, von, S. H. *et al.*, *J. Am. Chem. Soc.* **134**, 1817–1824 (2012).
7. Choe, A. *et al.*, *Proc. Natl. Acad. Sci. U. S. A.* **109**, 20949–20954 (2012).







User Summer School

A crash course in measurement techniques

From May 13 to 17, the MagLab hosted a group of 46 graduate students, post-doctoral associates and early career investigators for the 2013 Summer School. The participants came from 25 institutions in six different countries to gain practical measurement experience and learn skills to take back to their home laboratory. Students participated in tutorials on measurement techniques, did hands-on exercises and attended lectures from experts in condensed matter physics. This year's summer school had twice as many participants as last year and added four more lab practicums.

For more information on summer school or to apply for next year's session, please visit our website: **http://magnet.fsu.edu/summerschool**

Quotes from Participants

What they thought of the program:

"It was like summer camp for experimental condensed matter physicists."

"You gain a lot of experience in the lab in a short amount of time."

"This is a great way to be introduced to the many different ways to measure magnetic properties."

"The hands-on activities provided valuable exposure to experimental equipment and techniques."

"Lectures explained both theoretical and experimental aspects of materials."

"The staff does great work and makes learning enjoyable."

"I wish Summer School was longer than a week."

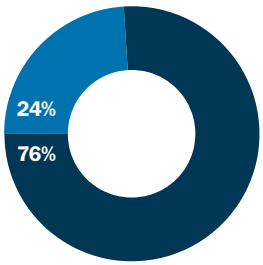
Topics suggested for future sessions:

- Magnet design
- Fermi surfaces
- EMR, ESR & EPR
- Cryogenics
- Magnetic optics
- Thermodynamics
- Torque & transport
- Physics of Noise
- Neutron Scattering
- Becoming a user

Diversity Stats

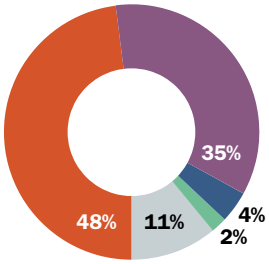
GENDER

11 females and 35 males



RACE & ETHNICITY

22 White
16 Asian
2 Black/African American
1 Hispanic/Latino
5 Prefered not to respond





MagLab News

HONORS & AWARDS

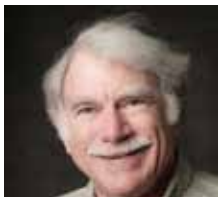


David Larbalestier, Director of the MagLab's Applied Superconductivity Center, was named an Institute of Electrical and Electronics Engineers (IEEE) Fellow. He was recognized for his many accomplishments in materials research and superconductivity.





Magnet Lab scientists **Peter Lee** and **Dragana Popović** have been recognized as 2013 Distinguished University Scholar award winners from Florida State University — the only two recipients of the award this year. Peter Lee is a Principal Investigator at the National High Magnetic Field Laboratory's Applied Superconductivity Center and Dragana Popović is a scholar/scientist in the lab's condensed matter science group and the MagLab's Diversity Committee chair. This award honors the work of exemplary and creative researchers who are not tenured or tenure-seeking.



Alan G. Marshall, Director of the Ion Cyclotron Resonance Program at the National High Magnetic Field Laboratory, has been elected as a fellow of the American Academy of Arts and Sciences, a prestigious independent policy research center founded in 1780 that conducts multidisciplinary studies of complex and emerging problems. Marshall is world-renowned for his pioneering work in co-inventing and developing Fourier Transform Ion Cyclotron Resonance (FT-ICR) mass spectrometry. Marshall has previously been recognized with numerous awards including a Robert O. Lawton Distinguished Professor, Kasha Professor of Chemistry and Distinguished Research Professor, a fellow of the American Physical Society and a recipient of the William H. Nichols Medal. As an American Academy of Arts and Sciences fellow, Marshall joins the prestigious company of George Washington, Thomas Jefferson, Ralph Waldo Emerson, Alexander Graham Bell and Ben Franklin.



Peter Hirschfeld, part of the National High Magnetic Field Laboratory team at the University of Florida, has been selected 2012-2013 University Teacher/Scholar of the Year. The University of Florida's oldest faculty award, it is awarded to a faculty member who "demonstrates distinguished achievement in both teaching and scholarly activity and visibility within and beyond the university." Hirshfeld is now the University of Florida's nominee for the SEC Distinguished Faculty Achievement Award.



MagLab-affiliated professor, **Rufina Alamo**, has received the 2013 FSU Distinguished Research Professor Award recognizing outstanding faculty members known for their pioneering and/or creative work. Alamo is a professor of chemical engineering at the Florida State University-Florida A&M College of Engineering and is a frequent MagLab researcher.



John Kynoch, Head of Facilities of the National High Magnetic Field Laboratory in Tallahassee, was honored Tuesday, May 21, 2013 with a Gabor Award for outstanding work at the FSU Office of Research employee recognition luncheon. Selection for the Gabor Award is based on an employee's superior accomplishments that contribute to Florida State University's efficiency and effectiveness.



Kevin Ingersent, a NHMFL faculty member in condensed matter theory, was appointed Chair of the Department of Physics at the University of Florida beginning in the fall 2013. He was elected a Fellow of the American Physical Society in 2009 and has served several terms on the NHMFL Research Program Committee. He directed the UF Physics Research Experiences for Undergraduates program from 1999 to 2008, and has served as the UF Physics Department's Associate Chair since 2009.



Jim Brooks, MagLab Director of Condensed Matter Science, was named Chair of the Department of Physics at Florida State University beginning in the fall of 2013. Brooks researches electronic and magnetic mechanisms in low dimensional and novel materials. He was elected a Fellow of the American Physical Society in 1999 and has served as a member of the editorial board for the Journal of Low Temperature Physics (2010).



Shermane Benjamin, a MagLab graduate research assistant in physics, was awarded a McKnight Doctoral Fellowship from the Florida Education Fund. This fellowship seeks to address the underrepresentation of minority faculty at Florida colleges and universities by investing in African-Americans and Hispanics pursuing a Ph.D in a variety of areas, including physics.

COMING & GOING



John Pucci, Head of Cryogenic & 45 T Hybrid Operations, joined the Lawrence Berkeley National Laboratory to lead its Cryogenic Operations group. He has been a part of the MagLab for 18 years and was the recipient of Florida State University's Gabor Superior Accomplishment Award in 2000.



The MagLab reaffirmed our commitment to creating a safe environment when **Kyle Orth** rejoined the Magnet Lab's safety team as an Industrial Safety & Health Engineer. He previously served as the lab's safety manager and brings more than 15 years of experience in the area of safety management.

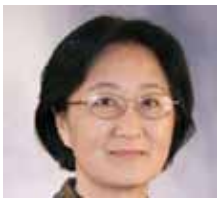


Kathy Hedick, Magnet Lab User Program Chief of Staff, will be retired from the Magnet Lab on September 12. She joined the MagLab in December 1994 and has been part of numerous Open Houses, many issues of MagLab Reports and four renewal proposals. She is responsible for the creation of eight different information management systems and has played an important leadership role, both as the keeper of all historical knowledge and advisor on the future of the lab. We thank her for her years of service and wish her well in her next chapter.

BRIEFS



In early April, the Leon County Board of Commissioners presented a Proclamation to **Eric Palm**, Deputy Director of the Mag Lab, in recognition of the NSF's $168 million grant award to the NHMFL.



Mei Zhang, associate professor of physics, was awarded an FSU Planning Grant for her work on solid state fabrication of graphene nanoribbons.



Assistant Professor **Samuel Grant** was awarded the FSU Planning Grant Award for 2012-2013 for his work on "Delayed Human Mesenchymal Stem Cell Injections for Stroke Treatment as Evaluated by High Field MRI."



Wei Guo, professor and member of the Scientific Staff of Magnet Science and Technology section, won the FSU First Year Assistant Professor Award for 2012-2013 for "Producing a Line of Excimer Helium Molecules for Visualization Study of Turbulence in Superfluid Helium-4."

SPECIAL NOTE



Jim Sims, one of the MagLab's leading pulsed magnet engineers, passed away on May 29, 2013 after an extended battle with cancer. He was an exceptional engineer whose lead role in developing the 60 T Long Pulse Magnet earned the MagLab one of its early successes in magnet technology development. Donations can be made to the Jim Sims Memorial Engineering Scholarship Fund (through the Los Alamos Public Schools Foundation).

MagLab Reports

1800 E. Paul Dirac Drive
Tallahassee, FL 32301-8350

Non-profit
Organization
U.S. Postage
PAID
Tallahassee, FL
Permit No. 55

www.magnet.fsu.edu

Facebook.com/NationalMagLab
@NationalMagLab
Youtube.com/nhmfl

The MagLab is supported by the National Science Foundation and the State of Florida.

© 2013 National High Magnetic Field Laboratory · Florida State University · University of Florida · Los Alamos National Laboratory

To become a user at the National High Magnetic Field Laboratory, visit: **http://magnet.fsu.edu/usershub**